université PARIS-SACLAY

Topology optimization applied to rotating electrical machines : analysis of electromagnetic and vibrational performance

Optimisation topologique appliquée aux machines électriques tournantes : analyse des performances électromagnétiques et vibratoires

Thèse de doctorat de l'université Paris-Saclay

École doctorale n° 575, Electrical, Optical, Bio-physics and Engineering EOBE
Spécialité de doctorat : Génie électrique
Graduate School : Sciences de l'ingénierie et des systèmes. Référent : CentraleSupélec

Thèse préparée dans le **Laboratoire de Génie Electrique et Electronique de Paris (Université Paris-Saclay, CentraleSupélec, CNRS)**, sous la direction de **Philippe DESSANTE**, Professeur des Universités, le co-encadrement de **Maya HAGE HASSAN**, Maître de conférences, **Xavier MININGER**, Professeur des Universités, et de **Guillaume KREBS**, Maître de conférences

Thèse soutenue à Paris-Saclay, le 30 septembre 2025, par

Alessandro SILVESTRINI

Composition du jury

Membres du jury avec voix délibérative

Frédéric MESSINE Professeur, ENSEEIHT – Toulouse INP	Président
Stéphane VIVIER Maître de Conférence, Université de Technologie de Compiègne	Rapporteur & Examinateur
Abdelmounaïm TOUNZI Professeur, Université de Lille	Rapporteur & Examinateur
Christine PRELLE Professeur, Université de Technologie de Compiègne	Examinatrice
Lionel PICHON Professeur, Université Paris-Saclay	Examinateur

THESE DE DOCTORAT

NNT : 2025UPAST102

université PARIS-SACLAY

ÉCOLE DOCTORALE
Physique et ingénierie : Electrons, Photons, Sciences du vivant (EOBE)

Titre : Optimisation topologique appliquée aux machines électriques tournantes : analyse des performances électromagnétiques et vibratoires

Mots clés : optimisation topologique, machine électrique, moteur synchrone à réluctance, optimisation multiphysique, réduction des vibrations

Résumé : Face au défi climatique, l'Union Européenne s'est fixé l'objectif ambitieux d'atteindre la neutralité carbone d'ici 2050, ce qui passe notamment par des progrès majeurs dans la conversion électromécanique, indispensable aux énergies renouvelables et à la mobilité électrique. Dans ce contexte, cette thèse explore l'optimisation topologique appliquée à la conception des machines électriques, en se concentrant principalement sur les moteurs synchrones à réluctance. L'enjeu est de proposer des méthodes innovantes capables de traiter des problématiques complexes, en prenant en compte les aspects magnétiques, mécaniques et vibratoires. Pour cela, une méthodologie complète d'optimisation basée sur la méthode SIMP est développée, combinant modélisations magnéto-statiques et mécaniques, et intégrant des stratégies pour limiter les vibrations. Une nouvelle manière de formuler le problème d'optimisation est proposée, permettant de réduire considérablement le temps de calcul sans compromettre les performances électromagnétiques. Le travail propose aussi une approche multiphysique croisant optimisation magnétique et mécanique, avec une comparaison entre une optimisation séquentielle en deux étapes et une optimisation simultanée. L'impact des contraintes mécaniques sur les performances globales est analysé en détail. Enfin, l'optimisation est étendue à la réduction des vibrations en repensant la structure du carter de la machine. Le but est de minimiser l'impact des forces électromagnétiques sur le comportement vibratoire, pour améliorer à la fois la robustesse et le confort acoustique. Les principales contributions de cette thèse reposent sur de nouvelles méthodologies pour optimiser les moteurs synchrones à réluctance, sur l'intégration explicite des critères vibratoires dans le processus de conception, et sur des avancées concrètes pour concevoir des machines électriques plus efficaces et plus fiables.

Title : Topology Optimization Applied to Rotating Electrical Machines : Analysis of Electromagnetic and Vibrational Performance

Keywords : topology optimization, electrical machine, synchronous reluctance motor, multiphysics optimization, vibration reduction

Abstract : In response to the climate challenge, the European Union has set the ambitious goal of achieving carbon neutrality by 2050, a mission that demands major advancements in electromechanical conversion technologies, essential for renewable energy and electric mobility. Within this framework, this thesis explores the use of topology optimization in the design of electrical machines, focusing mainly on synchronous reluctance motors. The aim is to develop innovative methods capable of tackling complex problems, considering magnetic, mechanical, and vibrational aspects. To achieve this, a complete optimization methodology based on the SIMP method is developed, combining magnetostatic and mechanical models while also integrating strategies to reduce vibrations. A new way of formulating the optimization problem is proposed, significantly cutting computation time without sacrificing electromagnetic performance. The work also introduces a multiphysics approach that links magnetic and mechanical optimizations, comparing a sequential two-step process with a fully coupled simultaneous optimization. The impact of mechanical constraints on overall performance is thoroughly analyzed. Finally, the optimization approach is extended to vibration reduction by redesigning the housing structure of the machine. The goal is to minimize the effects of electromagnetic forces on vibratory behavior, enhancing both robustness and acoustic comfort. The main contributions of this thesis lie in the development of new optimization methods for synchronous reluctance motors, the explicit integration of vibrational performance criteria into the design process, and concrete advances toward designing more efficient and reliable electrical machines.

Mamma, a te.

Ancora una volta ti dedico questo traguardo,

raggiunto nel tuo ricordo,

la prova che la tua forza continua a guidarmi.

Remerciements

Ce manuscrit marque la fin de trois années de recherche. Ma reconnaissance va à toutes les personnes qui, de près ou de loin, ont contribué à ce projet.

J'exprime tout d'abord ma profonde gratitude aux membres du jury, en particulier aux rapporteurs, M. Stéphane VIVIER et M. Abdelmounaïm TOUNZI, pour le temps qu'ils ont consacré à la lecture de mon manuscrit, ainsi que pour leurs questions pertinentes et leurs remarques constructives durant l'évaluation de ma thèse. Je tiens également à remercier les examinateurs, Mme Christine PRELLE, M. Frédéric MESSINE et M. Lionel PICHON, pour leurs questions et les discussions que nous avons eues lors de ma soutenance de doctorat.

Je remercie vivement mon équipe encadrante, composée de mon directeur, Philippe DESSANTE, et de mes co-encadrants, Maya HAGE-HASSAN, Xavier MININGER et Guillaume KREBS. Merci de m'avoir accompagné tout au long de ces trois années. Vos conseils, votre soutien constant et la contribution de chacun sur des sujets scientifiques variés ont été déterminants pour le succès de cette thèse.

Je remercie également tous les membres du laboratoire GeePs, permanents et non-permanents, pour les échanges fructueux et l'aide qu'ils m'ont apportée.

Un merci tout particulier à tous les doctorants, aux anciens comme aux nouveaux. Ces trois années de thèse m'ont permis de nouer de nombreuses amitiés, et la richesse des échanges culturels a été une source d'apprentissage et de perspectives nouvelles. Citer tout le monde serait bien trop long, mais à tous ceux qui liront ces lignes et se reconnaitront, je leur adresse un grand et sincère merci.

Je souhaite adresser un remerciement tout particulier à Thomas, mon compagnon d'optimisation topologique, pour tous les moments passés ensemble et nos mille discussions. Un grand merci également à Hakim. Depuis mon premier jour de doctorat, il a été un ami précieux avec qui j'ai partagé d'innombrables moments et qui m'a été d'un grand conseil.

J'aimerais aussi exprimer ma profonde gratitude à ma famille, belle-famille et mes amis pour leur soutien moral tout au long de ces trois années. Un grand merci à ma sœur Michela et à Bogdan pour avoir été présents lors de ce jour spécial. Merci également à mes meilleurs amis, Marco, Giacomo et Tommaso, qui sont venus de loin pour me soutenir même s'ils ne comprenaient pas le français. Votre présence a rendu cette journée mémorable.

Je remercie tous ceux et celles qui ont croisé mon chemin et contribué, de près ou de loin, à mon développement aussi bien sur le plan personnel que scientifique.

Enfin, je remercie du fond du cœur ma formidable épouse, Anaïs. Sans elle, je ne serais pas la personne que je suis aujourd'hui. Bien plus qu'un soutien inconditionnel, elle a su m'inspirer et rendre le quotidien plus léger. Je suis infiniment reconnaissant pour sa patience et son écoute, pour les encouragements dans les moments de doutes et pour les rires partagés qui ont rendu ces trois années plus douces. Ce succès est aussi le tien.

Contents

General Introduction **1**

1 State of the art **6**

1.1 Electrical machines optimization techniques 6

1.1.1 Parametric optimization 6

1.1.2 Shape optimization 8

1.1.3 Topology optimization 10

1.2 Topology optimization methods 15

1.2.1 ON-OFF method 15

1.2.2 Level-set method 18

1.2.3 Density-based method 20

1.3 Topology optimization for magneto-mechanical problems 22

2 Topology optimization tool **25**

2.1 Problem formulation and computational process overview 25

2.1.1 Problem formulation 26

2.1.2 Computational process overview 26

2.2 Material interpolation 29

2.3 Magnetostatic model 31

2.3.1 Material properties 31

2.3.2 Magnetostatic problem formulation 34

2.3.3 Finite element formulation 35

2.3.4 Quantity of interest 37

2.3.4.1 Magnetic energy 37

2.3.4.2 Electromagnetic torque 39

2.3.4.3 Magnetic forces for vibration analysis 41

2.4 Mechanical model . . . 42
2.4.1 Material properties . . . 43
2.4.2 Mechanical problem formulation . . . 44
2.4.3 Finite element formulation . . . 46
2.4.4 Quantity of interest . . . 48
2.4.4.1 Compliance . . . 49
2.4.4.2 Von Mises stress . . . 50
2.5 Sensitivity analysis . . . 50
2.6 Regularization techniques . . . 52
2.6.1 Density based filter . . . 54
2.6.2 Sensitivity based filter . . . 55
2.6.3 Heaviside projection . . . 56
2.7 Optimization algorithms . . . 56
2.7.1 Generalized Optimality Criteria GOC . . . 57
2.7.2 Method of Moving Asymptotes MMA . . . 58
2.8 Test case example . . . 60
2.8.1 Optimization problem . . . 60
2.8.2 Gradient computation . . . 61
2.8.3 Results . . . 62
2.9 Chapter conclusions . . . 63

3 Magneto-mechanical topology optimization 65
3.1 Case study . . . 66
3.2 Magnetostatic optimization . . . 68
3.2.1 Formulation of the optimization problem . . . 69
3.2.2 Sensitivity analysis for magnetostatic problem . . . 73
3.2.2.1 Mean torque sensitivity formulation . . . 73
3.2.2.2 Energy difference sensitivity formulation . . . 74
3.2.3 Magnetostatic optimization results . . . 75
3.2.3.1 Comparison of average torque and energy formulation . . . 77
3.2.3.2 Average torque formulation results . . . 78
3.2.3.3 Saliency formulation results . . . 81
3.2.4 Magnetostatic optimization section summary . . . 85
3.3 Two-step magneto-mechanical optimization . . . 86

3.3.1 Formulation of the mechanical optimization problem 86
3.3.2 Sensitivity analysis of compliance 90
3.3.3 Mechanical problem optimization results 91
3.3.3.1 Trade-off between magnetic and mechanical performances 96
3.3.4 Discussion on the two-step optimization approach 99
3.4 Coupled magneto-mechanical optimization 100
3.4.1 Formulation of the coupled magneto-mechanical optimization problem . . . 101
3.4.2 Choice of the optimization problem formulation 102
3.4.3 Optimization results 105
3.4.4 Comparison between simultaneous and 2-step magneto-mechanical optimization108
3.5 Chapter conclusions 110

4 Topology optimization and vibration reduction 113
4.1 Vibrations in electrical machine 114
4.1.1 Electromagnetic forces calculation 116
4.1.2 Dynamic mechanical model 119
4.1.3 Modal analysis 120
4.1.4 Modal superposition method 121
4.1.5 Vibration analysis of the stator 123
4.2 Topology optimization for vibration reduction 126
4.3 Application to an electrical machine 129
4.3.1 Formulation of the optimization problem 130
4.4 Vibrational problem results 133
4.4.1 Configuration with boundary conditions 133
4.5 Chapter conclusions 138

Conclusions and perspectives 139

Synthèse en français 145

References 155

List of Figures

1 Design space of optimization methods. 2

2 Number of publications per year related to "electromagnetic topology optimization" based on data from Scopus. 3

1.1 Examples from the literature of geometry parameters used for parametric optimization of synchronous machines. 8

1.2 Examples from the literature of shape optimization of synchronous machines. . . . 9

1.3 Examples from the literature of topology optimization of synchronous machines. . 13

1.4 ON-OFF method with filtering technique applied to an interior permanent magnet motor Watanabe et al. (2018). From the left, the geometry obtained without the filter, the neighborhood filtering technique, and on the right the optimal geometry using the filter. 16

1.5 Examples of ON-OFF based on normalized Gaussians and application to a PMSM. . 17

1.6 Level-set function $\phi(x,t)$ example for a two dimensional problem Chen et al. (2021). 18

1.7 Level-set method applied to optimize a SynRM motor Brun et al. (2024). From the left, the reference machine geometry, the problem initialization, and on the right the optimal geometry. 20

1.8 Illustrations of material distribution (left) and different interpolation functions (right). Highlighted in red the only possible values for ON-OFF method. 21

1.9 Examples of density-based method applications. 22

2.1 Typical flowchart of a density-based topology optimization problem. 27

2.2 Polynomial interpolation with different penalization factor q. 30

2.3 Magnetization curve obtained from Marrocco's formulation. 32

2.4 Comparison between permeability interpolation and reluctivity interpolation using the polynomial formulation. 33

2.5 Non-linear $\mathbf{BH}$ curve obtained for different material densities ρ. 33

2.6 Magnetic energy and co-energy derived from the linear and non-linear $\mathbf{BH}$ curve. . 37
2.7 Air-gap subdivision. 41
2.8 Young's modulus interpolation. 44
2.9 Interface $\partial\Omega$ (in red) between the rotor and the shaft. 48
2.10 Example of checkerboard pattern encircled in yellow. 53
2.11 Example of mesh dependency, geometry obtained with coarse mesh (left) and fine mesh (right). 53
2.12 Example of sensitivity filter applied to a gradient distribution: before the filter (left) and after (right). 56
2.13 Inductance geometry with optimization domain Ω in yellow. 60
2.14 Pareto front for the inductance design. 62

3.1 Machine geometry with the used winding distribution configuration and yellow rotor design space Ω where topology optimization is applied. 67
3.2 Magnetic flux lines obtained by applying the magnetization current I_d (left) and I_q (right), simulated using FEMM 4.2. 71
3.3 Mesh distribution of the motor used for optimization, including the yellow mesh for TO. 71
3.4 Flowchart of the magnetostatic TO procedure, with the different blocks description. 72
3.5 Geometry obtained without a density filter presenting rough surfaces and undesirable artifacts. 75
3.6 Different material distributions used for the initialization of the rotor domain. . . . 76
3.7 Comparison of the average torque value evolution between saliency (P_W) and torque (P_T) maximization problems. 77
3.8 Topologies obtained initializing the optimization problem P_T with **homogeneous material distribution**, from GOC (top) and MMA (bottom) algorithms. 79
3.9 Topologies obtained initializing the optimization problem P_T with **holes distribution**, from GOC (top) and MMA (bottom) algorithms. 79
3.10 Topologies obtained initializing the optimization problem P_T with **d-q axis holes distribution**, from GOC (top) and MMA (bottom) algorithms. 80
3.11 Topologies obtained initializing the optimization problem P_W with **homogeneous material distribution**, from GOC (top) and MMA (bottom) algorithms. 82
3.12 Topologies obtained initializing the optimization problem P_W with **holes distribution**, from GOC (top) and MMA (bottom) algorithms. 82

3.13 Topologies obtained initializing the optimization problem P_W with **d-q axis holes distribution**, from GOC (top) and MMA (bottom) algorithms. 83
3.14 Magnetic optimal geometries (from the saliency formulation) with the definition of the new optimization domain Ω_{air} for the optimization problem P_M. 87
3.15 Flowchart of the 2-step magneto-mechanical TO procedure, with the different blocks description. In the second step the optimization problem P_M is solved. 88
3.16 Rotor displacements of the magnetostatic geometry obtained from one the previous optimization problems (P_W). 92
3.17 Geometries utilized as starting point for the mechanical topology optimization. . . . 93
3.18 Compliance and geometry evolution with the effect of filter radius reduction during the optimization. 93
3.19 Mechanical TO result obtained using GOC and starting from the magnetostatic geometry 3.17a with the associated displacement (b) and Von-Mises stress distribution (c). . . 94
3.20 Mechanical TO result obtained using GOC and starting from the magnetostatic geometry 3.17b with the associated displacement (b) and Von-Mises stress distribution (c). . . 94
3.21 Mechanical TO result obtained using MMA and starting from the magnetostatic geometry 3.17c with the associated displacement (b) and Von-Mises stress distribution (c). . . 94
3.22 Mechanical TO result obtained using MMA and starting from the magnetostatic geometry 3.17d with the associated displacement (b) and Von-Mises stress distribution (c). . . 95
3.23 Magnetic flux distribution before (a) and after (b) the mechanical topology optimization. 95
3.24 Mechanical TO problem (P_M) results obtained from different volume constraints $V_{\%}$. 97
3.25 Material distribution in air barriers areas. On the left side the geometry with $V\% = 3\%$ highlighting the intermediate-density bridges. On the right side the geometry with $V\% = 15\%$ highlighting multi-bridges along the $q-$axis. 98
3.26 Relationship between mechanical volume constraint, average torque and compliance without and with Heaviside density projection. 98
3.27 Magnetic flux distribution comparison with different volume constraints. 99
3.28 Coupled magneto-mechanical topology optimization procedure flowchart. 101
3.29 Geometries obtained from the first optimization problem formulation, respectively with the two algorithms GOC (a) and MMA (b). 104
3.30 Results from the second optimization problem formulation, obtained with GOC algorithm.105
3.31 Optimal magneto-mechanical geometry (a) and convergence evolution of objective function and constraint (b). 105
3.32 Gradients of the magnetostatic function (a) and mechanical function (b). 106

3.33 Magnetic energy difference ($W_d - W_q$) and average torque evolution during the optimization process. 107
3.34 Geometry after the Heaviside density projection, with a full/void material distribution.107
3.35 Pareto front obtained from the two-step approach (varying the mechanical volume constraint) and simultaneous approach (varying the energy constraint). 109

4.1 Overview of the magneto-vibratory analysis. 114
4.2 Radial force distribution for a static rotor position. 116
4.3 Force distributions. 117
4.4 Radial force distribution for a static rotor position. 118
4.5 2D FFT of the forces distribution. 118
4.6 Modes shape of the stator with the associated natural frequencies. 121
4.7 Comparison between the natural mode deformation and the 8th force harmonic deformation with the associated displacement values. 124
4.8 Location of the stator surface points selected for acceleration analysis and respective frequency spectrum of the acceleration response. 124
4.9 Examples of electrical machine topology optimization for vibration reduction in the literature. 128
4.10 Initial configuration for the stator and housing yellow domain Ω_h. 129
4.11 Flowchart of the proposed method, considering the electromagnetic force evaluation step. 132
4.12 Zero displacement boundary conditions applied to the stator base (in green). 133
4.13 Modes shape of the stator considering boundary conditions, and associated natural frequencies. 134
4.14 Comparison between the natural mode deformation and the 8th force harmonic deformation with the associated displacement values. 135
4.15 Resulting housing geometry (a) and convergence evolution dynamic compliance (b). 135
4.16 Comparison between initial and final structure deformation. 136
4.17 Eigenfrequencies evolution for the first five modes. 136
4.18 Acceleration response spectrum comparison of initial and final geometry. 137
4.19 Exemples tirés de la littérature des differentes techniques pour l'optimisation paramétrique des machines electriques. 146
4.20 Illustrations de la distribution des matériaux (à gauche) et des différentes fonctions d'interpolation (à droite). 148

4.21 Géométrie de la machine avec la configuration de distribution des enroulements utilisée et l'espace de conception du rotor jaune Ω où l'optimisation topologique est appliquée. 149
4.22 Géométries obtenues à partir de la même initialisation pour les deux approches différentes. 151
4.23 Différentes étapes de l'analyse des vibrations du stator du moteur électrique analysé.152
4.24 Application de l'optimisation topologique à la conception du carter pour réduire les vibrations. 153

List of Tables

2.1 Parameters for Marrocco's BH curve approximation 32
2.2 Material mechanical parameters 43

3.1 SynRM geometric parameters 67
3.2 Average torque of final geometries obtained from the various initializations and the two algorithms (GOC and MMA). 81
3.3 Energy difference values of final geometries obtained from the various initialization and two algorithms 84
3.4 Average torque comparison between the two problem formulations P_T and P_W . . 84
3.5 Mechanical parameters of the ferromagnetic material and considered speed. 89
3.6 Performances results with the magnetic performances comparison (before/after mechanical optimization) and summary of mechanical criterion values 96
3.7 Final design performance comparison 108

4.1 Mode number and associated natural frequencies 133
4.2 Comparison between initial and final geometry 137
4.3 Comparaison du couple moyen entre les deux formulations de problème 150
4.4 Résumé des performances mécaniques et magnétiques avant et après optimisation mécanique 151

General introduction

The European Union (EU) is undertaking measures to progressively diminish its dependence on fossil fuels, aiming to comprehensively decarbonize the energy and transport sectors comprehensively. The overarching objective is to achieve carbon neutrality by 2050. This ambitious initiative reflects the EU's commitment to mitigating the environmental impact and transitioning towards more sustainable and eco-friendly practices in line with global climate goals Khaleel et al. (2024).

Achieving these goals requires a faster transition to renewable and energy efficiency. In particular, electromechanical conversion devices are indispensable in many practical applications, such as renewable energy systems and electric mobility. As the transition to sustainable energy sources speeds up, the need for these devices is anticipated to increase, emphasizing their vital role in the EU's strategy for reducing carbon emissions.
Electric machines are a prime example of this technological shift. They are gradually replacing combustion engines and hydraulic actuators in numerous areas, such as industrial machinery and transportation.

The increasing use of medium- and high-power electric machines comes with tough design challenges. These machines need to work well under various conditions and meet strict rules on efficiency, noise, and electromagnetic interference. Life cycle optimization, material recycling, and limited resources on specific primary resources like dysprosium due to politics and the market also constitute new challenges when designing electrical machines. Thus, it is crucial to design motors that maximize efficiency in terms of physical performance, energy consumption, and manufacturing costs.

Given the myriad of challenges designers face, there is a pressing need for innovative optimization methodologies in the design of electric machines. Three main strategies exist for optimizing the structure of a device based on the type of parameters chosen:

- **Parametric Optimization**: This approach involves adjusting the dimensions of an existing part, typically using basic geometric specifications. It allows for quick modifications but is limited to defined geometries.
- **Shape Optimization**: In this method, the boundaries of an initial structure are permitted to change, evolving into a design that meets optimal performance criteria while maintaining a consistent topology. That can lead to innovative designs that are not confined by existing shapes.
- **Topology Optimization**: This approach focuses on material distribution within a defined area without requiring a prior structure to guide the process. It allows for a broader exploration of design possibilities, which can yield groundbreaking solutions.

Each optimization approach addresses specific design challenges, and no single method fits all scenarios.

Parametric optimization, often considered the most intuitive approach, adjusts predefined geometrical parameters. Its simplicity ensures that the resulting designs are relatively easy to manufacture. However, its effectiveness is highly dependent on the selected parameters and often only explores a small subset of possible designs, leaving many innovative solutions undiscovered.

In contrast, shape and topology optimization open up the design freedom. Working in a higher dimensional design space allows these approaches to find innovative and unconventional geometries, as illustrated in Fig. 1. While shape optimization refines the contours of existing structures, topology optimization can change the structure itself: removing, adding, or relocating material for the best performance. This high flexibility, however, comes at the price of higher numerical complexity and challenges in manufacturing.

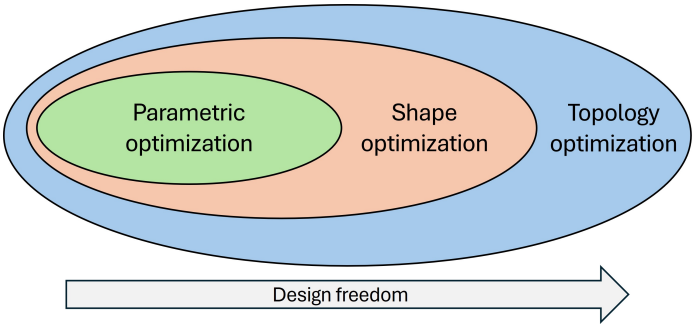

Figure 1: Design space of optimization methods.

The geometrical complexities resulting from topology optimization had significant fabrication challenges due to the inability of traditional manufacturing methods to handle irregular shapes

and structural refinement. Additive manufacturing has, however, changed the equation. It enables the manufacturing of complex designs that were considered impractical before, bringing topology optimization into focus for electric machines. Additive manufacturing bridges the gap from computational innovation to physical realization and allows for new frontiers in high efficiency and innovative motor designs. The need to design electric motors with increasingly higher performance and innovation makes topology optimization an ideal choice for addressing modern engineering challenges.

The growing interest in topology optimization for electromagnetic applications is underlined by the increasing presence in scientific literature, as shown in Fig. 2. This past decade trend indicates increased research publications driven by global efforts toward raising motor efficiency.

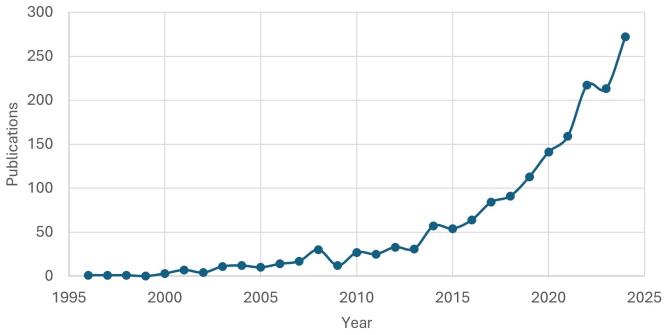

Figure 2: Number of publications per year related to "electromagnetic topology optimization" based on data from Scopus.

It should be noted that similar works have been carried out in parallel with this thesis [Cherrière (2023); Brun (2024); Bergeron (2023)]. The design of electrical machines using topology optimization is indeed a highly active and promising research area. While these studies share similar objectives with the present work, this thesis distinguishes itself in two key aspects. In the following chapters, it will be shown that the proposed methodology introduces a novel magnetostatic problem formulation, offering an alternative to those explored in the aforementioned works. Furthermore, one of the original contributions of this thesis is the explicit integration of vibrational performance criteria into the optimization process, a subject that is not addressed in the referenced works.

Research scope, aim and novelty

This thesis explores advanced topology optimization methods for electric machine design, with a primary focus on addressing the challenge of mechanical integrity through multiphysical optimization. A novel aspect of this work is its exploration of TO techniques aimed at reducing vibrations, a critical factor in durability and acoustic comfort of electric machines. The aim of this research is not only to contribute innovative methodologies but also to provide the reader with all the necessary tools and insights to replicate and extend the proposed approaches.

The work presented in this thesis is organized as follows:

Chapter 1 introduces the motivation and background for using topology optimization in electric machine design, highlighting the limitations of traditional methods such as parametric or shape approaches. It reviews the most common topology optimization techniques and discusses their advantages and limitations in electromagnetic applications. The chapter also identifies key challenges in ensuring mechanical robustness and minimizing vibrations in topology optimization of electrical machines, motivating the need for integrated magneto-mechanical and vibrational formulations.

Chapter 2 will focus on developing a general optimization methodology that can simultaneously address objectives and constraints related to both magnetic and mechanical physics. The process of topology optimization will be introduced and examined in detail. A flowchart outlining the various components of the overall topology optimization will be provided to give a comprehensive overview. The primary focus of this thesis is on magneto-mechanical optimization. Therefore, the finite element formulation will be discussed, including a detailed explanation of the formulation and the quantities of interest. Finally, a simple test case will be presented to illustrate the concepts.

Chapter 3 will apply the methodology described in Chapter 2 to a magneto-mechanical optimization. The electric motor under analysis will be described and the first innovation of this thesis will be introduced. This innovation involves a new problem formulation aimed at improving electromagnetic torque while reducing computation time and the number of finite element analyses (FEAs) required per iteration. A comparison will be made between the traditional average torque approach and the proposed formulation, highlighting their respective advantages and disadvantages. The magneto-mechanical optimization will be applied with two different approaches: a two-step process and a simultaneous optimization. Additionally, two different algorithms will be used and the results of both approaches will finally be compared.

Chapter 4 will begin by examining the origins of vibrations in electric machines and discussing

the methods for conducting mechanical dynamic analysis. It will then explore applications of topology optimization aimed at minimizing vibrational behavior. A specific objective function will be selected to address the optimization problem, focusing on reducing the vibrations in an electric motor caused by resonance. The methodologies and results presented in this chapter will represent a significant advancement in integrating topology optimization with vibrational considerations.

The final section will present the general conclusions of this work, summarizing the main contributions and results, and outlining several promising directions for future research.

Chapter 1

State of the art

1.1 Electrical machines optimization techniques

As previously introduced, the optimization of electrical machines can be approached through three main methods: parametric, shape, and topology optimization. In this section, these techniques will be examined in detail, with a focus on their application to synchronous reluctance machines and, particularly, rotor design optimization.

1.1.1 Parametric optimization

Parametric optimization is one of the most used methods for the design optimization of electrical machines. This approach is widely used in industry and research studies due to its relative ease of implementation. It is used to optimize various components of electric machines, such as stator and rotor shapes, magnet placements and dimensions, wingdings, and more.

Starting from an initial configuration, the designers specifies different design parameters and seeks to optimize these to enhance the chosen performance metrics, for example the overall efficiency, the electromagnetic performances, the vibration reduction, and the thermal behavior.

To solve the optimization problem, in conjunction with the model, two main optimization algorithms categories are utilized: deterministic and stochastic. Some stochastic algorithms are even combined with gradient descent methods to create hybrid approaches that allow for faster optimizations compared to traditional stochastic methods. The use of reduced models, such as response surfaces, Kriging, or models trained by artificial intelligence, is also very common, as discussed in Bramerdorfer et al. (2018).

From the literature, various applications applied to electrical machine can be found. These works vary considerably in terms of the type of machine being optimized, the optimization criterion employed, and the complexity of the problem addressed.

For permanent magnet synchronous motors (PMSMs), one example of research focus is on the magnets. By instance, the optimization of the size and placements of the V-shape magnets was conducted in Chen and Lee (2019) to improve the electromagnetic performances. Other targets can also be found, in Carlsson et al. (2024) the reduction of torque ripple and of the forces acting on the stator teeth was conducted to reduce the sound level and the design parameters were the flux barriers design and cutouts/holes in the rotor. More complex problems, such as multi-physics problems that take into account electromagnetic, thermal and mechanical considerations were treated as shown in Darmani et al. (2024).

Another type of machine is the synchronous reluctance motor (SynRM), where the parametric optimization is mainly applied to the rotor design. This design is challenging due to the complexity of the structure. A variety of barrier shapes exist (fluid, circular, ...), and the sizing and optimization process involves many geometric parameters that are sometimes difficult to define. In Ban et al. (2021), a rotor parametrization method was proposed to significantly reduce the total number of design parameters. While this approach achieved a notable reduction, the number of parameters remained relatively high to ensure an accurate representation of the flux barriers within the rotor geometry. The multi-physics problems for these machines are more related to electro-mechanical considerations, as high operating speeds incur challenging design to ensure the machine's structural integrity. In Nardo et al. (2018) a two-step design procedure was adopted, performing the electromagnetic and mechanical optimization with two different subsets of rotor geometrical parameters. The electromagnetic parameter considered was the average torque, while for the mechanical optimization, the parameter was the maximum stress. Alternatively, in Zhou et al. (2024) a multi-objective optimization was employed to simultaneously improve magnetic and mechanical performances by optimizing the rotor magnetic bridges. The electromagnetic performances considered were the flux density, the average torque, and the torque ripple, while the mechanical performance was represented by the average stress in the magnetic bridges. Some examples of parametric optimization are presented in Fig. 1.1.

While parametric optimization effectively improves electric motor designs, it is often limited by the predefined parameter space. Optimization relies on altering initial geometrical characteristics, so the potential for discovering truly innovative designs is restricted. In other words, this approach can only explore a limited subset of possible solutions, as it does not involve significant structural changes to the machine design.

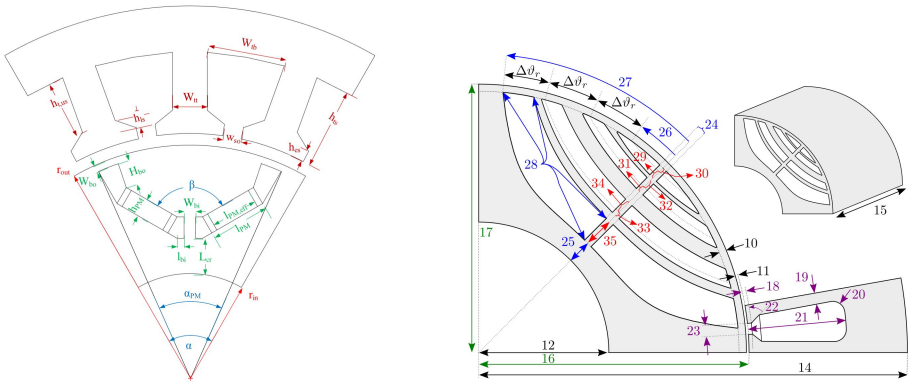

(a) Geometry variables for a PMSM Darmani et al. (2024).

(b) Geometry variables for a SynRM Ban et al. (2021).

Figure 1.1: Examples from the literature of geometry parameters used for parametric optimization of synchronous machines.

Additionally, parametric optimization can suffer from issues such as local optima, where the optimization algorithm converges to a sub-optimal solution due to the complex nature of the design space.

1.1.2 Shape optimization

Shape optimization is an optimization method that involves modifying the boundaries of an initial structure to achieve the optimal design. There are two types: parametric and non-parametric shape optimization.

In parametric shape optimization, the design is described through a finite set of parameters, that define the shape and dimensions. For example, Liu et al. (2021) applied this method to optimize the shape of permanent magnets to achieve a target flux density. This simplifies the design process by focusing on a fixed number of variables. It also applies to shapes represented by splines, which are controlled by specific points.

On the other hand, non-parametric shape optimization deals with infinite-dimensional design spaces. It uses the concept of the shape derivative, a measure of how the objective function changes with infinitesimal changes to the boundary, to explore the optimal shape. In this method, the boundaries are free to evolve iteratively during the optimization process, allowing for a much larger space of achievable designs than in parametric optimization. However, shape optimization does not allow the topology to vary during optimization. Consequently, the solution will always depend on the initial structure chosen.

Although its development is more recent compared to parametric optimization, shape optimization of electrical machines has also been widely discussed in the literature.

In this method, the initial geometry could totally change. For example, when considering the air barrier in a SynRM, the geometry might evolve from a rectangular form to a more fluid, circular shape. However, this method does not permit the complete modification of the geometry, such as altering the number of barriers.

Like parametric optimization, various synchronous motors are used as case studies, mainly focusing on PMSMs and SynRMs.

For PMSMs, the optimization could be applied to distinct motor parts. In Gangl et al. (2015), the electromagnetic performances were improved by modifying the geometry of a specific part of the rotor iron core. Differently, Putek (2016) focused on optimizing the surface magnet rotor poles and the base of the stator teeth to reduce mechanical vibration and acoustic noise caused by cogging torque.

For SynRMs, as for parametric optimization, the design of the flux barriers is the main objective. In Choi et al. (2020), the optimization aimed to increase the average torque and reduce the torque ripple adjusting the shape of two flux barriers. However, it should be noted that mechanical aspects, which are critical for the mechanical integrity of SynRM rotors, were not considered in the study. Although multi-physical aspects are less frequently analyzed, some publications such as Brun et al. (2023) take them into considerations. In this case, the entire rotor was optimized by taking into account both magnetic and mechanical performance, shaping and optimizing all air barriers and bridges. Some examples of shape optimization are presented in Fig. 1.2.

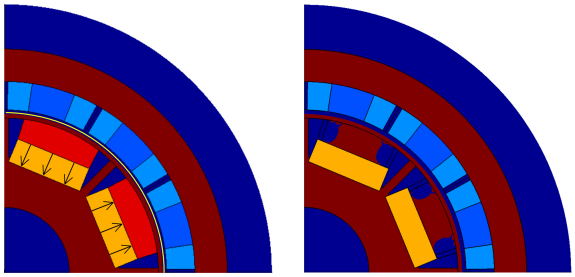

(a) Shape optimization of a PMSM: initial geometry (left) and optimized geometry (right) Gangl et al. (2015).

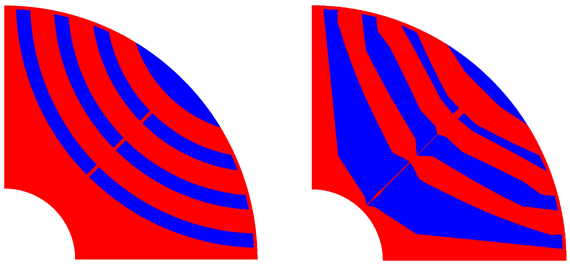

(b) Shape optimization of a SynRM: initial geometry (left) and optimized geometry (right) Brun et al. (2023).

Figure 1.2: Examples from the literature of shape optimization of synchronous machines.

This optimization approach provides more flexibility in achieving optimal designs compared to the parametric method. By allowing the geometry to be continuously adjusted, it enables the exploration of new and unconventional shapes that might not be accessible through parametric methods. However, certain limitations persist, particularly when it comes to achieving a more comprehensive representation of the system's topology.

Similar to the parametric method, the initial definition of the system still imposes constraints on the range of possible investigations. While the boundaries can adopt nearly any shape, the method does not allow for the creation of entirely new material regions within the design space.

1.1.3 Topology optimization

Topology optimization (TO) represents a design approach that aims to identify the optimal material distribution within a specified design space. This method offers significant advantages over traditional approaches, particularly in its design flexibility and capacity to explore unconventional solutions. Unlike parametric optimization, which fine-tunes predefined geometrical parameters, and shape optimization, which refines boundary contours without altering the overall structure, topology optimization surpasses these limitations.

The distinctive aspect of topology optimization lies in its capacity to alter the structure of topology itself. This flexibility allows the discovery of innovative and unconventional configurations that may be impossible to achieve with other optimization techniques, where the topology remains fixed.

The process of TO begins with defining the design space, where the material distribution is optimized. Depending on the approach, one material or multiple materials might be involved. In mono-material topology optimization, the algorithm determines where to place or remove material to achieve the desired performance. Multi-material optimization introduces more complexity by allowing the distribution of different types of materials, which opens up broader design possibilities.

A common approach for distributing the material is through the Finite Element Method (FEM), where the design domain is discretized into small finite elements. Each finite element is assigned a design variable that indicates its physical properties. While the FEM provides the framework for simulation and performance evaluation, it is the optimization algorithm that updates these design variables in order to iteratively improve the material distribution. To achieve such optimized distributions, various topology optimization techniques have been developed.

Among them, popular techniques for optimizing electric machines and electromagnetic devices include Lizarribar et al. (2022): ON-OFF, density-based (also called Solid Isotropic Material with Penalization), and Level-Set methods. These methods can be classified into two categories according to the nature of the density variable, i.e., discrete or continuous. The detailed analysis will be presented in the subsequent section.

The origins of TO lie in structural optimization, dating back to 1904, with Michell's work focused on the identification of the most economical frame structures that were capable of withstanding a balanced system of forces Michell (1904). These early theoretical principles were applied more concretely in the 1970s by Rozvany, who introduced the precise analytical optimization of grid-like structures Rozvany (1972), and later, in Rozvany and Prager (1976) through the discretization of structures.

The foundation of modern numerical topology optimization can be attributed to the groundbreaking work of Bendsøe and Kikuchi (1988), who proposed the homogenization method for structural optimization. This method introduced the concept of modeling material distribution through complex microstructures, allowing intermediate material states between solid and void regions. However, the homogenization approach was mathematically complex and computationally intensive, requiring the management of microscopic material patterns. To address these limitations, Bendsøe (1989) proposed the Solid Isotropic Material with Penalization (SIMP) method a year later. The SIMP method simplified topology optimization by replacing complex microstructure modeling with a continuous material density variable assigned to each element of the structure. This approach not only reduced the computational burden but also made the method more accessible and easier to apply to large-scale problems, marking a major step forward in the evolution of topology optimization.

Over time, topology optimization has spread to a wide range of other physical disciplines, including thermal Fawaz et al. (2022), fluids Chen (2016), acoustic Dilgen et al. (2019), and electromagnetic applications. These developments were further facilitated by the rise of advanced computational power and optimization algorithms, which enabled handling complex, large-scale design problems.

The first application of topology optimization to an electromagnetic problem is found in Dyck and Lowther (1996). In this paper, a magnetic bearing was optimized, using SIMP method, to produce sufficient vertical force on a copper ring to levitate it. After few years, the first applications for the electromagnetic design of rotating electrical machines were described in Im et al. (2003); Byun and Hahn (2001).

Since then, this topic has garnered interest, leading to the publication of many articles. A literature review reveals several publications that serve as references for a global overview of topology optimization. The reference papers for electromagnetic applications are Campelo et al. (2010) and Lucchini et al. (2022). The papers for electric machines fields are Igarashi (2020), Nishanth and Wang (2022) and Mahmoud et al. (2024).

In recent years, TO in electrical machine applications has been a key topic in the literature, primarily focusing on two specific types of machines: PMSM and SynRM. While fewer publications address wound-field synchronous machines Guo et al. (2020); Hidaka (2024), there are more researches on switched reluctance machines Abdalmagid et al. (2023); Gauthey et al. (2024); Sun et al. (2024). Most optimization efforts focus on the rotor part, while the stator geometry has received limited attention but has also been reported Watahiki and Akatsu (2021); Cherrière et al. (2022, 2023a).

Focusing on the two main machine topologies studied in recent years, the primary objectives of nearly all topology optimization studies are to maximize the torque density or to shape the torque profile to reduce the torque ripple. Nevertheless, other performance metrics are also being explored, including iron losses and harmonics content, among others.

Recent works have applied TO to PMSMs and SynRMs with notable results. For example, in Lee and Jang (2023a), the average torque of a PMSM was maximized by considering the current-phase angle in different working regions, such as the maximum torque per ampere and flux weakening. By combining geometry and control optimization, the authors achieved significant improvements in torque density across varying speed ranges. Otherwise, in Hayashi et al. (2022) the optimization not only aimed to optimize the motor torque production but also focused on reducing iron losses and copper losses.

For SynRMs, in Lee and Jang (2023b), used a similar approach to that of PMSMs, aiming to improve the average torque considering the optimal current-phase angle. In this case, the current angle was obtained by interpolating the average torque curve. In addition, the optimization was divided into two phases, firstly improving only electromagnetic performances and secondly including the mechanical analysis. A further example in Hage-Hassan et al. (2023), where TO is combined with additive manufacturing. In this study, the optimization was performed by considering $\mathbf{BH}$ curves obtained through the characterization of different printed ferromagnetic materials. The findings revealed that, although the optimal geometry remained similar across various materials, the thickness of the flux guides differed depending on the specific material properties. Some examples of topology optimization application are presented in Fig. 1.3.



(a) PMSM topology optimization: initial geometry (left) and optimized geometry (right) Hayashi et al. (2022).

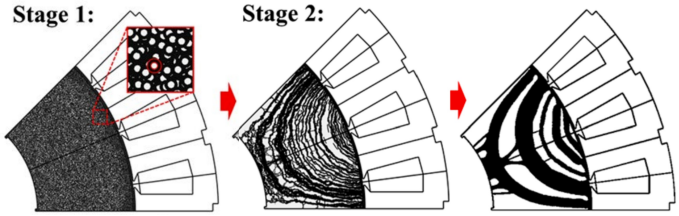

(b) SynRM topology optimization: initial geometry (left), magnetically optimized geometry (center), and magneto-mechanically optimized geometry (right) Lee and Jang (2023b).

Figure 1.3: Examples from the literature of topology optimization of synchronous machines.

Research challenges

Although topology optimization of electric machines is very promising to realize innovative designs, it is important to acknowledge that this approach does present certain challenges. These challenges range from issues related to manufacturability and computational complexity to multi-material integration and mechanical integrity.

Manufacturability: One of the major challenge in topology optimization is ensuring that the optimized designs can be practically manufactured. These designs often feature irregular shapes, rough surfaces, and discontinuous material layouts, making them difficult to produce using conventional manufacturing methods. While additive manufacturing offers the potential to address some of these challenges, its application is not yet mature enough for widespread adoption in electric machine manufacturing Tiismus et al. (2022a). Additionally, the necessary magnetic properties of conventional laminated steel are still far from being achieved Huguet et al. (2021). Furthermore, manufacturing an electric motor requires precise tolerances, just considering the thin air-gap. A slight deviations can impact performances and reliability. Consequently, manufacturability considerations must be integrated into the topology optimization process. In recent years, the use of additive manufacturing has grown in the field of electrical machines, with the winding components that have the most advanced maturity Selema et al. (2022a), and many stator and rotor prototypes Hussain et al. (2023).

Multi-materials: Electric machines are composed of various materials, including copper, iron, and permanent magnets. While optimizing a single material, such as the iron distribution in a SynRM, is relatively straightforward, multi-material optimization presents considerable challenges. The simultaneous distribution of different materials must be optimized, along with their interactions. This includes the behavior of non-isotropic materials like permanent magnets. Additional constraints, such as controlling the magnetization direction, complicate the optimization process compared to single-material scenarios. Recent advancements in multi-material optimization have been discussed, including different types of machines and especially PMSMs due to the presence of the magnets.

In Cherrière et al. (2023b), the rotor was optimized considering iron, air and magnets and in Cherrière et al. (2022) the same author applied the optimization to the stator and thus the materials were the copper winding phases and the iron. Other examples of PMSMs could be found in Gauthey et al. (2022) and Lee and Jang (2022). Hybrid machines with a combined wound-PM rotor are also investigated Hidaka (2022).

While these studies report significant advancement, multi-material optimization remains challenging to implement.

Mechanical integrity: Another critical issue is the mechanical robustness of optimized designs. When the optimization is focused only on electromagnetic performance, the resulting designs can often be structurally weak. For example, in SynRM rotors, the TO process may produce designs without mechanical ribs or thin structural features that compromise mechanical integrity, especially under high rotational speeds. These weaknesses can lead to rotor dynamic instability or mechanical failure. Therefore, mechanical considerations such as stress, strain, and structural compliance must be integrated into the TO process to ensure that optimized designs are not only electromagnetically efficient but also mechanically viable. Recent researches increasingly addresses this limitation by integrating multi-physics optimization, which incorporates both electromagnetic and mechanical constraints into the design process. A detailed analysis of these magneto-mechanical considerations will be thoroughly explored in one of the following sections, being one of the main subjects of this thesis.

Despite these challenges, topology optimization remains a promising approach for electric machine design.

1.2 Topology optimization methods

As previously introduced, the approaches employed in topology optimization can be generally categorized according to the nature of the design variables, which can be either discrete or continuous. This distinction forms the basis for the various optimization methods, each adapted to different challenges and applications.

Among the various TO methods, the most popular approaches for the field of electromagnetic design are the ON/OFF, level-set and density-based methods. These methods differ in their mathematical formulation, material distribution strategies, and computational approaches, offering various trade-offs between accuracy, complexity, and ease of implementation.

In a recent PhD thesis Cherrière (2023), the author analyzed works published between 2018 and 2023 in which topology optimization is applied to electromagnetic devices. The study found that discrete methods, such as ON/OFF approaches using genetic algorithms and NGnet approach, dominate the field, with the 32% of the publications. Density-based methods, such as SIMP, follow closely at 28%, while level-set methods are less commonly used, with only 7% of applications. Despite this distribution, recent trends indicate a growing interest in density-based methods, which seem to be gaining popularity over discrete approaches.

These observations underscore the diversity and evolving nature of topology optimization methods. Each method comes with trade-offs between accuracy, complexity, and ease of implementation, making the choice of method highly dependent on the specific requirements of the optimization problem.

1.2.1 ON-OFF method

The ON-OFF method is one of the simplest approaches for topology optimization. The fundamental principle is to assign a discrete variable to each finite element in the design space. This variable can only take two distinct values, when the material is present (ON or 1), and when the material is absent (OFF or 0). This method is particularly useful for problems where two discrete material are needed, such as in synchronous electrical machine design, where the main materials are air and ferromagnetic iron. This technique can be combined with various numerical optimization methods, such as evolutionary and approximate sensitivity-based algorithms, to find optimal solutions.

This method has the advantage of always producing well-defined materials throughout and at the end of the optimization process. On the other hand, one of the major drawbacks of the

ON-OFF method is its tendency to leads to discontinuous shapes (typically called checkerboard pattern) that are not easily manufacturable or even mechanically infeasible.

ON-OFF method, due to its simplicity and ease of implementation, has been used in the design of electrical machines. One of the earliest applications is found in Im et al. (2003), where it was applied to the design of a brushless motor. Many other applications have since been documented in the literature.

In Watanabe et al. (2018), an interior permanent magnet motor was optimized using an immune algorithm de Castro and Timmis (2002). As the initial shapes obtained were too complex and difficult to manufacture, a filtering process that checks the neighborhood of each mesh element prior to material assignment was introduced to smooth the geometry, see Fig. 1.4. Similarly, in Lee et al. (2021), a stochastic genetic algorithm was applied to optimize the rotor air barriers of a SynRM. The resulting designs exhibits rough surfaces, which pose similar challenges to the one addressed in Watanabe et al. (2018). Here, another "contour-based" smoothing technique was used in post-processing to address these issues, improving fortuitously in the process both the average torque and torque ripple.

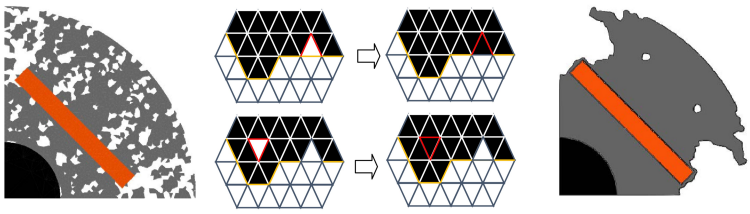

Figure 1.4: ON-OFF method with filtering technique applied to an interior permanent magnet motor Watanabe et al. (2018). From the left, the geometry obtained without the filter, the neighborhood filtering technique, and on the right the optimal geometry using the filter.

These examples highlight the necessity of incorporating filtering techniques and post-processing to the ON-OFF method to ensure that designs are smooth and manufacturable. These discontinuities and checker-boarding are caused by the absence of relationship in between neighboring elements. To address these challenges more effectively, recent studies propose expanding the ON-OFF method with other techniques that take into account this neighborhoods relation.

One effective strategy to improve the ON-OFF method is to introduce spatial correlation between neighboring elements, thereby preventing discontinuities and checkerboard patterns. This can be achieved by using a weighted sum of basis functions to define the material distribution across the design domain, rather than treating each element independently. In this approach, the material state at a given location is not controlled directly by a single design variable assigned

to that element. Instead, it is influenced by a combination of nearby design variables, weighted by smooth basis functions. This overlapping influence introduces a natural smoothness into the material boundaries. A well-known example of this concept is the Normalized Gaussian Network (NGnet), in which each basis function is a normalized Gaussian centered at specific control points in the domain. The overall material distribution is then expressed as a linear combination of these Gaussian functions, as illustrated in Fig. 1.5a. This approach was first proposed by Sato et al. (2015a) for the optimization of a SynRM. Since then, it has been demonstrated its effectiveness in topology optimization Igarashi (2020); Sasaki and Igarashi (2018).

In Otomo and Igarashi (2021), a Gabor filter was proposed in conjunction with the NGnet method to optimize a SynRM, similarly to the first paper. The Gabor filter was shown to produce designs with significantly lower torque ripple compared to conventional NGnet, improving the method.

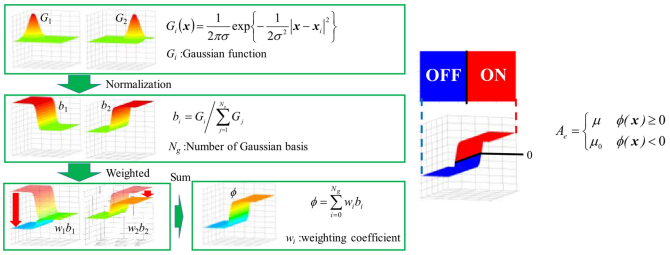

(a) ON-OFF based on normalized Gaussians Sasaki and Igarashi (2018).

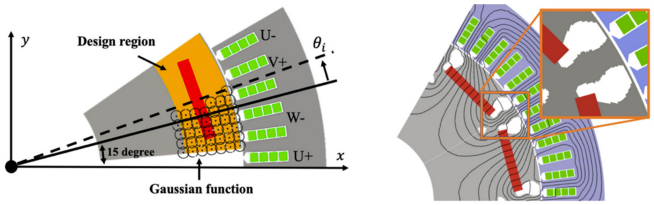

(b) Optimization result using NGnet applied to a PMSM Hayashi et al. (2023).

Figure 1.5: Examples of ON-OFF based on normalized Gaussians and application to a PMSM.

In recent studies, NGnet has been applied to optimize targeted rotor regions in PMSMs. For example, in Hayashi et al. (2023) and Guo et al. (2023b), the optimization was restricted to specific areas of the rotor rather than the entire structure, as shown in Fig. 1.5b. This focused approach simplifies the optimization process by reducing computational complexity.

Another method is the Bi-directional Evolutionary Structural Optimization (BESO) Yang et al. (1998). This technique is an improvement over the conventional ON-OFF method by using sensitivity analysis to guide material updates, unlike NGnet, which models material states continuously using Gaussian functions. In BESO, elements are ranked based on their sensitivity, with low-performing solid elements replaced by air and high-performing voids filled with material. For electrical machines, BESO was used in Garibaldi et al. (2019) and Hage-Hassan et al. (2023).

Multi-material topology optimization based on the ON-OFF technique has also been explored, typically applied to PMSMs. For example, a multi-material TO with three materials (air, iron and magnets) was employed in Sato et al. (2015b) to optimize the rotor shape to maximize the average torque with constraints on the permanent magnet volume. In Hidaka (2024), four materials (air, iron, magnets and coils) were considered for a hybrid wound field motor with permanent magnets.

1.2.2 Level-set method

The level-set method for topology optimization, first introduced in Osher and Sethian (1988), represents a fundamentally different approach compared to traditional methods. Instead of directly assigning material properties to elements in the design domain, the level-set method implicitly defines the geometry of the structure by using a continuous scalar function, known as the level-set function, typically denoted with $\phi(x,t)$. This level-set function is defined over the entire design domain and is used to distinguish between material and void. The function takes positive values in regions filled with material, negative values in void regions (typically air), and zero along the material boundaries. The material interface is represented by the zero level set, where $\phi(x,t) = 0$. This function is illustrated in Fig. 1.6 and formulated as follows:

$$\phi(x,t) = \begin{cases} \phi(x,t) > 0 & \forall x \in \Omega \setminus \partial\Omega \text{ (solid material)}, \\ \phi(x,t) = 0 & \forall x \in \partial\Omega \text{ (boundary)}, \\ \phi(x,t) < 0 & \forall x \in D \setminus \Omega \text{ (air)}. \end{cases} \tag{1.1}$$

where, x denotes the spatial coordinates, t is a pseudo-time variable that represents iterations of the optimization process, D is the entire design domain, Ω is the subdomain occupied by the material, and and $\partial\Omega$ is the boundary interface. The concept of "time" here does not refer to physical time but to the evolution of the design through optimization iterations.

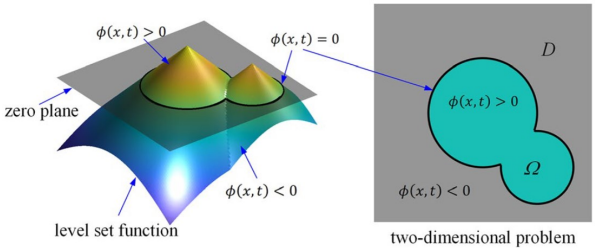

Figure 1.6: Level-set function $\phi(x,t)$ example for a two dimensional problem Chen et al. (2021).

The evolution of the material boundary is governed by the Hamilton-Jacobi transport equation:

$$\frac{\partial \phi}{\partial t} + \mathbf{V} \cdot \nabla \phi = 0 \tag{1.2}$$

where $\mathbf{V}$ is a velocity field that drives the motion of the interface. This velocity field is typically derived from shape derivatives, which quantify how the objective function changes with respect to perturbations in the shape Allaire et al. (2002). In essence, the level-set function evolves smoothly under the influence of these shape sensitivities, gradually deforming the material boundaries to improve performance according to the optimization objective.

One of the major strengths of the level-set method is its ability to produce smooth, well-defined structural boundaries, naturally avoiding issues such as checkerboard patterns and intermediate material densities that are common in density-based methods. However, it also has limitations. A key drawback is its difficulty in introducing new holes or disconnected regions during optimization, unless the method is augmented with topological derivatives or initialized with internal voids. As a result, the final design can be strongly dependent on the initialization.

From a computational perspective, the level-set method is more complex than other approaches. It often requires re-initialization or re-meshing to maintain numerical stability and accuracy, particularly in conformal implementations where the mesh must conform to the evolving material boundaries Kuci et al. (2021).

Despite these challenges, there are numerous case studies in the literature demonstrating the effectiveness of this method for electric machines optimization. One of the earliest examples of TO using the level-set method is found in Kim and Park (2010), where it was applied to the rotor design of a SynRM motor with the objective of maximizing the energy difference. Another application to SynRM was presented in Yamashita and Okamoto (2020), where both the rotor and stator end tooth were optimized simultaneously to improve average torque and reduce iron losses. More recently, in Brun et al. (2024), the method was used to minimize the volume of the rotor, with constraints on average torque and torque ripple, ensuring the optimized design maintained at least the same torque performance as the reference machine, see Fig. 1.7. In Kuci et al. (2021), magneto-mechanical aspects were optimized, and mesh re-meshing was implemented, illustrating the complexity of the method's implementation. There are relatively fewer studies focused on PMSMs. In Gangl et al. (2016), a rotor region was optimized using topological sensitivity to achieve low total harmonic distortion of the radial component of the magnetic flux density in the air gap while preserving a large amplitude of the first harmonic. Additionally, Choi et al. (2011) focused on reducing torque ripple by optimizing the design of the

stator tooth shoe.

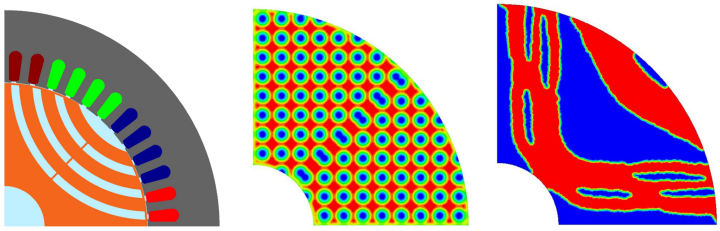

Figure 1.7: Level-set method applied to optimize a SynRM motor Brun et al. (2024). From the left, the reference machine geometry, the problem initialization, and on the right the optimal geometry.

1.2.3 Density-based method

The density-based method, also known as SIMP method, was originally derived from the homogenization method Bendsøe and Kikuchi (1988). In the homogenization approach, the material is distributed through microstructures, which are typically rectangular cells with rectangular holes. The dimensions and angle of rotation of each hole serve as the design variables for optimization. In the homogenization approach, a cell is considered to be solid when the hole disappears, and void if the hole has the same dimensions as the cell. This method is complex in both theoretical and numerical terms. With three variables for each cell, it requires the introduction of numerous optimization variables.

To overcome these problems, the SIMP method was developed as a simplified alternative to the homogenization approach Bendsøe (1989), eliminating the need to explicitly define microstructures at the microscopic level.

With SIMP method, the material properties in each element of the design domain are described using a continuous variable, called density variable ρ. The values of ρ varies between 0 (void) and 1 (solid material). Referring to the previously presented ON-OFF method, the use of continuous variable enable the transformation of the discrete TO problem into a relaxed problem that allows intermediate values between 0 and 1, as shown in Fig. 1.8. Due to the continuous nature of the problem, deterministic algorithms based on gradient descent are mainly associated with the numerical resolution of density methods.

The relationship between density and the associated physical property is obtained using an interpolation function (see Fig. 1.8), also called mapping function. In the literature, many interpolations can be found Mohamodhosen (2017). In order to provide a physically interpretable

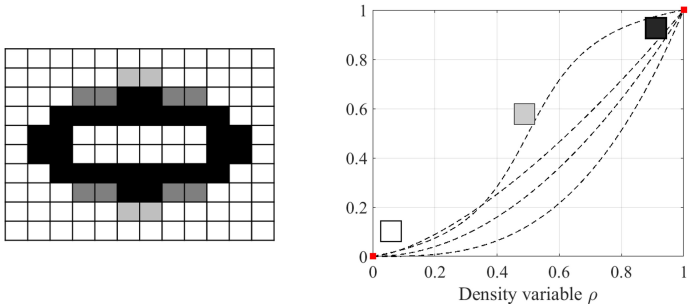

Figure 1.8: Illustrations of material distribution (left) and different interpolation functions (right). Highlighted in red the only possible values for ON-OFF method.

solution to the TO problem, the intermediate materials must have disappeared in the final result, which is not usually the case. To force them to disappear, a widely used solution consists of penalizing the interpolation function. With penalization, the intermediate materials become less "efficient".

The advantages of the SIMP method are its highly flexibility as it can be applied to a wide range of optimization problems. It is compatible with gradient-based optimization algorithms, ensuring efficient convergence even for large-scale problems. Multi-material application are also been investigated.

Despite its advantages, this method has some inconveniences. The final design may presents intermediate densities that are difficult or impossible to manufacture. Additionally, the SIMP method may generate designs with sharp corners or checkerboard, similarly to ON-OFF method, which are also challenging from a manufacturing point of view. Several solutions are available to mitigate the impact of these issues Lucchini et al. (2022). These are typically based on filtering of the density and/or its gradient, with the objective of regulating the distribution, and projection techniques to project the density onto a discrete distribution. These regularization techniques will be detailed in Section 2.6.

The density-based method has been successfully employed in the design of electrical machines. One of the earliest applications can be identified in Wang et al. (2004), where it was used to optimize a single-phase induction motor for a rotary compressor, aiming to reduce the oil circulation rate while maintaining the rated torque. The density-based approach has become increasingly popular in recent years, with significant advancements and new applications emerging. The latest state of the art advances demonstrated the capability of efficiently optimizing the rotor of SynRM, as shown in Li et al. (2023a), where the method was used to improve both electromagnetic performances and mechanical compliance, including output torque, mechanical stiffness, strength, and rotor weight. This study also examined how variations in the current

angle affected the resulting geometry. In Guo et al. (2023a), a flat bar, V-shaped PMSMs, and a Wound-Field Synchronous Machine (WFSM) were optimized, combining parametric and topology optimization (see Fig. 1.9a). For the PMSMs the magneto-mechanical performance were optimize, for the WFSM, in addition, the copper losses of the rotor are constrained. In Gauthey et al. (2024), a novel objective function was proposed to reduce the torque ripple in a switched reluctance machine. This function targeted specific harmonics, allowing for more precise control over both rotor design and the harmonic content of the torque during ripple minimization. Moreover, in Cherrière et al. (2024) an entire multiphase reluctance machine with no initial information on the internal topology of the rotor and the stator was optimized, as shown in Fig. 1.9b, demonstrating the strong potential of multi-material optimization.

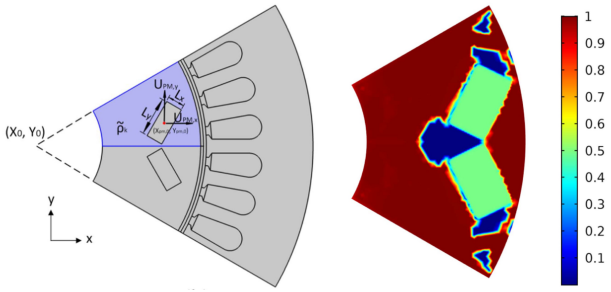

(a) Combined parametric and topology optimization Guo et al. (2023a). Initial geometry with variables parameters for the permanent magnets (left) and optimized geometry (right).



(b) Multi-material TO of entire multiphase machine Cherrière et al. (2024). From the left: initial design, 1-phase, 3-phase, and 5-phase optimization results.

Figure 1.9: Examples of density-based method applications.

These studies highlight the adaptability of the density-based method for complex, multi-material designs in electrical machine optimization.

1.3 Topology optimization for magneto-mechanical problems

The TO of electrical machine designs, when focused exclusively on enhancing electromagnetic performances, can result in structurally weak designs. For example, consider the design of a SynRM rotor optimized only for magnetic performance. Electromagnetic torque reaches its

maximum when there is no flux leakage from the d-axis to the q-axis within the rotor. As a result, a topology optimization that prioritizes only magnetic aspects may produce a rotor geometry that lacks adequate mechanical supports in the flux barriers. This design approach can be impractical regarding both mechanical integrity and manufacturing feasibility. Similarly, for PMSMs, the optimized rotor shapes may include several air gaps or voids, compromising the rotor's structural strength.

Therefore, structural requirements must be included in the TO problem to ensure that the optimized geometry is mechanically robust.

An initial discussion on magneto-structural optimization was presented by Yoo in Yoo (2002). In this work, the homogenization method was employed to optimize the stator of a switched reluctance motor, with the objective of reducing the deformation caused by the magnetic harmonic excitation by minimizing the mean compliance. However, this early work did not account for torque, a crucial aspect of motor design.

Subsequent studies, adopting a multi-physics approach, have predominantly focused on the magneto-structural optimization of actuators, as seen in Shim and Wang (2008); Shim et al. (2008); Lee and Kikuchi (2010). In these studies, the authors similarly employed density-based techniques to reduce the compliance of an electromagnet subjected to local magnetic forces, while simultaneously maximizing these forces.

One of the first works to consider simultaneous magneto-mechanical topology optimization of an electric machine was Sawada et al. (2019). This paper combines electromagnetic and structural analyses to optimize the rotor structure of the SynRM, achieving improved torque and rigidity under centrifugal force. In the same year, Credo et al. (2019) optimized an initial SynRM rotor design that lacked radial ribs. However, unlike Sawada et al. (2019), their study employed a sequential approach to optimize the electromagnetic and mechanical performances, rather than a simultaneous one. Furthermore, topology optimization was applied only to the mechanical aspects of the design.

Magneto-mechanical topology optimization is currently one of the most promising and challenging research fields in the design of high-performance electrical machines. The need to simultaneously meet electromagnetic and mechanical requirements has led to increasingly complex multi-physics optimization problems, necessitating robust methodologies capable of addressing various and often conflicting objectives. Integrating these multi-physical aspects is crucial for developing high-performance, mechanically robust electric machines capable of

meeting the demanding requirements of modern applications.

Driven by these challenges, the work presented in this thesis focuses on developing a methodology for magneto-mechanical topology optimization. The aim is to develop a practical computational framework to address the often conflicting needs of electromagnetic performance and mechanical integrity in electric machines.

The following chapter will introduce this topology optimization tool, providing a detailed overview of each block in its flowchart, with special attention given to both magnetostatic and mechanical models.

This methodology constitutes the backbone of the entire thesis and allows for the case studies and original contributions that will be explored in the subsequent chapters.

Chapter 2

Topology optimization tool

This chapter introduces the essential topology optimization (TO) tool that forms the foundation for the methods discussed in this thesis. The process of creating a topology optimization method can be broken down into three parts: defining the topology optimization problem, developing the finite element model and choosing an optimization algorithm. For this thesis, a homemade Matlab program is used, and it incorporates the entire TO method. This approach makes it easier to identify the source of convergence problems during the development of the optimization methods. Furthermore, it allows for complete freedom in selecting the multiple parameters that constitute the optimization problem.

As presented in Chapter 1, there are two main approaches for the variable design definition: the discrete approach and the continuous approach. In this thesis, a continuous approach will be used, and more precisely, the density-based method, proposed by Bendsøe, called Solid Isotropic Materials with Penalization (SIMP) Bendsøe (1989). The optimization process illustrated in the next parts is based on this method.

2.1 Problem formulation and computational process overview

Topology optimization is a design methodology that allows designers to achieve optimal geometry by distributing materials within a predefined design space. The material is distributed to meet specific performance criteria while satisfying constraints, integrated in the optimization problem. This section explains the problem formulation and computational process of the TO developed in this thesis.

2.1.1 Problem formulation

As we introduced in the previous chapter, topology optimization deals with the modification of the material distribution in a defined domain, i.e., material can be removed or added. Denoting with ρ the material distribution at any point of the design domain, the general optimization problem can be written as:

$$\begin{aligned} \min_{\rho \in \mathbb{R}^n} \quad & f_0(\chi(\rho), \rho) \\ \text{s.t.} \quad & g_i(\rho) \leq 0, \qquad i = 1, 2, ..., m \\ & g_h(\chi(\rho), \rho) \leq 0, \qquad h = 1, 2, ..., e \\ & \rho_{\text{min}} \leq \rho_j \leq \rho_{\text{max}} \quad j = 1, 2, ..., n \end{aligned} \tag{2.1}$$

where $f_0(\chi(\rho), \rho)$ is a single or multi-term objective function, usually identifying performance metrics such as, considering electrical machine, maximizing the system's energy, or maximizing the mean torque, or reducing the torque ripple. The functions $g_i(\rho)$ and $g_h(\chi(\rho), \rho)$ typically represent design or physical constraints, and are normally written in inequality form. The vector $\rho = (\rho_1, ..., \rho_n) \in \mathbb{R}^n$ contains the density design variables, which are usually combined with the material parameters, and has lower and upper bounds identified by ρ_{min} and ρ_{max}, respectively. This vector dictates the material distribution within the design domain and wields considerable influence over the optimization process, driving the evolution of optimal designs.

The state field $\chi(\rho)$ satisfies a linear or non-linear state equation depending on ρ. Evaluating it typically involves solving a partial differential equation, which is most commonly done using the finite element method.

The choice of objective function and constraints is a crucial step in topology optimization, as the inappropriate formulation could drive into an infeasible material distribution.

2.1.2 Computational process overview

The computational process to solve the topology optimization problem involves several key steps. In this section, these steps are analyzed and explained to provide the reader with an overview of topology optimization. This discussion will focus specifically on the multi-physics optimization of a synchronous reluctance motor, which is the subject of this thesis. Fig. 2.1 synthesizes an example of the general topology optimization problem resolution.

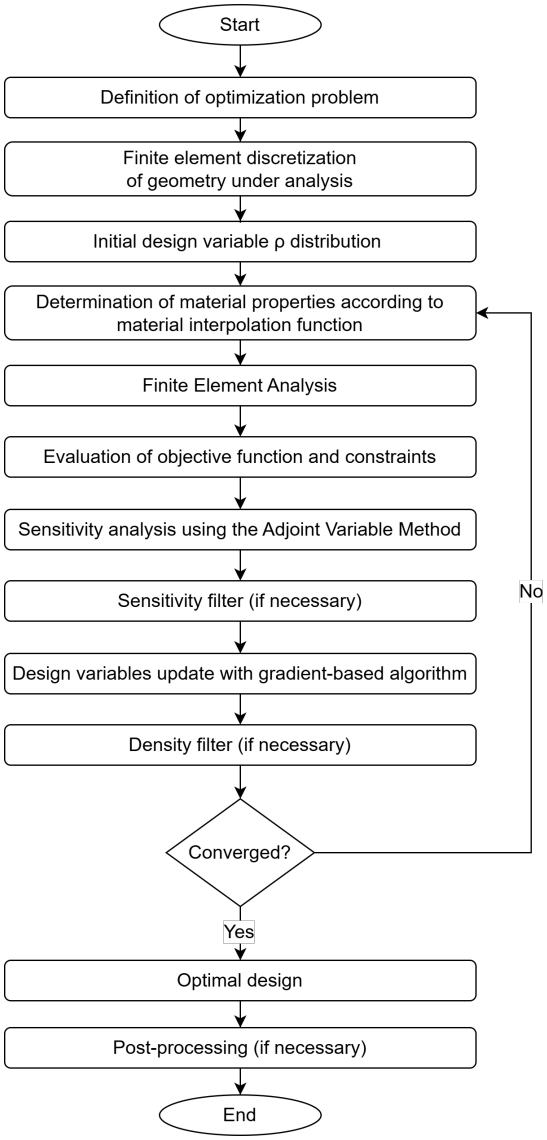

Figure 2.1: Typical flowchart of a density-based topology optimization problem.

After the problem definition, the entire geometry under analysis is discretized into a finite element mesh, used to solve the partial differential equations of the physical problem. Each element of the mesh in the optimization domain is related to a design variable ρ_i. The degree of refinement applied to the mesh dimension has a direct impact on the precision and reliability of the optimization outcomes. Consequently, the most appropriate mesh size for a given problem must be carefully determined considering the problem complexity and the available computational resources. Once the mesh is in place and the initial density variable distribution has been determined, it is necessary to assign the material properties. It is assumed that a mesh cell is occupied by material when the density is at its maximum value, ρ_{max}, while a cell that is void would have a minimum density, ρ_{min}. As intermediate densities are employed, it is important to calculate

the precise material properties. Material interpolation schemes are then used to determine the material characteristics for intermediate density levels.

It is then possible to perform the Finite Element Analysis (FEA) and compute the generic state field χ. This involves solving partial differential equations from diverse fields such as electromagnetic, structural mechanic, fluid dynamic and thermic that govern the physical behavior of the system under study. Once obtained χ, the objective function and constraints can be evaluated. The sensitivity analysis of both objective function and constraints is performed, this step is essential to update the solution in gradient-based optimization methods. Different techniques exist for the gradient computation, but only one is suitable for topology optimization problems, due to the elevate number of design variables. The widely used technique is the Adjoint Variable Method (AVM) Cea (1986). The main advantage of AVM is its efficiency, compared to the other techniques. Indeed, with the adjoint method, it is possible to estimate the sensitivity of the objective function relative to any number of design variables using only one additional numerical analysis, i.e., the adjoint analysis.

Before the optimization algorithm with the update of the design variables, different filters can be applied. Generally, a sensitivity filter is applied once the gradients are calculated and thus before the optimization algorithm. Another filter that can be used is the density filter, which helps the convergence of the results to a void/full material distribution. The density filter is usually applied after the design update. These filters are usually utilized to avoid different numerical problems in topology optimization, such as checkerboard patterns, mesh dependence, and the appearance of disconnected elements Svanberg and Svärd (2013).

With the gradient information, the next step is the update to design variables. The optimization algorithm usually associated to the density-based method is a gradient-based algorithm. At this point, the choice of the optimization algorithm for the formulated optimization problem is another important stage. In this work, two algorithms will be used: GOC (Generalized Optimality Criteria) and MMA (Method of Moving Asymptotes).

This procedure is repeated until the optimization converges. However, the result sometimes presents some intermediate materials or rough surfaces. A post-processing is then necessary to improve the design for the manufacturability.

This whole computational process forms the basis for implementing topology optimization methodologies. Here it is presented the general overflow, but it could be adapted and changed based on the optimization problem. In this thesis, the optimization of a synchronous reluctance motor will be addressed through topology optimization, and the previously computational process will be adapted for two main physics, magnetostatic and mechanical.

In the following sections, the main blocks of the flowchart will be presented in detail, with a focus on the main objective of this thesis work.

2.2 Material interpolation

As mentioned before, the first step of topology optimization problem is the initialization of the optimization domain with an initial design variable distribution $\rho = (\rho_1, ..., \rho_n) \in R^n$. The design variables are continuous, with $\rho_{\text{min}} \leq \rho_j \leq \rho_{\text{max}}$, and assigned to each mesh element. The physical properties of each element, next utilized in the finite element analysis, are thus defined as a function of the continuous design variable ρ using an interpolation function. This interpolation involves a representation of the material distribution within the design space as a continuous function of ρ varying between $\rho_{\text{min}} = 10^{-3}$ and $\rho_{\text{max}} = 1$. The value of ρ_{min} is used to avoid singularity problems and numerical issues when $\rho_{\text{min}} = 0$.

A penalization parameter, denoted as q, is also used and play a crucial role in the SIMP method as it helps to avoid intermediate densities in the final design. In the context of electrical machine, a density value of 1 indicates that the element is filled with ferromagnetic material, while a density value of 10^{-3} indicates that the element is void and filled with air. Multi-material interpolation also exists as shown in Cherrière et al. (2023b), but it is not the topic of this thesis. A judicious selection of the interpolation function and penalization factor is essential to achieve the optimal material distribution.

In the literature we can find different interpolations functions and methods, a summary list can be found in Mohamodhosen (2017). Considering the density-based optimization problem and particularly the SIMP method, the first material interpolation that was introduced is the power-law interpolation Bendsøe and Sigmund (1999), written as:

$$p(\rho) = p_1 \rho^q \tag{2.2}$$

where $p(\rho)$ is the interpolated material property, p_1 is the material property of the solid phases, and q is the penalization coefficient.
Another form of power-law interpolation, derived from the previous one, is given by:

$$p(\rho) = p_0 + (p_1 - p_0)\rho^q \tag{2.3}$$

This material interpolation, also called polynomial, is the most utilized in topology optimization. The material property p_0 represents here the void phases (air). Due to the continuous nature

of ρ, regions with intermediate densities are generated during the optimization process. These intermediate regions, also called "gray scale" regions, usually correspond to unmanufacturable material due to their intermediate physical properties. To eliminate this intermediate material, the normalized material density is penalized into either 1 or 0 by the factor q. The challenge then consists in properly adjusting the penalization parameter corresponding to each optimization problem specification, ensuring that the interpolated material properties are physically meaningful, and that the optimization problem is well-posed. Typically, researchers choose values of q between 1 and 5, with $q = 1$ representing linear interpolation and $q = 3$ representing the widely used SIMP interpolation scheme in mechanical topology optimization. An example is illustrated in Fig. 2.2, demonstrating the correlation between the penalization parameter and the resulting material properties.

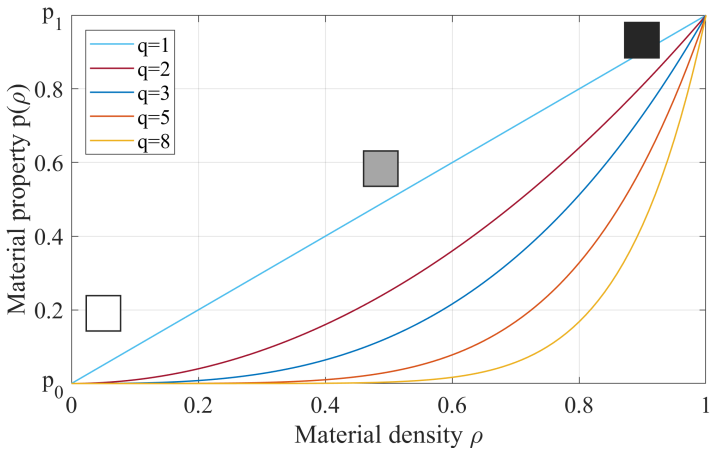

Figure 2.2: Polynomial interpolation with different penalization factor q.

The value of q could also be greater, as found in the literature Lee and Jang (2023a). For the magnetostatic and mechanical problem that will be presented in the following sections, the choice of this parameter will be discussed as well of the full material and void properties p_1 and p_0.

The finite element analysis is one of the key points for a TO problem. The optimization domain needs to be discretized into finite elements in order to associate at each mesh a density variable. In this work, the geometry mesh is generated through the open source software FEMM 4.2 Meeker (2010) and then read and used in the Matlab code. Two main physical behaviors will be considered in this thesis: magnetostatic and mechanical.

2.3 Magnetostatic model

This section outlines the magnetostatic model, following three key steps. First, material interpolation is employed to represent the material properties. Next, these interpolated properties are incorporated into the finite element formulation, where the governing physical equations are applied and finite element analysis is used to solve the electromagnetic problem. Finally, the solution is used to compute the quantities of interest. The magnetostatic model is crucial for the accurate computation of the magnetic behavior and the analysis and the optimization of the performance of electric machines and other electromagnetic devices.

2.3.1 Material properties

The ferromagnetic material is characterized by the relation between the magnetic field $\mathbf{H}$ and the magnetic flux density $\mathbf{B}$. Considering an electromagnetic problem, this relation can be linear or non-linear, but in the context of electric motors the non-linear relation is utilized. Only isotropic materials are being considered, ensuring that these two fields remain parallel, while any potential effects of hysteresis are neglected.

For a linear material, only the relative iron reluctivity (ν_r) is needed. Assuming the absence of permanent magnetization, we have that $\mathbf{H} = \nu\mathbf{B}$, where $\nu = \nu_r\nu_0$ is the magnetic reluctivity that depends on ν_r of the considered material, and $\nu_0 = 1/(4\pi 10^{-7})$ $(\mathbf{m}/\mathbf{H})$ the reluctivity of the vacuum. For non-linear materials, the reluctivity depends on the magnetic flux density, $\nu(|\mathbf{B}|)$. In a low magnetic field, the magnetic flux density $\mathbf{B}$ is proportional to magnetic field $\mathbf{H}$, the reluctivity is then constant. In a high magnetic field, the material is characterized by the magnetic saturation, therefore the magnetic flux density $\mathbf{B}$ increases less as magnetic field $\mathbf{H}$ increases. In this case, when the considered material is non-linear and reluctivity depends on $\mathbf{B}$, several mathematical and physical models exist to represent it. In this work, a modified version of the Marrocco's $\mathbf{BH}$ curve interpolation was chosen Marrocco (1977). This method ensures a smooth and accurate representation of the non-linear behavior, which is crucial for the stability and accuracy of the finite element analysis and then for the convergence of the non-linear magnetostatic model. The Marrocco's $\mathbf{BH}$ approximation divides the magnetization curve in three different parts as:

$$\nu(|\mathbf{B}|) = \begin{cases} \nu_0 \left(\epsilon + (c-\epsilon)\frac{|\mathbf{B}|^{2\alpha}}{\tau+|\mathbf{B}|^{2\alpha}}\right) & \text{if } |\mathbf{B}| \leq B_{\max}, \\ \nu_0 \left(1 - \frac{M_s}{|\mathbf{B}|}\right) & \text{else if } |\mathbf{B}| > B_s, \\ \exp\left(\frac{\gamma(|\mathbf{B}|-\beta)}{|\mathbf{B}|}\right) & \text{otherwise} \end{cases} \tag{2.4}$$

where $B_s = \beta + \frac{\log(\nu_0/\gamma)}{\gamma}$ and $M_s = B_s + \frac{1}{\gamma}$. The coefficients ξ, ϵ, α, τ, γ, β are empirical parameters derived from fitting the interpolation to experimental data. Table 2.1 shows the value of the coefficients used in this work, these parameters are obtained from the interpolation of the curve of M-27 steel found in FEMM 4.2 material library.

Table 2.1: Parameters for Marrocco's BH curve approximation

Parameter	Value
ξ	$1.90 \cdot 10^{-2}$
ϵ	$1.57 \cdot 10^{-4}$
α	6.83
τ	$4.13 \cdot 10^{3}$
γ	4.85
β	$-1.30 \cdot 10^{-1}$
$B_{\max}$	$1.8\,[\mathrm{T}]$

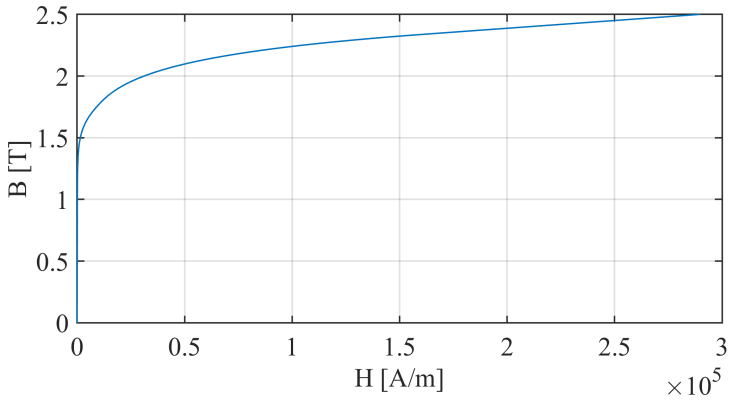

Figure 2.3: Magnetization curve obtained from Marrocco's formulation.

The coefficients of the Marrocco's equations can be found with a regression function, fitting real data points from manufacturer material curve and adjusting in function of the $\mathbf{BH}$ material curve. With the ferromagnetic material properties and the interpolation scheme previously presented, we can define the one used for the magnetostatic model. Two possibilities are reported in the literature to interpolate the magnetic properties of intermediate materials. We can interpolate with either the magnetic permeability μ as in Wang and Kang (2002) or the magnetic reluctivity $\nu = \mu^{-1}$ as in Ma et al. (2020). In this thesis, we choose to interpolate ν. This interpolation provides robust and stable results, while eliminating the need to adjust the penalization factor Choi and Yoo (2008). The material properties for the solid and void phases are respectively the non-linear reluctivity $\nu(|\mathbf{B}|)$ and the air reluctivity ν_0. With the polynomial interpolation formulation (2.3) it results as:

$$\nu(\rho) = \nu_0 + (\nu(|\mathbf{B}|) - \nu_0)\rho^q \tag{2.5}$$

This formulation is also called reluctivity mapping, proposed the first time for electromagnetic topology optimization in Choi and Yoo (2008). In this case, the penalization parameter is generally $q = 1$. This value is used because the interpolation of air and ferromagnetic material results in a "naturally" penalized curve, compared to the classical polynomial interpolation presented earlier in Fig. 2.2. This is not the case when permeability is used. The comparison of these two interpolation method is shown in Fig. 2.4.

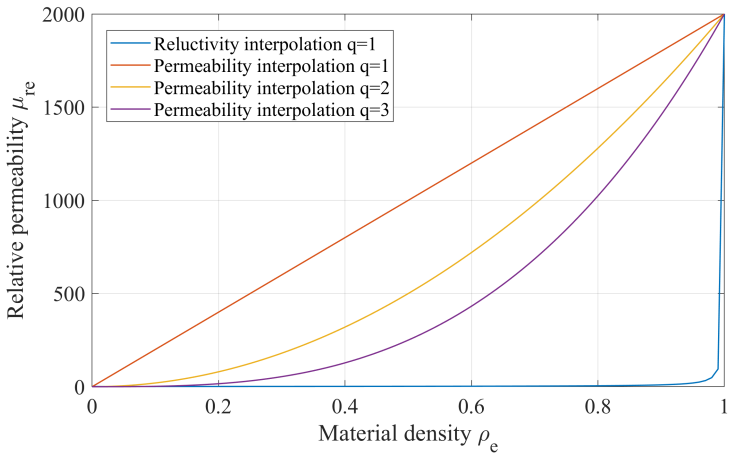

Figure 2.4: Comparison between permeability interpolation and reluctivity interpolation using the polynomial formulation.

The interpolation of ferromagnetic material with its non-linear $\mathbf{BH}$ curve, obtained with $\nu(|\mathbf{B}|)$, and the air of reluctivity ν_0 are presented in in Fig. 2.5. This is obtained with the material density variation $0 \leq \rho \leq 1$.

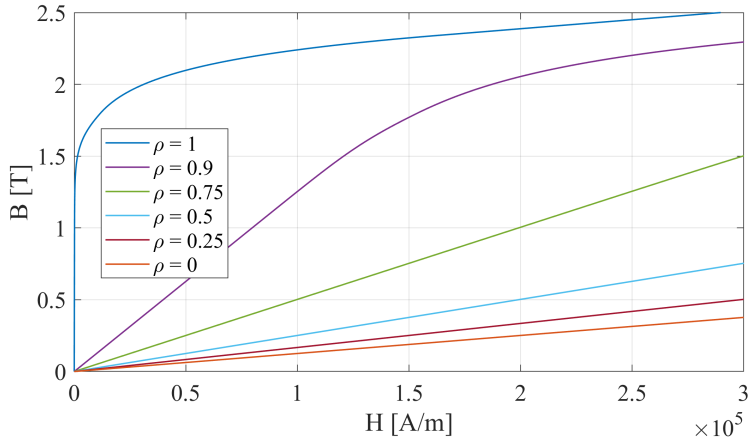

Figure 2.5: Non-linear $\mathbf{BH}$ curve obtained for different material densities ρ.

2.3.2 Magnetostatic problem formulation

Electromagnetic phenomena are described by Maxwell's equations, which were first introduced in 1892 by James Clerk Maxwell Maxwell (1892). The finite element model is derived from the set of equations that reads:

$$\begin{cases} \nabla \times \mathbf{E} = -\frac{\partial \mathbf{B}}{\partial t} \\ \nabla \times \mathbf{H} = \mathbf{J} + \frac{\partial \mathbf{D}}{\partial t} \\ \nabla \cdot \mathbf{D} = \rho_v \\ \nabla \cdot \mathbf{B} = 0 \end{cases} \tag{2.6}$$

with $\mathbf{E}$ ($\mathrm{V/m}$) the electric field intensity, $\mathbf{H}$ ($\mathrm{A/m}$) the magnetic field intensity, $\mathbf{D}$ ($\mathrm{C/m^2}$) the electric flux density, $\mathbf{B}$ (T) the magnetic flux density, $\mathbf{J}$ ($\mathrm{A/m^2}$) the current density source and ρ_v ($\mathrm{C/m^3}$) the electric charge density. The above system of equations presented in (2.6) is the general form, which may or may not be a function of time. In this thesis, all the problems treated are two-dimensional magnetostatic. The magnetostatic model is thus obtained by neglecting the time derivatives in Maxwell's equations. The Maxwell's equations can then be resumed as:

$$\begin{aligned} \nabla \times \mathbf{H} &= \mathbf{J} \\ \nabla \cdot \mathbf{B} &= 0 \end{aligned} \tag{2.7}$$

To solve the magnetic problem, the system of equations (2.7) must be completed with a material constitutive law. This constitutive relation describes the macroscope properties of the materials at any point in the field region and link the vector fields $\mathbf{H}$ and $\mathbf{B}$. The constitutive law can be written as:

$$\mathbf{H} = \nu(|\mathbf{B}|)\mathbf{B} \tag{2.8}$$

With ν the non-linear magnetic reluctivity of the material, depending on $\mathbf{B}$ value. In this dissertation, all material properties are assumed to be homogeneous and isotropic.

The magnetic vector potential $\mathbf{A}$ can be introduced:

$$\mathbf{B} = \nabla \times \mathbf{A} \tag{2.9}$$

This relation automatically satisfies $\nabla \cdot \mathbf{B} = 0$, because the divergence of curl is always zero and it results in $\nabla \cdot (\nabla \times \mathbf{A}) = 0$.

Substituting equations (2.8) and (2.9) into the field problem (2.7), we can write:

$$\nabla \times \mathbf{H} = \nabla \times (\nu(|\mathbf{B}|)\mathbf{B}) = \nabla \times (\nu(|\nabla \times \mathbf{A}|)\nabla \times \mathbf{A}) = \mathbf{J} \tag{2.10}$$

In the context of two-dimensional analysis, using cartesian coordinates, the current density vector $\mathbf{J}$ has only one component perpendicular to the plane (x, y), which is just the z-axis component. Therefore, the magnetic vector potential $\mathbf{A}$ has only a z-axis component, i.e., the vector $\mathbf{A}$ is parallel to vector $\mathbf{J}$. Then these vectors, assuming the invariance along the z-axis, can be simplified to only z-components J_z and A_z. Equation (2.10) becomes:

$$\frac{\partial}{\partial x}\left(\nu(|\nabla A_z|)\frac{\partial A_z}{\partial x}\right) + \frac{\partial}{\partial y}\left(\nu(|\nabla A_z|)\frac{\partial A_z}{\partial y}\right) = -J_z \tag{2.11}$$

The magnetic flux density vector $\mathbf{B}$ has components only on the plane (x, y), then (2.9) could be written as:

$$\mathbf{B} = \left(\frac{\partial A_z}{\partial y}, -\frac{\partial A_z}{\partial x}, 0\right) = (B_x, B_y, 0) \tag{2.12}$$

The magnetic flux density vector $\mathbf{B}$ will be used, combined with the material interpolation, for the computation of the different quantities of interest presented in the following sections.

2.3.3 Finite element formulation

The finite element method is utilized to solve the two-dimensional magnetostatic problem described by the partial differential equation in (2.11). The problem domain is discretized into a set of finite elements, which can be triangular, quadrilateral, or other shapes. In this thesis, first-order triangular elements are chosen. The physical quantities are calculated in each of these elements and the solution can be found at nodes using an interpolation function. The initial step is to establish the weak formulation of the governing equation (2.11). This is obtained by multiplying the equation with a test function ψ, integrating over the entire problem domain Ω and applying Green's theorem:

$$\int_\Omega \nu(|\nabla A_z|)(\nabla A_z \cdot \nabla \psi)\ \mathrm{d}\Omega = \int_\Omega J_z \psi\ \mathrm{d}\Omega, \quad \forall \psi \tag{2.13}$$

The solution for the magnetic vector potential $\mathbf{A}$ is approximated by a set of functions, called shape or basis functions, that are defined over each element.

$$A_z = \sum_i N_i A_{z,i} \tag{2.14}$$

where N_i are the designed shape functions at the node i^{th} and $A_{z,i}$ are the nodal values of A_z. Substituting this approximation into the weak form (2.13), we obtain:

$$\sum_i A_{z,i} \int_\Omega \nu \left(|\nabla A_z|\right) \left(\nabla N_i \cdot \nabla N_j\right) \, \mathrm{d}\Omega = \int_\Omega J_z N_j \, \mathrm{d}\Omega \quad \forall j \tag{2.15}$$

This can be written in the matrix form as:

$$K(\mathbf{A})\mathbf{A} = \mathbf{J} \tag{2.16}$$

where K is the magnetic stiffness matrix, obtained for each mesh element as:

$$K_{ij} = \int_\Omega \nu \left(|\nabla A_z|\right) \left(\nabla N_i \cdot \nabla N_j\right) \, \mathrm{d}\Omega \tag{2.17}$$

For the following sections, $\mathbf{A}$ is the vector of nodal values $A_{z,i}$ associated at each element, and $\mathbf{J}$ is the vector of the current density contributions:

$$J_j = \int_\Omega J_z N_j \, \mathrm{d}\Omega \tag{2.18}$$

Appropriate boundary conditions must be applied to solve the system of equations obtained from (2.13). Common boundary conditions for magnetostatic problems include Dirichlet's boundary conditions (specifying the value of A_z on the boundary) and Neumann's boundary conditions (specifying the derivative of A_z on the boundary).

In this study, on the outer boundary of the simulation domain the magnetic vector potential is set to zero, enforcing a zero normal component of the magnetic flux density $\mathbf{B}$.

Here, the known vector potential is associated with the outer surface of an electrical machine.

Once the system matrix equation (2.16) has been assembled, and the boundary conditions correctly applied, the problem is then solved and the magnetic vector potential A_z at each node can be obtained. For the non-linear formulations, the problem is solved using the Newton-Raphson method. The method is based on the linearization of the non-linear equations around the current solution estimation, the detailed formulation can be found in Bargallo (2006).

2.3.4 Quantity of interest

Once the structure is designed and the boundary conditions are assigned, the magnetic properties of the materials are assigned together with the field sources. The solution of the problem (2.16) consists of the knowledge of the magnetic vector potential A_z in all the domain. The magnetic flux density and magnetic field strength vectors are derived from A_z. From that, different quantities can be computed. In this thesis, we will focus only on some quantities, detailed below.

2.3.4.1 Magnetic energy

The magnetic energy is an important parameter integrated in the objective functions in various optimization problems addressed in this thesis, as it will be presented in the next chapter.

In the linear model, the ferromagnetic material is assumed to have a constant relative magnetic reluctivity ν_r, and the magnetic energy computation is straightforward. However, a non-linear model is required when saturation effects cannot be ignored, such as in electrical machine design. For these cases, we use Marrocco's interpolation, as previously described in (2.4), to account for the saturation in the energy computation accurately. Here, both linear and non-linear energy computations will be presented.

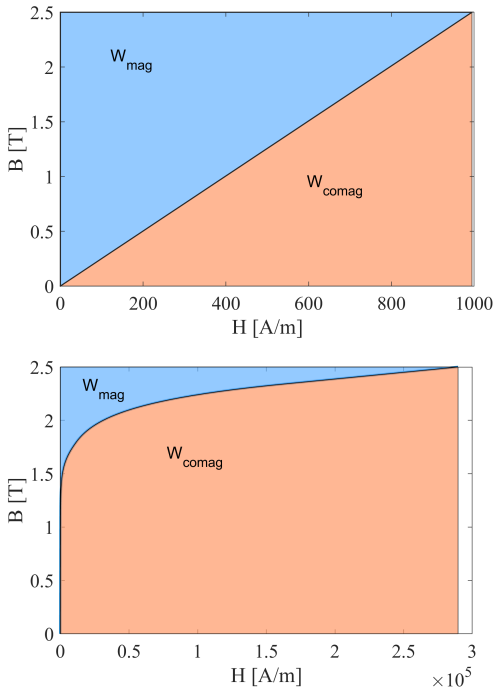

Figure 2.6: Magnetic energy and co-energy derived from the linear and non-linear $\mathbf{BH}$ curve.

In the linear case, the magnetic energy W_{mag} in a given region Ω of the space, considering the material relation $\mathbf{H} = \nu\mathbf{B}$, where $\nu = \nu_r\nu_0$, can be defined as:

$$W_{\text{mag}} = \frac{1}{2}\int_{\Omega} \nu\mathbf{B}^2 \, \mathrm{d}V \tag{2.19}$$

Let us consider the discretization of the domain Ω into finite elements, and denote the number of mesh elements as N_{elem}. The integral over the domain Ω can be approximated by the sum of integrals over each element e as:

$$W_{\text{mag}} = \frac{1}{2}\sum_{e=1}^{N_{\text{elem}}} \int_{\Omega_e} \nu_e\mathbf{B}_e^2 \, \mathrm{d}V \tag{2.20}$$

Within each element, the magnetic flux density $\mathbf{B}_e$ can be approximated in terms of the nodal values $\mathbf{A}$. With (2.12), (2.14) and (2.17) the magnetic energy can be expressed by the discrete vector potential $\mathbf{A_e}$ in an element e, and the associated elementary magnetic stiffness matrix K_e, leading to:

$$W_{\text{mag}} = \frac{1}{2}\sum_{e=1}^{N_{\text{elem}}} \mathbf{A}_e^T K_e \mathbf{A}_e \; = \frac{1}{2}\mathbf{A}^T K \mathbf{A} \tag{2.21}$$

Considering the proposed material interpolation (2.5), the material properties depend on the density ρ, thus the linear energy formulation can be written for a single element as:

$$w_{\text{mag,e}}(\rho_e) = \frac{1}{2}\left(\nu_0 + (\nu - \nu_0)\rho_e^q\right)\mathbf{B}_e^2 = \frac{1}{2}\left(\nu_0 + (\nu - \nu_0)\rho_e^q\right)\mathbf{A}_e^T K_e^{(0)} \mathbf{A}_e \tag{2.22}$$

where $K_e^{(0)}$ is the element magnetic stiffness matrix with the material properties of the air.

With saturation, the ferromagnetic non-linearity must be considered, and the magnetic energy can be obtained as a difference between the $\mathbf{BH}$ product and the magnetic co-energy, computed from the non-linear $\mathbf{BH}$ curve, according to their relationship shown in Fig. 2.6.

$$\mathbf{B}\cdot\mathbf{H} = W_{\text{mag}} + W_{\text{comag}} \tag{2.23}$$

Considering a single finite element, the magnetic energy density can be written:

$$w_{\text{mag,e}} = \int_0^{\mathbf{B}_e} \nu_e(|b|)b \; \mathrm{d}b \tag{2.24}$$

Considering the material interpolation, the elementary magnetic energy could be written as:

$$w_{\mathsf{mag},e}(\rho_e) = \int_0^{\mathbf{B}_e} \left(\nu_0 + (\nu(|b|) - \nu_0)\rho_e^q\right) b \, \mathrm{d}b \tag{2.25}$$

Thus, the magnetic energy can be divided into two distinct contributions: one related to the air and the other to the ferromagnetic material. It can be rewritten as follows:

$$\begin{aligned} w_{\mathsf{mag},e}(\rho_e) &= \nu_0(1-\rho_e^q)\frac{\mathbf{B}_e^2}{2}\Delta_e + \int_0^{\mathbf{B}_e} \nu(|b|)\rho_e^q b \, \mathrm{d}b\Delta_e \\ &= \nu_0(1-\rho_e^q)\frac{\mathbf{B}_e^2}{2}\Delta_e + \rho_e^q w_{\mathsf{mag},e}(|\mathbf{B}_e|) \end{aligned} \tag{2.26}$$

The expression is analogous to interpolating between the energies of air and ferromagnetic material. Factoring out the terms that depend on the density, the equation is similar to interpolating between the two energies $\left(W_{\mathsf{mag},e}(\rho_e) = W_0 + \left(W_{\mathsf{mag},e}(|\mathbf{B}_e|) - W_0\right)\rho_e^q\right)$. Using equation (2.23), the expression (2.26) becomes:

$$\begin{aligned} w_{\mathsf{mag},e}(\rho_e) &= \nu_0(1-\rho_e^q)\frac{\mathbf{B}_e^2}{2}\Delta_e + \rho_e^q\left(\mathbf{B}_e\cdot\mathbf{H}_e - w_{\mathsf{comag},e}(|\mathbf{B}_e|)\right)\Delta_e \\ &= \nu_0(1-\rho_e^q)\frac{\mathbf{B}_e^2}{2}\Delta_e + \rho_e^q\left(\nu(|\mathbf{B}_e|)\mathbf{B}_e^2 - w_{\mathsf{comag},e}(|\mathbf{B}_e|)\right)\Delta_e \\ &= \left[\nu_0 + (2\nu(|\mathbf{B}_e|) - \nu_0)\,\rho_e^q\right]\frac{\mathbf{B}_e^2}{2}\Delta_e - \rho_e^q w_{\mathsf{comag},e}(|\mathbf{B}_e|)\Delta_e \end{aligned} \tag{2.27}$$

This formulation enables the energy calculation with intermediate material properties, thereby facilitating gradient computations.

2.3.4.2 Electromagnetic torque

Different calculation approaches have been developed to obtain the torque produced by a rotating electrical machine, such as Maxwell stress tensor, virtual work principle, Arkkio's method, etc. The Maxwell stress tensor is the most used in literature and software implementation. It is the simplest in terms of computation but it is very sensitive to error and mesh size, as the stress tensor is integrated on a line in the air-gap. An in-depth comparative analysis of accuracy between the above-mentioned methods can be found in Sadowski et al. (1992).

In this thesis, the electromagnetic torque is computed using the Arkkio's method Arkkio (1987). This method is based on the Maxwell stress tensor but differs in that the tensor is not integrated along a line, but rather over a band (surface) inside the air-gap. Additionally, it mitigates the dependency on the quality of the mesh. The electromagnetic torque is then computed with:

$$T = \frac{L_{\mathsf{stk}}\nu_0}{r_s - r_r}\int_{r_r}^{r_s}\int_0^{2\pi} r B_r B_\theta \, dr \, d\theta \tag{2.28}$$

where r_s and r_r are the internal and external radii of the torque integration band, θ the angular position, and L_{stk} the axial length of the machine. B_r and B_θ are the normal and tangential components of the $\mathbf{B}$-field vector. Using the x and y components of the magnetic density, the two quantities can be written as:

$$\begin{cases} B_r = \cos(\theta)B_x + \sin(\theta)B_y \\ B_\theta = -\sin(\theta)B_x + \cos(\theta)B_y \end{cases} \tag{2.29}$$

With the normal and tangential flux density components expressed in terms of the x and y components, and using the formulation of the magnetic flux density in (2.12), we get the following formula:

$$T = \frac{L_{\text{stk}}\nu_0}{r_s - r_r} \int_{\Omega_{\text{band}}} \frac{1}{2\sqrt{x^2+y^2}} \begin{pmatrix} -2xyB_x & (x^2-y^2)B_x \\ (x^2-y^2)B_y & 2xyB_y \end{pmatrix} \cdot \begin{pmatrix} B_x \\ B_y \end{pmatrix} dxdy \tag{2.30}$$

To simplify the formulation, we define:

$$Q = \frac{1}{2\sqrt{x^2+y^2}} \begin{pmatrix} -2xy & x^2-y^2 \\ x^2-y^2 & 2xy \end{pmatrix} \tag{2.31}$$

Using this, we get:

$$T = \frac{L_{\text{stk}}\nu_0}{r_s - r_r} \int_{\Omega_{\text{band}}} B \cdot QB \, dx \, dy \tag{2.32}$$

This can be expressed considering each mesh element e of the air-gap by the following:

$$T = \frac{L_{\text{stk}}\nu_0}{r_s - r_r} \sum_e B_e \cdot Q_e B_e \, \Delta_e \tag{2.33}$$

where Δ_e is the surface of the mesh element e. With this matrix notation in the expression of the electromagnetic torque, its gradient computation will be simplified.

This formulation is carried out for one rotor position, giving the instantaneous torque value. The movement of the rotor needs to be considered for the computation of the electromagnetic torque curve and to get the torque ripple. To account for motion in electrical machines, various techniques have been developed that consider motion in an intermediate zone between moving and fixed parts Davat et al. (1985).

In this thesis, the movement of the rotor is taken into consideration using the moving-band technique. This method subdivides the air-gap into meshes, allowing rotation to occur via a layer

of finite elements placed in the air-gap. This layer can occupy the entire air-gap region or a part of it. At each step of the rotor displacement, the elements of the moving band are distorted. When the distortion becomes too large, the air-gap is re-meshed. The detailed formulation is presented in Bastos and Sadowski (2003). In order to mitigate the impact of the known issues associated with the moving band method, it was ensured that the torque is computed outside the re-meshed elements and that at least one element of air is present on the stator side. The different layers of the air-gap are presented in Fig. 2.7 with the description of each layer.

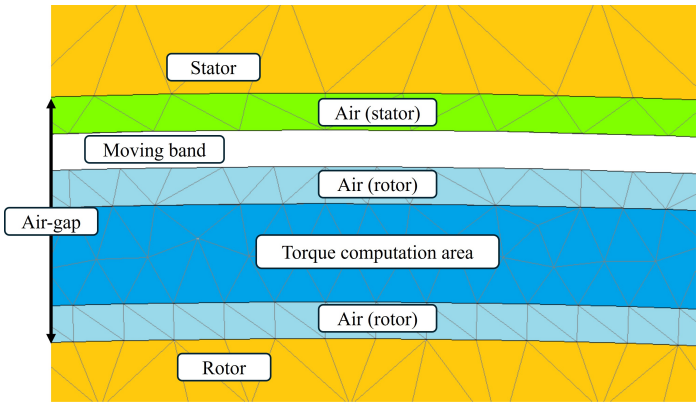

Figure 2.7: Air-gap subdivision.

2.3.4.3 Magnetic forces for vibration analysis

Calculating forces is essential for analyzing electrical machines, as these devices rely on the interaction between the stator and rotor to generate motion or rotation. Electromagnetic forces in electrical machines can be classified into three categories: Maxwell forces, Laplace (or Lorentz) forces and equivalent magnetostrictive forces. Among these, Maxwell forces play a dominant role in generating electromagnetic noise. For this reason, this thesis will consider only Maxwell forces, focusing on the component that causes vibro-acoustic effects on the stator for further vibration computation.

In electrical machine analysis, two types of forces can be considered: global forces and local forces. Global forces refer to the overall resultant forces acting on an object, while local forces are characterized by their distribution at specific points across the object's surface.

If the interest is placed only on the operational total force on the rigid moving object, a global force calculation may be enough. However, for noise and vibration analysis of electric machines, it is necessary to calculate the distribution of local forces.

Among the various existing methods for local magnetic force computation, such as the Maxwell stress tensor method, energy method, Lorentz force method, and virtual work method, the virtual work method was chosen for this thesis, based on its advantages Bossavit (2011).

The principle of the virtual work method is based on the energy balance between two different positions, supposing a virtual movement along the direction where the force is computed. In electromagnetic problems, the magnetic force is expressed as the partial derivative of magnetic energy (at constant flux) with respect to the coordinates x along which the force component must be computed:

$$F_x = -\frac{\partial W_{\text{mag}}}{\partial x} \tag{2.34}$$

Considering that the force computation is done at fixed constant flux, this means fixed magnetic flux density $\mathbf{B}$ and therefore fixed magnetic vector potential $\mathbf{A}$. The local magnetic force at a node k in x direction is then written using vector potential $\mathbf{A}$:

$$F_k = -\frac{1}{2}\nu \mathbf{A}^T \frac{\partial K}{\partial x}\mathbf{A} \tag{2.35}$$

It should be noted that the local force is non-zero mainly at the nodes located at the interface of air and ferromagnetic material. To compute the derivative of the magnetic stiffness matrix, the local Jacobian derivative method, formulated by Coulomb Coulomb and Meunier (1984), is employed. The force formulation (2.35) is not developed further since these forces will be utilized only for vibration analysis. The implementation of this method within the Matlab code can be found in Besbes (1995), and Bastos and Sadowski (2003).

In electrical machines, electromagnetic forces are usually the main source of vibrations and noise emitted beyond the stator mechanical structure. To calculate these vibrations, it is necessary to determine the distribution of electromagnetic forces on the stator for each time step. For the vibrational analysis described in Chapter 4, the time and space mapping of electromagnetic forces will be obtained by combining the virtual work method with the moving band.

2.4 Mechanical model

In this section, the mechanical model employed in this thesis is presented. To ensure clarity and precision, some initial hypotheses and assumptions are utilised. The first hypothesis concerns the

material, which is assumed to be elastic, linear, homogeneous, and isotropic. This means that the material deforms proportionally to the applied load, and that its mechanical properties are the same in all directions and throughout the material. The second hypothesis concerns the problem, assumed to be quasi-static and quasi-isothermal so without dynamic effects and temperature changing and assuming small displacements so the deformation of the structure does not change the geometry of the problem.
Based on these hypotheses, the mechanical model is developed and solved in 2D with plane stress consideration using the finite element method Saiac (2009).

2.4.1 Material properties

The considered linear material properties are characterized by the Young's modulus (E_Y) and the Poisson's coefficient (ν_p). The mechanical parameters of the considered electrical steel are derived from average values that are representative of commercial M270-35A steels, and presented in Table 2.2.

Table 2.2: Material mechanical parameters

Parameter	Value	Unit
Material density (γ)	7800	kg/m^3
Young's modulus (E_{steel})	200	GPa
Poisson's ratio (ν_p)	0.3	
Yield strength (S_y)	400	MPa

The yield strength is utilized in the post processing and compared with the Von Mises stress of the solution. This comparison, done considering a safety factor, indicates if the stress is lower than the critical yield value of the material.

Considering the polynomial interpolation formulation of equation (2.3), the Young's modulus is made to be dependent on the element relative density using the SIMP approach:

$$E_Y(\rho) = E_{min} + (E_{steel} - E_{min})\rho^q \tag{2.36}$$

where E_{steel} is the Young's modulus of the considered material, as presented in Table 2.2, and E_{min} is a minimum value, here equal to 10^{-3} [GPa], corresponding to the air properties. Associating a Young' modulus value to the air does not really make sense, but this is done to ensure numerical stability during the finite element problem resolution. The penalization factor here is set to $q = 3$ and the resulting interpolation curve is reported in Fig. 2.8.

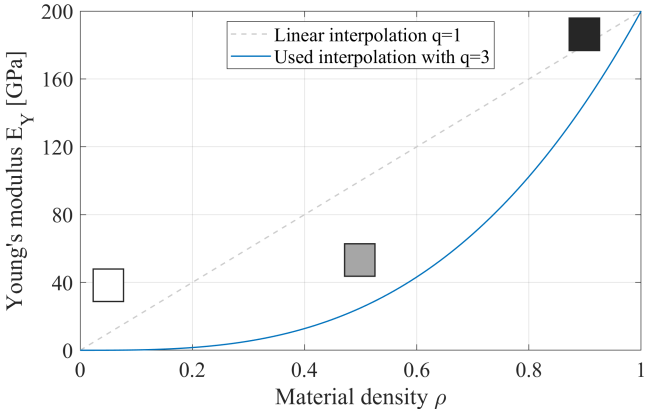

Figure 2.8: Young's modulus interpolation.

2.4.2 Mechanical problem formulation

The two-dimensional mechanical problem is formulated under the assumption of plane stress. This assumption is applicable to thin structures, such as plates or thin-walled components, where the thickness is small compared to the other dimensions. Stator and rotor laminations are typically made of thin sheets of ferromagnetic material stacked together. Therefore, for these thin sections, the plane stress assumption is valid.

The concepts of a two-dimensional state of stress and strain and the stress-strain relationships for plane stress are essential to introduce the static mechanical analysis and to fully understand the finite element analysis.

As introduced, let's assume small displacements, for which the equations of linear elasticity are valid. In 2D, the unknown of the problem is the plane displacement vector $\mathbf{u}$:

$$\mathbf{u} = \begin{pmatrix} u(x,y) \\ v(x,y) \end{pmatrix} \tag{2.37}$$

The strain vector ϵ is given by its components as a function of the first derivatives of the displacements according to:

$$\epsilon = \begin{pmatrix} \epsilon_{xx} \\ \epsilon_{yy} \\ 2\epsilon_{xy} \end{pmatrix} = \begin{pmatrix} \frac{\partial u}{\partial x} \\ \frac{\partial v}{\partial y} \\ \frac{\partial u}{\partial y} + \frac{\partial v}{\partial x} \end{pmatrix} \tag{2.38}$$

ϵ_{xx} and ϵ_{yy} are the axial strains along the x, y directions and $2\epsilon_{xy}$ is the shear strain. With

displacements known at all points within the element, the "strains" at any point can be determined. It can be written as a relationship that in matrix notation is written as:

$$\epsilon = B_u \mathbf{u} \tag{2.39}$$

With B_u the matrix of differential operators:

$$B_u = \begin{pmatrix} \frac{\partial}{\partial x} & 0 \\ 0 & \frac{\partial}{\partial y} \\ \frac{\partial}{\partial y} & \frac{\partial}{\partial x} \end{pmatrix} \tag{2.40}$$

The equations of elasticity are expressed by a linear relationship between stress and strain, which in a plane stress problem can be written as:

$$\sigma = \mathbf{D}\epsilon \tag{2.41}$$

where σ is the stress vector written as:

$$\sigma = \begin{pmatrix} \sigma_{xx} \\ \sigma_{yy} \\ \sigma_{xy} \end{pmatrix} \tag{2.42}$$

with σ_{xx} and σ_{yy} being the axial stresses, and σ_{xy} the shear stress. $\mathbf{D}$ is the Hooke matrix, also called the constitutive matrix, which is expressed as a function of the Young's modulus E_Y and the Poisson's coefficient ν_p. For plane stress conditions we have:

$$\mathbf{D} = \frac{E_Y}{1-\nu_p^2} \begin{pmatrix} 1 & \nu_p & 0 \\ \nu_p & 1 & 0 \\ 0 & 0 & \frac{1-\nu_p}{2} \end{pmatrix} \tag{2.43}$$

The Young's modulus and Poisson's ratio are determined by the material's characteristics. Consequently, the constitutive matrix is influenced by the material interpolation employed in topology optimization, as it incorporates the necessary material properties.
Finally, the equilibrium equations between forces and stresses can be written as:

$$\begin{cases} \frac{\partial}{\partial x}\sigma_{xx} + \frac{\partial}{\partial y}\sigma_{xy} + f_x = 0 \\ \frac{\partial}{\partial x}\sigma_{xy} + \frac{\partial}{\partial y}\sigma_{yy} + f_y = 0 \end{cases} \tag{2.44}$$

where f_x and f_y are the two components of the surface forces in the x and y directions.

Using the matrix of differential operators B_u and the relations $\epsilon = B_u\mathbf{u}$ and $\sigma = \mathbf{D}\epsilon$, we obtain a system of second-order partial differential equations, written in the form:

$$\mathbf{B}_u^T\mathbf{D}\mathbf{B}_u\mathbf{u} + \mathbf{f} = 0 \tag{2.45}$$

where the unknown of the system is the displacements vector $\mathbf{u}$.

2.4.3 Finite element formulation

The finite element method is employed in a manner analogous to that of the magnetostatic model in order to solve the two-dimensional mechanical problem described by the partial differential equilibrium equation. The mesh of the mechanical problem will be identical to the one used for the magnetostatic problem. The weak formulation of the governing equation is then derived by multiplying the equilibrium equation (2.45) with a test function η and integrating by parts with the Green formulation over the entire problem domain Ω:

$$\int_\Omega (\mathbf{D}\mathbf{B}_u\mathbf{u}) \cdot \mathbf{B}_u\eta \, d\Omega = -\int_\Omega \mathbf{f} \cdot \eta \, d\Omega \quad \forall\eta \tag{2.46}$$

We assume the domain Ω is meshed with $P1$ Lagrange space triangular finite elements. We write the approximate problem in the sub-space V_h^2. Let $\mathbf{I}$ be the set of indices of the mesh nodes corresponding to an unknown value of the solution $\mathbf{u}$, and $\mathbf{N_I}$ the cardinality of $\mathbf{I}$. The space V_h^2 will have dimension $2N_\mathbf{I}$. We choose the set of vectors as the basis of V_h^2, according to the Lagrange technique:

$$\begin{pmatrix} w_i \\ 0 \end{pmatrix}, \begin{pmatrix} 0 \\ w_i \end{pmatrix} \quad \text{for } i = 1, \ldots, N_\mathbf{I} \tag{2.47}$$

where w_i are the Lagrange basis scalar functions of the space of continuous affine functions on triangles. The components of the approximate solution will be written as linear combinations of these basis functions w_i as:

$$\begin{aligned} u_h(x,y) &= \sum_{j\in\mathbf{I}} u_j w_j(x,y) \\ v_h(x,y) &= \sum_{j\in\mathbf{I}} v_j w_j(x,y) \end{aligned} \tag{2.48}$$

By using the matrix form of the variational formulation, we obtain from 2.46 the following

linear system:

$$\begin{cases} \displaystyle\int_\Omega \sum_{j\in\mathbf{I}} \mathbf{DB_u} \begin{pmatrix} w_j & 0 \\ 0 & w_j \end{pmatrix} \begin{pmatrix} u_j \\ v_j \end{pmatrix} \cdot \mathbf{B_u} \begin{pmatrix} w_i \\ 0 \end{pmatrix} d\Omega = \int_\Omega \begin{pmatrix} f_x \\ f_y \end{pmatrix} \begin{pmatrix} w_i \\ 0 \end{pmatrix} d\Omega \quad \forall i \in \mathbf{I} \\ \displaystyle\int_\Omega \sum_{j\in\mathbf{I}} \mathbf{DB_u} \begin{pmatrix} w_j & 0 \\ 0 & w_j \end{pmatrix} \begin{pmatrix} u_j \\ v_j \end{pmatrix} \cdot \mathbf{B_u} \begin{pmatrix} 0 \\ w_i \end{pmatrix} d\Omega = \int_\Omega \begin{pmatrix} f_x \\ f_y \end{pmatrix} \begin{pmatrix} 0 \\ w_i \end{pmatrix} d\Omega \quad \forall i \in \mathbf{I} \end{cases} \tag{2.49}$$

Since there are 2 unknowns u_i and v_i per node of the mesh, the above system is a linear system of $2N_\mathbf{I}$ equations with $2N_\mathbf{I}$ unknowns. After assembling on a mesh element, the system (2.49) may be rewritten for one mesh element e in the commonly recognized form:

$$K_s^e \, \mathbf{u}^e = \mathbf{f}^e \tag{2.50}$$

where:

$$K_s^e = \int_{\Omega_e} (B_u^e)^T D^e B_u^e \, d\Omega_e \tag{2.51}$$

In this form K_s^e is the element structural stiffness matrix indicating the resistance of the element to deformation when subjected to loading, u^e is the vector of element nodal displacements, f^e is the vector generalized forces, and Ω_e is the volume of element e. Once each element stiffness matrix has been calculated, a standard assembly process is used to generate the global structural stiffness matrix K_s and the force vector F, which are then used to solve for the global displacements vector u of a given structure:

$$K_s u = F \tag{2.52}$$

The final step is the insertion of prescribed boundary conditions into the final assembled matrix. It can be shown that at this stage, the global stiffness matrix K_s is a singular matrix because its determinant is equal to zero. To remove this singularity problem, we must invoke certain boundary conditions (constraints or supports) so that the structure remains in place instead of moving as a rigid body. For this case, Dirichlet boundary conditions specify the displacements at certain points or regions of the structure. These conditions define how parts of the structure are fixed or how they move. We find fixed boundary (zero displacement) when certain nodes or regions are constrained to prevent the rigid body motion and the displacement in all directions

is set to zero, or prescribed displacements when specific displacements are assigned to certain points or regions.

In this thesis, we use only the fixed boundary condition due to the specific requirements of analyzing electrical machines. We apply this condition for the interface $\partial\Omega$ between the rotor and the shaft, as shown in Fig. 2.9, imposing fixed boundaries to ensure that the rotor remains rigid to the shaft. This approach maintains the structural integrity and stability needed for accurate analysis.

$$\mathbf{u} = 0 \quad \text{on } \partial\Omega \tag{2.53}$$

When the boundary conditions are inserted, the unknown global structure nodal displacements are determined by solving the system of algebraic equations given by (2.52).

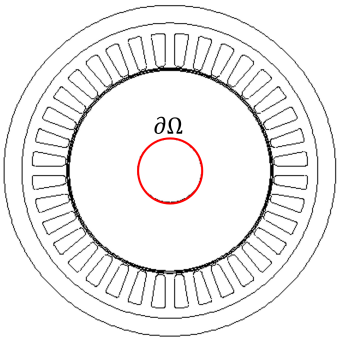

Figure 2.9: Interface $\partial\Omega$ (in red) between the rotor and the shaft.

The system (2.52) is related to a mechanical static problem, in Chapter 4 the topology optimization problem will be applied to a dynamic problem and so the equilibrium equation will change, for a dynamic system it will be written as follows:

$$M_s\ddot{\mathbf{u}} + C_s\dot{\mathbf{u}} + K_s\mathbf{u} = \mathbf{F}(t) \tag{2.54}$$

where M_s is the mass matrix and C_s is the damping matrix. The vectors $\ddot{\mathbf{u}}$ and $\dot{\mathbf{u}}$ represent respectively the vector of nodal accelerations and the vector of nodal velocities. The force vector $\mathbf{F}(t)$ represents the impact of external forces applied to the structure, which can vary with time t. The comprehensive explanation will be provided in the corresponding chapter.

2.4.4 Quantity of interest

In addition to the magnetic analysis, a mechanical study is conducted to ensure the structural integrity of the electric machine during operation. Since this thesis primary focus is to optimize

the rotor topology, the discussion will mainly revolve around the stress sources affecting this rotating component.

To ensure structural integrity, it is crucial to consider a structural design criterion, which helps to limit the displacement of rotor steel parts, especially for the material regions near the airgap. Furthermore, it is essential to consider the local resistance of the material to guarantee the risk of failure of the mechanical bridges in the flux barrier regions. The quantities that will be considered to overcome these necessities are the compliance and Von Mises stress.

2.4.4.1 Compliance

Compliance is an energy quantity representing a global design criterion, defined as the inverse of the stiffness. Minimizing the compliance of a structure means maximizing its stiffness, thereby improving its rigidity. This quantity has been used since the first work on topology optimization, applied to trusses, cantilever, and bridges Bendsøe and Kikuchi (1988).

The choice of the compliance as a quantity in topology optimization is motivated by the fact that its sensitivity is easy to calculate, being self-adjoined, i.e. it does not require an adjoint variable to compute its derivative. The compliance C is formulated as follows:

$$C = F^T \mathbf{u} = \mathbf{u}^T K_s \mathbf{u} \tag{2.55}$$

The stiffness matrix contains the material properties, and it will be affected by the material interpolation. Additionally, the load vector, which includes the forces generated by the rotation of the rotor (centrifugal forces), is linearly dependent on the material density. These forces are then design-dependent and, for a single element, are expressed in terms of the design variable ρ_e as follows:

$$F_e = \rho_e m_e r_e \omega^2 \tag{2.56}$$

where m_e is the mass of the element, r_e is the distance between the center of the element and the origin of the global coordinate, and ω the rotational speed. Considering the material interpolation (2.36), the compliance is rewritten as:

$$C(\rho) = \mathbf{u}^T K_s(\rho) \mathbf{u} = \mathbf{u}^T (E_{min} + (E_{steel} - E_{min})\rho^q) K^{(0)} \mathbf{u} \tag{2.57}$$

where $K^{(0)}$ is the base stiffness matrix constructed without considering the Young's modulus

material properties. When the compliance is minimized, the displacement $\mathbf{u}$ is reduced, and the stiffness of the structure is globally maximized. Of course, the maximum stiffness will be achieved when the structure is thus a solid structure with a maximum volume and, consequently, if only this quantity is employed in the optimization problem, it is necessary to consider a constraint on the maximum volume. For an electrical machine rotor, minimizing the displacement of the region near the air-gap is important but not sufficient to guarantee the mechanical integrity.

2.4.4.2 Von Mises stress

The Von Mises stress is a scalar that measures the intensity of the entire stress state and is used to predict the failure of a structure subjected to static loading. The Von Mises stress σ_{vm}, considering the plane strain condition, is given in terms of the three principal stresses $(\sigma_{xx}, \sigma_{yy}, \sigma_{xy})$ by:

$$\sigma_{vm} = \sqrt{\frac{1}{2}\left[(\sigma_{xx} - \sigma_{yy})^2 + (\sigma_{yy} - \sigma_{zz})^2 + (\sigma_{zz} - \sigma_{xx})^2\right] + 3\sigma_{xy}^2} \tag{2.58}$$

with $\sigma_{zz} = \nu_p(\sigma_{xx} + \sigma_{yy})$. If the Von Mises stress reaches the yield strength of the material, the structure is at risk of failure and rupture. Therefore, ensuring that the Von Mises stress stays below the yield strength is crucial in structural design to prevent failure. This criterion is written as follows:

$$\sigma_{vm} \leq S_y \tag{2.59}$$

Considering the design of a rotor, this criterion must be respected to assure the structural integrity during high-speed operation. Additionally, the rotor can be designed with a safety factor to prevent the mechanical failure. Introducing the safety factor SF, typically set in the range between 2 and 3 Babetto et al. (2018a), the criterion to be respected is expressed as:

$$\sigma_{vm} \leq \frac{S_y}{SF} \tag{2.60}$$

2.5 Sensitivity analysis

When addressing topology optimization through a gradient-based method, it is essential to compute the gradient of the objective function and constraints with respect to the design variables. Let us consider a generic function denoted as $f_i(\chi(\rho), \rho)$ that could represent any objective or constraint. A simple approach to compute the gradient of this function is to evaluate the derivatives through finite differences. This technique consists in taking a small perturbation $\delta\rho$ in

each design variable in turn and recalculate the function value. Adopting the centered difference scheme, the design sensitivities are computed as:

$$\frac{df_i}{d\rho} \approx \frac{f_i(\rho + \delta\rho) - f_i(\rho - \delta\rho)}{2\delta\rho} \tag{2.61}$$

To compute the function value for each perturbation, the physical problem should be solved by a finite element analysis. Considering a total of N design variables, the central difference strategy requires $2N$ finite element analysis. Therefore, due to the large number of design variables (equivalent to the number of elements) in topology optimization problems, the cost of calculating the sensitivity by the finite difference is too expensive and time consuming. Further, the results are dependent by the perturbation size, sometimes leading to errors in gradient computation. For these reasons, the finite difference method is not considered for computing sensitivities in topology optimization.

The analytical differentiation is an alternative to finite differences, allowing a reduced computational complexity. For the generic function dependent on both explicit variable ρ and state (implicit) variables χ , the sensitivities can be calculated based on their respective terms as:

$$\frac{df_i}{d\rho} = \left.\frac{\partial f_i}{\partial \rho}\right|_{\chi=\text{const}} + \left(\left.\frac{\partial f_i}{\partial \chi}\right|_{\rho=\text{const}}\right)^T \frac{\partial \chi}{\partial \rho} \tag{2.62}$$

The first two terms are generally easy to compute, but evaluating the third term is much more involving. To compute the third term, two different approaches can be used: the direct method or the adjoint method. The direct method requires as many system solutions as the number of design variables, similarly to finite difference. Therefore, it is still not suitable for topology optimization problems. The adjoint method, on the other hand, involves solving an auxiliary (adjoint) problem to obtain the gradients of the function with respect to the design variables Cea (1986). When compared to the direct method, the adjoint method requires a number of evaluations equal to the number of functions, not the number of design variables. The adjoint method also calculates the sensitivities without explicitly calculating the sensitivity of the state variables.

Considering a non linear partial differential equation $K(\rho, \chi)\chi = j$ as example, we can introduce the residual r of the problem defined as:

$$r(\rho, \chi) = K(\rho, \chi)\chi - j = 0 \tag{2.63}$$

And differentiating the residual equation as:

$$\frac{dr}{d\rho} = \frac{\partial r}{\partial \rho} + \frac{\partial r}{\partial \chi}\frac{\partial \chi}{\partial \rho} = 0 \tag{2.64}$$

We can rewrite the sensitivity as follows:

$$\frac{df_i}{d\rho} = \frac{\partial f_i}{\partial \rho} - \frac{\partial f_i}{\partial \chi}\left(\frac{\partial r}{\partial \chi}\right)^{-1}\frac{\partial r}{\partial \rho} \tag{2.65}$$

Which can be rearranged inverting the order of multiplications of the terms above as:

$$\frac{df_i}{d\rho} = \frac{\partial f_i}{\partial \rho} - \left[\frac{\partial f_i}{\partial \chi}\left(\frac{\partial r}{\partial \chi}\right)^{-1}\right]\frac{\partial r}{\partial \rho} \tag{2.66}$$

The term in brackets is also called the adjoint term, which leads to the following simplified formulation:

$$\frac{df_i}{d\rho} = \frac{\partial f_i}{\partial \rho} + \lambda^T\frac{\partial r}{\partial \rho} \tag{2.67}$$

where λ is the vector of adjoint state variables, obtained through an initial solution of the adjoint problem:

$$\frac{\partial r}{\partial \chi}\lambda = -\frac{\partial f_i}{\partial \chi} \tag{2.68}$$

The adjoint problem is not sensitive to the optimization problem dimension as it does not depend on design variables ρ. Thus, the adjoint variable method is an efficient approach for gradient computation in optimization problems with a large number of design variables like in topology optimization. In this thesis, the finite-difference method will only be used to verify the analytical sensitivity obtained through the AVM.

2.6 Regularization techniques

In topology optimization, several numerical issues may arise during the optimization process Sigmund and Petersson (1998). Regularization techniques are employed to control the optimization process to overcome the appearance of these issues.

One of these issues is the appearance of checkerboard patterns, a numerical artifact obtained when solid and void regions appear in adjacent meshes in a grid-like pattern. This problem is common in mechanical topology optimization. It is particularly prevalent when using first-

order finite elements, as the finite element method tends to overestimate the stiffness of the checkerboard pattern in such cases. As a result, the checkerboard pattern is artificially preferred by the optimizer. This numerical artifact makes interpretation of the final design difficult and, therefore, must be prevented. In Fig. 2.10 is shown an example of these patterns, appeared in the mechanical bridges of a rotor of a synchronous reluctance motor.

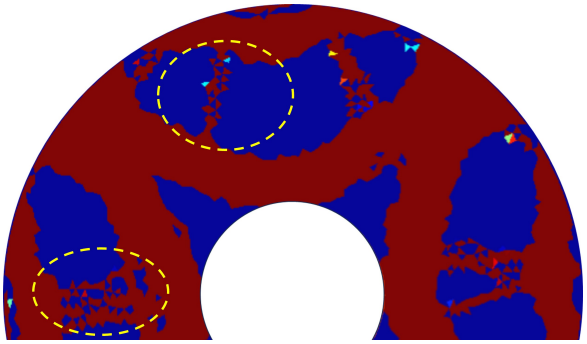

Figure 2.10: Example of checkerboard pattern encircled in yellow.

Another issue is mesh dependency, where using different mesh sizes for the same problem yields different results. Moreover, this issue remains mainly a difficulty in mechanical topology optimization despite a minor presence in magnetic ones. For example, a coarse mesh may result in one topology, whereas a finer mesh may yield a different outcome. This problem is less prevalent in electromagnetic problems due to the necessity for compactness of the material distribution for an efficient magnetic flux flow, as shown in Fig. 2.11.

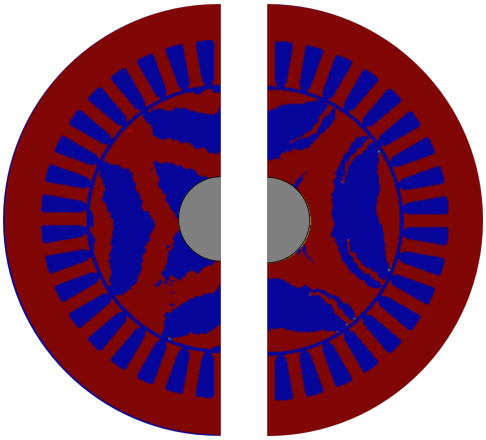

Figure 2.11: Example of mesh dependency, geometry obtained with coarse mesh (left) and fine mesh (right).

Furthermore, the appearance of intermediate densities in the final design is another potential issue. Topology optimization should ideally give a result with a clear distinction between solid (material) and void (air) regions. However, because the design variables are continuous, the optimization process may produce elements with intermediate densities, making a design

difficult to produce or impractical if the objective is to achieve a solution comprising exclusively solid or void densities.

For the first two problems, filtering techniques are usually adopted. For intermediate density, post-processing at the end of the optimization, consisting of a density projection, is done.

Filtering methods for topology optimization are divided into two categories, density based and sensitivity based. Density filters are directly applied to the design variables, while sensitivity filters are applied to the computed sensitivity.

2.6.1 Density based filter

Density filtering was introduced in Bruns and Tortorelli (2001) and consists in replacing the density variable in each element of the domain by a weighted average of the elements in a mesh-independent neighborhood of this element. This filter can be applied to the design variable at each iteration or periodically, as done in Cherriere et al. (2024). As shown in the flowchart in Fig. 2.1, this filter is applied after the optimization algorithm to the updated solution. The filtered density results as:

$$\widetilde{\rho}_e = \frac{\sum_{i \in N_e} w(x_i)\rho_i \Delta_i}{\sum_{i \in N_e} w(x_i)\Delta_i} \tag{2.69}$$

where $\tilde{\rho}_e$ represents the filtered element density, N_e represents the set of neighboring elements around element e, Δ_i is the volume or area of the neighboring element i, and $w(x_i)$ is the weighting function that depends on the distance between the center of the neighboring element i and the target element e. The neighborhood of an element is defined in general as the elements whose centers are in a pre-defined distance, defined by the filter radius value, from the center of this element. The weighting function is defined as follows:

$$w(x_i) = 1 - \frac{\|x_i - x_e\|}{r_{\text{filter}}} \tag{2.70}$$

where r_{filter} is the filter radius which defines the neighborhood size, and $\|x_i - x_e\|$ represents the distance between the center of the ith element and the center of the eth element. The weights are typically chosen to decrease with distance from the center of the element being filtered, ensuring that closer neighbors have a more significant influence on the filtered density. Therefore, the size of the set N_e depends on the filter radius as follows:

$$N_e = \{i \text{ such that } \|x_i - x_e\| \leq r_{\text{filter}}\} \tag{2.71}$$

The radius is normally chosen based on the mesh size, if the radius is smaller than the mesh size the filter will not have any effect.

2.6.2 Sensitivity based filter

Sensitivity filter was first introduced in Sigmund (1994). The idea is the redefinition of the sensitivity of an element as a weighted average of the sensitivities in a mesh-independent neighborhood of this element, like the density filter. This method has proven to work well in practice and is the most utilized, making solutions mesh-independent and accessible from checkerboards. As it modifies the gradient, this filter is applied after the sensitivity computation. The original form of the sensitivity filter was formulated considering homogeneous meshes discretization. However, the meshes are normally non-regular and a modification need to be done, considering the element surface or volume. The filtered sensitivity of the generic function f with respect a mesh element e is written as:

$$\frac{\widetilde{\partial f}}{\partial \rho_e} = \frac{\sum_{i \in N_e} w(x_i)\rho_i \left(\frac{\partial f}{\partial \rho_i}\right)/\Delta_i}{\rho_e/\Delta_e \sum_{i \in N_e} w(x_i)} \tag{2.72}$$

The weighting factor and the neighborhood domain are computed by (2.70) and (2.71) as showed for the density filter.

Intuitively, it would have made more sense to multiply by the element volumes (big elements, big weight and small elements, small weight), however, the motivation for dividing by the volumes is partly based on numerical experiments and partly based on energy considerations Sigmund (2007). By dividing by the element volume, the term inside the summation in the numerator can be interpreted as an averaged strain energy density (energy per unit volume).

The filter radius can vary dynamically throughout the optimization and typically it should have a low value at the final iterations to allow the algorithm to reach black and white solution.

The gradients computed in this thesis are directly dependent by the mesh size through the mesh surface of each element, resulting in a discrete gradient distribution. The filter effects are showed in the Fig 2.12, where the computed gradient results in a discrete distribution and with the sensitivity filter (considering in this example a radius $r_{\text{filter}} = 1.5$mm) a resulting continuous distribution is obtained without the mesh size dependence.

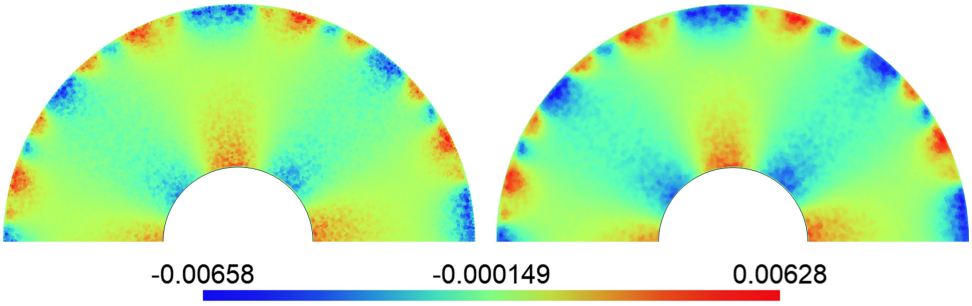

Figure 2.12: Example of sensitivity filter applied to a gradient distribution: before the filter (left) and after (right).

2.6.3 Heaviside projection

The solution of the density-based topology optimization is often considered conceptual, with sometimes intermediate materials or rough surfaces. These intermediate densities are usually caused by the usage of density filters or contrasting multi-physics in the optimization problem, such as magneto-mechanical problems. On the other hand, the rough surfaces are related to the finite element mesh dimension, and the general idea is to use the density filter to smooth out the shape of the obtained solution. However, as mentioned, it leads to the appearance of intermediate densities.

To convert the optimized design into a manufacturable design, which consists of either full or void material densities, a post-processing step is essential. This step often involves a density projection, also known as Heaviside projection, applied to the optimal density distribution ρ. This projection uses a smoothed Heaviside function to refine the initial design into a more feasible and manufacturable one. The projected density $\widetilde{\rho}$ results as:

$$\widetilde{\rho} = \frac{\tanh(\beta\eta) + \tanh(\beta(\rho - \eta))}{\tanh(\beta\eta) + \tanh(\beta(1 - \eta))} \tag{2.73}$$

where β is an intensity factor of the projection and η is the cut-off threshold value.

By employing these regularization techniques, topology optimization problems can be solved more effectively, resulting in designs that are both optimized for performance, have a physical sense and practical for manufacturing.

2.7 Optimization algorithms

The topology optimization problem formulated with the density-based method is typically solved using gradient-based iterative algorithms. These algorithms are particularly suitable for

differential and continuous objective functions and constraints. Derivative-based optimization solvers are known for their efficiency and ability to handle complex problems with a large number of design variables. These algorithms also require low computational time, compared to those without the gradient as genetic algorithms. The two algorithms that will be utilized in this thesis are the Generalized Optimality Criteria (GOC) and the Method of Moving Asymptotes (MMA).

2.7.1 Generalized Optimality Criteria GOC

The generalized optimality criteria was introduced in Kim et al. (2021) and this algorithm is developed from the so-called Optimality Criteria (OC). The OC algorithm gained significant attention since the publication of the 99-lines Matlab code for topology optimization Sigmund (2001). For simple problems, the OC algorithm is an excellent choice due to its ease of use, speed, and cost efficiency. It is particularly useful for compliance problems with a volume fraction constraint, as it consistently aims to add material to achieve high stiffness. However, the OC method is insufficient when dealing with more complex problems. To address this limitation, the generalized version of the OC algorithm extends its capabilities to handle multiple inequality constraints and allows for a general objective function.

After the computation of the sensitivity of the objective and constraints functions, the design variables ρ are updated by the following formulation:

$$\rho^{k+1} = \rho^k \cdot D^{\frac{1}{\beta^k c_0}} \tag{2.74}$$

where ρ^k and ρ^{k+1} represent the material density at the current iteration and the updated one respectively, D is the scale factor that contains the gradients information, β and c_0 are two acceleration parameters that can be modified based on the exigence. The two acceleration parameters are suggested in Kim et al. (2021) to be $\beta = 1$ and $c_0 = 2$, these values will also be used in this thesis. Considering the general objective function f and multiple constraints g_i, the scale factor is calculated based on the sign of the sensitivities. The numerator consists of all terms with negative sensitivities, while the denominator has all terms with positive sensitivities. Consequently, for a given design variable ρ_e, the scale factor in an element e is computed as follows:

$$D_e = \frac{-\left\langle \frac{\partial f}{\partial \rho_e} \right\rangle_- + \sum_{i=1}^{N_C} \mu_i \left\langle \frac{\partial g_i}{\partial \rho_e} \right\rangle_-}{\left\langle \frac{\partial f}{\partial \rho_e} \right\rangle_+ + \sum_{i=1}^{N_C} \mu_i \left\langle \frac{\partial g_i}{\partial \rho_e} \right\rangle_+} \tag{2.75}$$

where N_C is the number of constraints and μ_i the Lagrange multiplier corresponding to constraint g_i. The negative and positive sensitivities are taken as $\langle a \rangle_- = \min(0, a)$ and $\langle a \rangle_+ = \max(0, a)$. If the numerator and/or the denominator are zero, the scale factor needs to be modified and limited so that it stays close to one. The Lagrange multipliers are iteratively determined during the optimization process to find a value that satisfies the constraints. The method for updating the Lagrange multipliers can vary depending on the specific algorithm and problem formulation. In this thesis, a bisection method is employed.

With the updated design variable, it is needed to limit the variations imposing the lower and upper bounds (ρ_{min} and 1). To ensure approximation quality, it is also suggested to limit the range of variable changes with a move limit m, so that:

$$\max\left(\rho_{\mathsf{min}}, \rho^k - m\right) \leq \rho^{(k+1)} \leq \min\left(1, \rho^k + m\right) \tag{2.76}$$

Smaller move limits results in finer adjustments and can improve the convergence to local minima but may slow down the optimization process. On the other hand, larger move limits allow for faster convergence but can lead to larger variations and potentially less accurate results. Choosing an appropriate move limit often involves empirical testing and may depend on the specific problem characteristics, constraints, and desired precision of the solution.

2.7.2 Method of Moving Asymptotes MMA

The Method of Moving Asymptotes, also known as MMA, was developed by K. Svanberg in 1987 Svanberg (1987) and since then is one of the most utilized algorithms for density-based topology optimization problems. Svanberg also proposed a better convergent version of MMA in 2002, the globally convergent version (GCMMA) Svanberg (2002). However, GCMMA needs relatively higher calculation time compared to MMA.

The MMA algorithm is based on a convex approximation of the optimization problem, and it can fit single or multiple constraints. At each iteration a subproblem is created, in which the functions (objective and constraint functions) are replaced by an approximated convex function. The approximated functions are computed on basis of the gradient information at the current iteration point, and on the moving asymptotes parameters which are updated in each iteration based on information from previous iteration point. These asymptotes permit to control the subproblem and may both stabilize and speed up the convergence of the general process. The

subproblem generated by MMA is then solved using "primal-dual-interior-point method" to find the optimal point that will be used in next iteration.

Given an iteration point k with the design variable $\rho^{(k)}$ with $\rho \in \mathbb{R}^n$, an approximation of a given function f_i will be written as following. Firstly, the lower asymptotes L_j and the upper asymptotes U_j are computed, and based on these parameters the approximation function $\tilde{f}_i^{(k)}$ of the given function f_i is defined as:

$$\tilde{f}_i^{(k)}(\rho) = r_i^{(k)} + \sum_{j=1}^{n} \left(\frac{p_{ij}^{(k)}}{U_j^{(k)} - \rho_j} + \frac{q_{ij}^{(k)}}{\rho_j - L_j^{(k)}} \right) \tag{2.77}$$

where

$$r_i^{(k)} = f_i\left(\rho^{(k)}\right) - \sum_{j=1}^{n} \left(\frac{p_{ij}^{(k)}}{U_j^{(k)} - \rho_j^{(k)}} + \frac{q_{ij}^{(k)}}{\rho_j^{(k)} - L_j^{(k)}} \right) \tag{2.78}$$

$$p_{ij}^{(k)} = \begin{cases} \left(U_j^{(k)} - \rho_j\right)^2 \frac{\partial f_i}{\partial \rho_j}, & \text{if } \frac{\partial f_i}{\partial \rho_j} > 0 \\ 0, & \text{if } \frac{\partial f_i}{\partial \rho_j} \leq 0 \end{cases} \tag{2.79}$$

$$q_{ij}^{(k)} = \begin{cases} 0, & \text{if } \frac{\partial f_i}{\partial \rho_j} \geq 0 \\ -\left(\rho_j - L_j^{(k)}\right)^2 \frac{\partial f_i}{\partial \rho_j}, & \text{if } \frac{\partial f_i}{\partial \rho_j} < 0 \end{cases} \tag{2.80}$$

It is worth noting that $\tilde{f}_i^{(k)}$ is a convex function and a first order approximation of f_i. The parameters $U_j^{(k)}$ and $L_j^{(k)}$ act like asymptotes in (2.77) and control, loosely speaking, the range for which $\tilde{f}_i^{(k)}$ approximates f_i reasonably. The tighter we choose $U_j^{(k)}$ and $L_j^{(k)}$ around $\rho^{(k)}$, the more curvature is given to the approximating function, and the more conservative the approximation of the original problem becomes.

For more information on the MMA and GCMMA algorithm and details on how to choose the asymptotes and the others algorithms parameters, the already cited references should be looked at, but also Svanberg's notes Svanberg (2014) on MMA and GCMMA are useful.

2.8 Test case example

In this subsection, a numerical example is presented to show the application of the topology optimization methodology previously described. To simplify the example, a linear magnetostatic case will be analyzed.

2.8.1 Optimization problem

The optimization is here applied to the design of an inductance. The simple geometry is given in Fig. 2.13 where the yellow central leg is the optimization domain, the thickness is taken of unitary value of 1 mm. The optimization problem is formulated to maximize the magnetic energy of the inductance under a volume constraint.The problem is written as follows:

$$\begin{aligned} \min_{\rho \in \Omega} \quad & -W_{mag}(\mathbf{A}, \rho) \\ \text{s.t.} \quad & \frac{1}{V_{tot}} \sum_{e=1}^{N_{\text{elem}}} \rho_e \Delta_e \leq V_{\%} \\ & \rho_{\text{min}} \leq \rho_e \leq 1 \end{aligned} \tag{2.81}$$

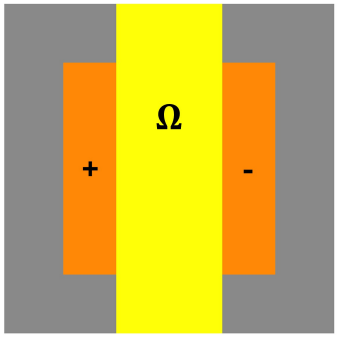

Figure 2.13: Inductance geometry with optimization domain Ω in yellow.

The material interpolation law used for the optimization domain is the polynomial law presented in (2.5), with the penalty parameter $q = 1$. The optimization problem is solved with different values of the volume constraint $V_{\%}$, varying from 10% to 90%. The used optimization algorithm is the GOC algorithm and no filter is applied during the optimization. N_{elem} is the number of mesh elements that compose the optimization domain Ω, here equal to 8745 elements. The coil is supplied with a current density $\mathbf{J}$ set as 5 A/mm^2. Considering the optimization domain filled with a material density $\rho = 1$ the resulting magnetic energy is $W_{mag} = 1.7 \cdot 10^{-4} J$. The GOC algorithm needs the gradient of the objective function to update the density variable distribution, we will then compute it with the adjoint variable method previously presented.

2.8.2 Gradient computation

The objective function in (2.81) is the magnetic energy of the system, this quantity is computed with (2.19). The energy of the optimization domain, considering the material interpolation, is then computed by (2.22). With these equations and the adjoint variable method introduced in section 2.5 we can derive the gradient of the objective function:

$$\frac{dW_{mag}}{d\rho} = \frac{\partial W_{mag}}{\partial \rho}\bigg|_{\mathbf{A}=\text{const}} + \left(\frac{\partial W_{mag}}{\partial \mathbf{A}}\bigg|_{\rho=\text{const}}\right)^T \frac{\partial \mathbf{A}}{\partial \rho} \tag{2.82}$$

As previously mentioned, the first two terms are easy to compute but evaluating the third term is not trivial. To compute the third term we then use the adjoint method. We define the residual r of the linear magnetic finite element problem $K(\rho)\mathbf{A} = \mathbf{J}$ as:

$$r = K(\rho)\mathbf{A} - \mathbf{J} = 0 \tag{2.83}$$

Using this residual notation and the adjoint state variable λ, we can rewrite sensitivity of the magnetic energy as follows:

$$\frac{dW_{mag}}{d\rho} = \frac{\partial W_{mag}}{\partial \rho} + \lambda^T \frac{\partial r}{\partial \rho} \tag{2.84}$$

where λ is first obtained from:

$$\frac{\partial r}{\partial \mathbf{A}}\lambda = -\frac{\partial W_{mag}}{\partial \mathbf{A}} \tag{2.85}$$

We can now compute each of the four terms:

$$\frac{\partial W_{mag}}{\partial \rho} = \frac{1}{2}\left(\nu - \nu_0\right)\mathbf{A}^T K^{(0)}\mathbf{A} \tag{2.86}$$

$$\frac{\partial W_{mag}}{\partial \mathbf{A}} = \mathbf{A}^T K \tag{2.87}$$

$$\left(\frac{\partial r}{\partial \mathbf{A}}\right) = K \tag{2.88}$$

$$\frac{\partial r}{\partial \rho} = \frac{\partial K}{\partial \rho}\mathbf{A} = \left(\nu - \nu_0\right) K^{(0)}\mathbf{A} \tag{2.89}$$

Finally, we can obtain the adjoint variable, resulting:

$$\lambda = -\mathbf{A}^T K K^{-1} = -\mathbf{A}^T \tag{2.90}$$

Note that, in this linear problem case, the adjoint term can be directly obtained from the state variable. This type of problem is referred to as self-adjoint.

The gradient of the magnetic energy can now be obtained:

$$\begin{aligned}\frac{dW_{mag}}{d\rho} &= \frac{\partial W_{mag}}{\partial \rho} + \lambda^T \frac{\partial r}{\partial \rho} = \frac{1}{2}\left(\nu - \nu_0\right)\mathbf{A}^T K^{(0)}\mathbf{A} - \left(\nu - \nu_0\right)\mathbf{A}^T K^{(0)}\mathbf{A} = \\ &= -\frac{1}{2}\left(\nu - \nu_0\right)\mathbf{A}^T K^{(0)}\mathbf{A}\end{aligned} \tag{2.91}$$

2.8.3 Results

By varying the volume constraint $V_{\%}$, different geometries are obtained and a Pareto front can be achieved as show in Fig. 2.14. The ferromagnetic material is distributed around the coil to canalize the field lines. For low volume constraints we obtain a disconnected structure.

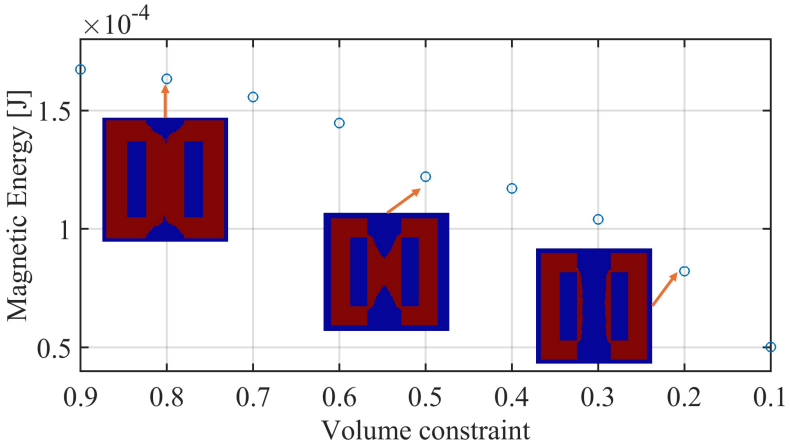

Figure 2.14: Pareto front for the inductance design.

2.9 Chapter conclusions

In this chapter we presented the methodology for topology optimization problems, focusing on magnetostatic and mechanical formulations. The various components of the computational process were explained and discussed, giving the basis for the application of TO to a general optimization problem.

The detailed descriptions of the magnetostatic and mechanical models began with the material properties and the interpolation technique. For both models, the density-based SIMP method was employed. This method facilitates the interpolation of physical properties via the material densities ρ. Various interpolations exist, and those applied in this work have been outlined. Following this, the problem formulation was developed, including the governing equations and their implementation using the finite element method. The chapter then described the specific quantities of interest used in this thesis: magnetic energy and electromagnetic torque for the magnetostatic model, and compliance and Von Mises stress for the mechanical model. These quantities are essential for evaluating the performance of the designs.

Then we dig into sensitivity analysis, a fundamental step when addressing TO through gradient-based method. Due to the high number of design variables, the adjoint variable method was adopted.

Regularization techniques were additionally discussed, important for ensuring the stability and reliability of the optimization process.

Additionally, we dig into the sensitivity analysis and regularization techniques. We covered various filters and a projection method that help to solve different problems in TO. We also reviewed optimization algorithms, including the Generalized Optimality Criteria (GOC) and the Method of Moving Asymptotes (MMA).

A practical test case was finally presented, illustrating the methodology application to a simple magnetostatic problem. In this example, a reluctance was optimized to maximize the magnetic energy under different volume constraints. The sensitivity analysis of the magnetic energy by applying the AVM was detailed. The optimization results were then presented, showing the variation of the material distribution within the volume constraints.

In summary, the chapter provided a thorough description of the tools and techniques necessary for implementing topology optimization in a rigorous and reproducible manner. The methodologies presented here form the basis for the more complex applications that will be explored in the subsequent chapters. Specifically, in the next chapter, this framework will be applied to the optimization of an electrical machine.

Chapter 3

Magneto-mechanical topology optimization

This chapter presents a detailed study of magneto-mechanical topology optimization (TO) applied to the rotor design of a synchronous reluctance motor. Firstly, magnetic TO is presented with two different optimization formulations with the objective of improving the magnetic performances of the motor. More specifically, this step allows the comparison between a new objective function formulated with the magnetic energy, and the more common formulation with the average torque.

After the magnetic optimization, we will extend our analysis by including mechanical considerations. The combination of electromagnetic and mechanical computation in electric machine design is a necessary approach to ensure satisfactory robustness of the rotor structure. The magneto-structural optimization is applied using two different methodologies.

The first consists in a two-step methodology approach where magnetic and mechanical optimizations are decoupled and run one after the other. This will enable the sequential refinement of the rotor design, first addressing the magnetic performance and then the mechanical integrity with structural robustness.

The second methodology is the coupled one in which magnetic and mechanical optimizations are within the same optimization process. This integrated approach allows handling the magnetic and mechanical objectives simultaneously when searching for an optimum trade-off between magnetic efficiency and mechanical strength. Coupling these optimizations, we seek a rotor design that improves the mechanical behaviour while ensuring magnetic performance.

In the final section of this chapter, we will discuss about the comparison between the results obtained with both the two-step and combined approaches.

3.1 Case study

A significant trend in the design of electrical machines is the parallel efforts in different domains toward non-rare earth machine alternatives. By eliminating the rare-earth magnets, motor cost reduction is improved, and dependence on this critical material is removed. Induction machines have had a good shot at meeting this need, but the increasing demands for high specific power and power density requirements are eliminating induction machines as viable options. Two other machine topologies that eliminate magnets on the rotor are the synchronous reluctance machine (SynRM) and the switched reluctance machine (SRM). Both machines have a rotor composed of only thin steel laminations.

The SRM, despite some advantages, has significant noise issues, high torque ripple, vibration problems, and significant complexity and costs in the motor control. SynRMs are more appealing for their higher efficiency and lower torque ripple compared to SRM, and simplicity (low cost) of control. On the other hand, the lack of the permanent magnetic field in the rotor is penalized with lower torque density, lower power factor, and higher torque ripple compared to SynRMs with permanent magnets. It was recognized that significantly improved saliency ratios can abate these disadvantages Kostko (1923). If adequately designed with a high saliency ratio, the machine's power factor, efficiency, and torque/power density are improved with levels that are competitive with permanent magnet SynRMs Ban et al. (2019). With significant research, SynRM can provide a path to obtain high-performance traction machines without rare earth content.

For the aforementioned reasons, this thesis analyzes and designs a three-phase SynRM. This type of machine was chosen due to its simplicity, widespread use across various fields, and flexibility in design, either with or without permanent magnets. Topology optimization is applied for the design of the rotor part, while the stator geometry is fixed. The main motor parameters are represented in Table 3.1. In Fig. 3.1 the relative geometry is shown with the rotor region (Ω) highlighted in yellow that represents the rotor domain where topology optimization will be applied.

Table 3.1: SynRM geometric parameters

Parameter	Unit	Value
Phases number		3
Poles number		4
Slots number		36
Stator outer diameter	mm	130
Rotor outer diameter	mm	78.75
Rotor inner diameter	mm	25
Air-gap	mm	1
Machine length	mm	100

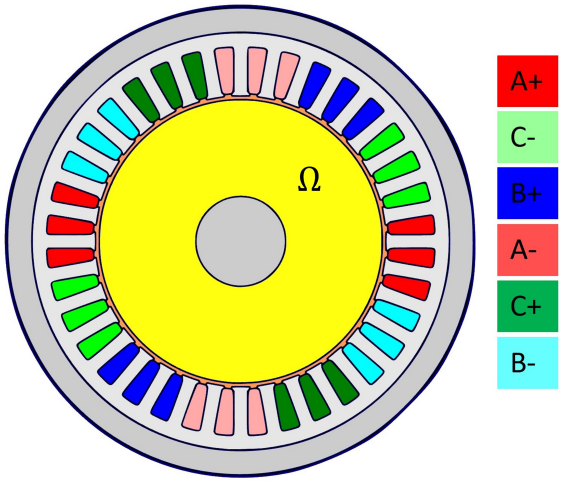

Figure 3.1: Machine geometry with the used winding distribution configuration and yellow rotor design space Ω where topology optimization is applied.

The winding distribution on the stator consists in a single-layer distributed configuration with a coil span of 9 slots and a maximum achievable winding factor k_w of $0,96$. In the context of electric motor, the torque generated is proportional to the fundamental winding factor. Therefore, a higher value of k_w is desirable as it indicates enhanced performances. The three-phase currents are purely sinusoidal for simplicity and the sources are represented by:

$$\begin{cases} J_A = J\cos\left(\theta_e + \phi\right) \\ J_B = J\cos\left(\theta_e - \frac{2\pi}{3} + \phi\right) \\ J_C = J\cos\left(\theta_e - \frac{4\pi}{3} + \phi\right), \end{cases} \tag{3.1}$$

where J is the current density amplitude and here is set as 5 A/mm^2, θ_e is the electrical angle, and ϕ is the current phase angle that represents the angular displacement between the d-axis of the stator and the d-axis of the rotor. The choice of 5 A/mm^2 is based on typical values used for machines with natural convection, ensuring a balance between thermal management and

performance Yang et al. (2017). This value also helps achieve magnetic saturation, allowing the machine to operate in nonlinear conditions.

3.2 Magnetostatic optimization

Over the past several years, there have been vigorous research activities in electromagnetic design optimization to improve the performance of electrical machines and in particularly SynRMs Chowdhury et al. (2021) Bianchi et al. (2021) Zhang et al. (2024).The primary objective of nearly all topology optimization (TO) focused on electric machines thus far has been to maximize the torque density or shape the torque profile to reduce the torque ripple. The objective function for the torque maximization in the literature is typically formulated in terms of average torque T_{avg} Lee and Jang (2021) Korman et al. (2022a), which is computed by determining its instantaneous values for different rotor positions T_θ.

$$T_{avg} = \frac{1}{N}\sum_{k=1}^{N} T_{\theta_k} \tag{3.2}$$

In principle, the "mean" torque T_{em} of a SynRM is closely linked to the saliency ratio ξ, written as:

$$\begin{aligned} T_{em} &= \frac{3}{2}p(L_d - L_q)i_d i_q \\ \xi &= L_d/L_q \end{aligned} \tag{3.3}$$

where p is the number of pole pairs, L_d, i_d and L_q, i_q are the $d-$axis and $q-$axis inductances and currents respectively. As shown, the electromagnetic torque depends on the saliency ratio and in order to improve machine performance, they must be designed with a high value, as already discussed previously. Thus, increasing the quantity $(L_d - L_q)$ is equivalent to increasing ξ.

With these considerations, we propose an alternative formulation of the magnetostatic problem. In linear conditions, the inductances of the $d-$ and $q-$axis can be calculated considering the respective axis magnetic energies and currents as:

$$L_d = \frac{2W_d}{i_d^2} \quad L_q = \frac{2W_q}{i_q^2} \tag{3.4}$$

where W_d and W_q are the $d-$axis energy and $q-$axis energy. The saliency ratio maximization $(L_d - L_q)$ could then be expressed as the maximization of the difference between the magnetic

energies of the $d-$axis and $q-$axis $(W_d - W_q)$.

It should be noted that the two equations in (3.4) are only valid under linearity conditions. In non-linear conditions these inductances are highly affected by the level of saturation in the machine core due to high amount of iron in both d- and q-axis flux paths Moghaddam (2007). The saturation effect in the q-axis is much lower than in the $d-$axis, because of the air barriers that cut the q-axis flux lines. Another effect is the cross-coupling, created by the magnetic interaction between the $d-$ and $q-$axis Pellegrino et al. (2016). This phenomenon occurs when the magnetic flux produced by the $d-$axis current saturates some zones of the machine, distorting the flux lines produced by the $q-$axis current, and vice versa.

In classical optimization methods for the magnetic design of electrical machines, it is essential to consider all these phenomena, cross-coupling effects and saturation, to accurately compute the inductance values in the $d - q$ axis. However, in topology optimization, these effects can first be considered negligible. This is because the energy formulation is used to estimate the instantaneous torque. This method uses the magnetic energy stored in the system, offering an indirect but efficacious means of improving the machine's performance without delving into the complexities of cross-coupling and saturation.

It is important to highlight that this method eliminates the need to calculate the average torque, thus reducing the computation time required to analyze different rotor positions.
Indeed, the energy difference is obtained by solving two magnetostatic finite element analysis, one with a magnetization current of the direct axis ($d-$axis) and the other with a magnetization current of the quadrature axis ($q-$axis). These axes are determined by the specific rotor geometry. In general, with topology optimization, we do not have a defined initial geometry but rather an initial material distribution that does not allow to define a $d-$ and $q-$axis. In our analysis, the $d-$ and $q-$axis were determined a priori by selecting two distinct phase angles for the currents, resulting in a 4-poles configuration.

In what follows, a magnetic-only topology optimization applied to the rotor of the SynRM is presented. The primary objective of the optimization is to maximize the average output torque. To achieve this, two different formulations will be employed, allowing for a comparative analysis of their impact on the rotor topology and its magnetic performance.

3.2.1 Formulation of the optimization problem

We define two different optimization problems, named P_T and P_W. The first problem (P_T) has the objective function expressed by the average torque maximization. This optimization

problem is the most commonly used in all topology optimization problems aimed at improving the performance of electric motors. Otherwise, the second problem (P_W) has the objective function expressed by the magnetic energy maximization between the $d-$ and $q-$axis, as previously described.

$$(P_T): \begin{cases} \min\limits_{\rho\in\Omega} & -T_{avg}(\rho) = -\dfrac{1}{N}\displaystyle\sum_{k=1}^{N} T_{\theta_k}(\rho) \\ \text{s.t.} & \dfrac{1}{V_{tot}}\displaystyle\sum_{e=1}^{N_{\text{elem}}} \rho_e \Delta_e \leq V_{\%} \\ & \rho_{\text{min}} \leq \rho_e \leq 1 \end{cases} \tag{3.5}$$

$$(P_W): \begin{cases} \min\limits_{\rho\in\Omega} & -\Delta W(\rho) = -(W_d(\rho) - W_q(\rho)) \\ \text{s.t.} & \dfrac{1}{V_{tot}}\displaystyle\sum_{e=1}^{N_{\text{elem}}} \rho_e \Delta_e \leq V_{\%} \\ & \rho_{\text{min}} \leq \rho_e \leq 1 \end{cases} \tag{3.6}$$

where N is the total number of rotor positions θ_k and T_{θ_k} is the torque at position k. The magnetic torque is calculated using the Arkkio's method, with $\theta_N = 90°$ and $N = 45$. This means an instantaneous torque computation each 2 mechanical degree. The 3-phase currents are imposed with a current phase angle $\phi = 45°$.

For the energy difference Δ_W in problem P_W, the two energies are obtained by simply taking the current phase angle ϕ, W_d with $\phi = 0°$ and W_q with $\phi = 90°$. While typically defined by rotor geometry, the absence of an initial geometry in our approach necessitates a different method for establishing the $d-q$ axes. We achieve this by a priori imposing the $d-q$ axes through two distinct current distributions on the stator. This guides the optimization process towards a material distribution that aligns flux guides with the $d-$axis and flux barriers with the $q-$axis. Fig. 3.2 illustrates the resulting flux lines with a homogeneous rotor material distribution under the influence of magnetizing currents I_d and I_q, clearly demarcating the $d-$ and $q-$ axes. This approach contrasts with the mean torque formulation, where the $d-$ and $q-$ axes emerge naturally during optimization. A volume constraint is applied to the two problems, in order to compare the two formulations with the same amount of ferromagnetic material in the rotor domain. Typically, the rotor core of a SynRM is made up of laminated iron sheets that occupy between 50% and 80% of the rotor volume, depending on the specific motor design and application. These values were obtained through research on the existing designs of SynRM machines and by analyzing the volume ratio of each design. The volume constraint $V_{\%}$ is then chosen to achieve a light motor design with a volume of 60%.

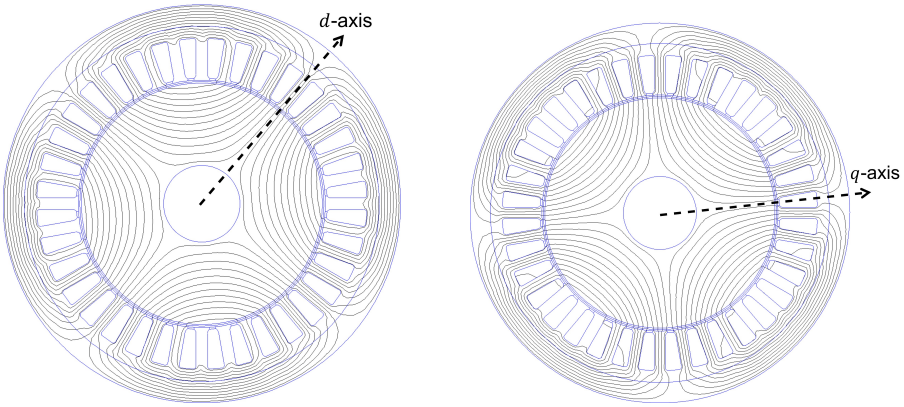

Figure 3.2: Magnetic flux lines obtained by applying the magnetization current I_d (left) and I_q (right), simulated using FEMM 4.2.

The machine in Fig. 3.1 is modeled and meshed with the open source software FEMM 4.2. The entire machine is discretized into 65480 first-order triangular elements. For the optimization domain Ω, a mesh size value of 0.5 mm is applied, limiting the maximum edge length of the triangular elements within this region. This choice results in a total number of mesh elements N_{elem} equal to 36033. The mesh distribution is presented in Fig. 3.3.

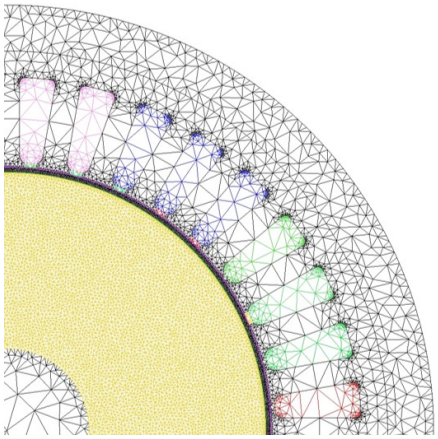

Figure 3.3: Mesh distribution of the motor used for optimization, including the yellow mesh for TO.

The optimization procedure applied to the two problems is based on the general scheme presented in Section 2.1.2. The organization of the different steps that shape the optimization procedure is represented in Fig. 3.4.

First, the material distribution is initialized. To demonstrate the importance of the initial problem setup, we will analyze the effects of different initializations. The material properties of the rotor are then derived from the interpolation function (2.5). As a reminder, density

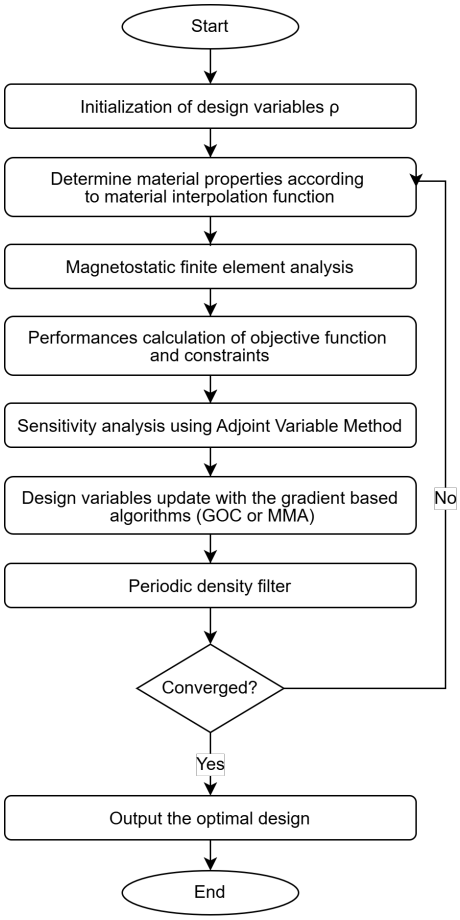

Figure 3.4: Flowchart of the magnetostatic TO procedure, with the different blocks description.

$\rho = 1$ has the magnetic properties of ferromagnetic material characterized by the non-linear reluctivity $\nu(|\mathbf{B}|)$ and $\rho = \rho_{\text{min}}$ has the air properties with void reluctivity ν_0. As we are using a continuous material distribution we utilize gradient-based algorithms, the sensitivity of the presented objective functions and constraint are necessary to correctly update the design variables. The problem is then solved with two different algorithms presented in the previous chapter, GOC and MMA. The first one is less known and we applied it here for the first time to a magnetostatic problem. The density filter (2.69) is applied periodically during the optimization process, more precisely at each 40 iterations. Considering an average element mesh size of 0.5 mm, the filter radius is set at 1.25 times the average element size. The application of this filter serves to smooth the material density distribution, thereby facilitating a broader exploration of potential solutions and preventing the algorithm from converging to non-manufacturable local optima. However, the use of the filter at each iteration can have adverse effects, such as impeding convergence and reducing the accuracy of the optimization process, which ultimately leads to sub-optimal designs Cherriere et al. (2024). Finally, the stopping criterion is defined by a maximum

number of iterations, set to 400. This choice is based on an empirical analysis combined with the periodic filtering, ensuring sufficient convergence of the optimization process while maintaining a reasonable computational cost. Using the variation of the objective function as a convergence criterion is often too sensitive, prematurely stopping the algorithm before the geometry reaches a stable design. In all cases, convergence is considered reached when the relative increase in average torque remains below 0.1 %. A post-processing phase could also be considered, where a Heaviside projection will be applied in order to obtain a final geometry composed of only full or void materials.

3.2.2 Sensitivity analysis for magnetostatic problem

This section presents the methodology for computing the gradients of the two objective functions introduced for the magnetostatic problem: average torque and energy difference. Due to the large number of control variables, we will employ the adjoint variable method (AVM) to derive these gradients with respect to the design variable ρ. We will then outline the step-by-step procedures and mathematical formulations used to obtain these gradients.

3.2.2.1 Mean torque sensitivity formulation

The derivative of the instantaneous torque expression (2.33) in regard to the state variable $\mathbf{A}$ and the design variables ρ are needed to compute the gradient, as:

$$\frac{dT}{d\rho} = \underbrace{\frac{\partial T}{\partial \rho}\bigg|_{\mathbf{A}=\text{const}}}_{=0} + \left(\frac{\partial T}{\partial \mathbf{A}}\bigg|_{\rho=\text{const}}\right)^T \frac{\partial \mathbf{A}}{\partial \rho} \tag{3.7}$$

As the torque is computed in the defined band in the air-gap, there is no explicit dependence of the material density and consequently the first term of the gradient is equal to zero. Defining the adjoint variable λ such that:

$$\frac{\partial r}{\partial \mathbf{A}}\lambda = -\frac{\partial T}{\partial \mathbf{A}} \tag{3.8}$$

The equation (3.7) results:

$$\frac{dT}{d\rho} = \lambda^T \frac{\partial r}{\partial \rho} \tag{3.9}$$

The first term for the adjoint computation, derived from the expression (2.32)

$$\frac{\partial T}{\partial \mathbf{A}} = \frac{L_{\text{stk}}\nu_0}{r_s - r_r} 2 \sum_e \frac{\partial B_e}{\partial \mathbf{A}} \cdot Q_e B_e \, \Delta_e \tag{3.10}$$

From the relation between the magnetic flux density $\mathbf{B}$ and the vector potential $\mathbf{A}$ in the 2D finite element formulation, the derivative $\frac{\partial B_e}{\partial \mathbf{A}}$ can be written as:

$$\frac{\partial \mathbf{B}_e}{\partial \mathbf{A_i}} = \nabla N_i \tag{3.11}$$

It is important to consider that as we are in a non-linear case the residual is:

$$r = K(\rho, \mathbf{A})\mathbf{A} - \mathbf{J} = 0 \tag{3.12}$$

Thus the derivative of the residual will change respect to the linear case, we have:

$$\frac{\partial r}{\partial \mathbf{A}} = K + K' \tag{3.13}$$

where the matrix K' expresses the non-linear effects, and is given by:

$$K' = \frac{\partial K}{\partial \mathbf{A}}\mathbf{A} \tag{3.14}$$

The term $\frac{\partial r}{\partial \rho}$ is the same as in the linear case, described in (2.89). The gradient of the instantaneous torque can be now computed. Here we are maximizing the mean torque, obtained through the instantaneous torque values calculated at N different angular rotor positions θ. Thus, the derivative of the torque with respect to the design variable is expressed as follows:

$$\frac{dT}{d\rho} = \frac{1}{N}\sum_{k=1}^{N}\frac{dT_{\theta_k}}{d\rho} \tag{3.15}$$

3.2.2.2 Energy difference sensitivity formulation

The procedure for the gradient computation of the magnetic energy is very similar to what we already presented in the test case example in section 2.8. Here we will do only two FE analysis and for the gradient we will need to compute the derivative of the two energies in the d- and q-axis. Starting from the energy expression of equation (2.27) and developing for one single energy we obtain:

$$\frac{\partial W_{\mathsf{mag},e}}{\partial \rho} = \left[\left(2\nu(|\mathbf{B}_e|) - \nu_0\right)\frac{\mathbf{B}_e^2}{2} - \mathsf{w}_{\mathsf{comag},e}(|\mathbf{B}_e|)\right]\Delta_e \tag{3.16}$$

The second derivative is obtained through the chain rule:

$$\frac{\partial W_{\mathsf{mag},e}}{\partial \mathbf{A}} = \left(\frac{\partial W_{\mathsf{mag},e}}{\partial \mathbf{B}_e}\right)^T \frac{\partial \mathbf{B}_e}{\partial \mathbf{A}} \tag{3.17}$$

Where:

$$\frac{\partial W_{\text{mag},e}}{\partial \mathbf{B}_e} = \nu_e(|\mathbf{B}_e|)\mathbf{B}_e \tag{3.18}$$

The validity of sensitivity computation for the average torque and energy difference has been verified comparing its results with the sensitivity obtained using the finite difference method. This comparison has been performed with an homogeneous and a random material distribution over the optimization domain. We then selected random mesh elements for the comparison. As a result, the relative difference between AVM and finite differences is lower than $1 \cdot 10^{-5}$ for each selected mesh element. This confirms the validity of the AVM formulation.

3.2.3 Magnetostatic optimization results

Before presenting the results, we want to discuss about the necessity of a density filter. The magnetostatic problem in topology optimization is not much affected by numerical issues, such as checkerboard patterns, that need the use of filters. Using a filter at each iteration greatly govern the course of the optimization process and it is advisable not to over-use it as already discussed before. However, it is important to avoid the creation of some artifacts, as shown in Fig. 3.5. For this reason, we decided to use a periodic density filter. In addition, the use of the filter helps the convergence toward geometries with fluid and regular shapes, where it is not the case without the use of filters as showed in Lee and Jang (2021).

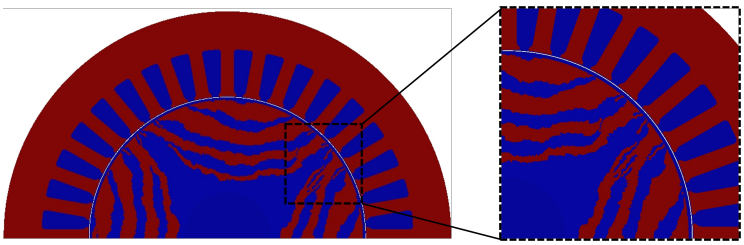

Figure 3.5: Geometry obtained without a density filter presenting rough surfaces and undesirable artifacts.

The optimization problems are initialized with different material distributions in order to explore different possible solutions, as gradient-based algorithms are sensitive to the initialization points and this strongly influences the optimal solution. For TO we can find in literature different ways to initialize the problem, for example an homogeneous material distribution Okamoto et al. (2018)-Korman et al. (2022b), a random "hollow circles" distribution Lee and Jang (2021) and a multi-holes structure distribution Li et al. (2023b). Or, if we have already an initial rotor machine design it is possible to use this last as a starting point for the TO Hu et al. (2018). In this thesis,

we don't have any initial rotor geometry derived from previous parametric optimization. For this reason, we have chosen three different initialization patterns, illustrated in Fig. 3.6. The first consists in a homogeneous material distribution imposing a material density $\rho = 0.6$ over the entire domain (Fig. 3.6a). This density value is chosen based on the volume constraint of 60%. The second initialization is based on the previous pattern but introduces holes distributed along three different circumferences inside the rotor domain (Fig. 3.6b). These holes have a radius of 1.5 mm and are filled with a material density $\rho = 0.2$. For the third initialization, we use the same circumferences as in the second pattern, but the holes are strategically arranged. This configuration is based on the working principles of the SynRM, facilitating smooth magnetic flux flow along the $d-$axis and creating air barriers along the $q-$axis, as shown in Fig. 3.6c.

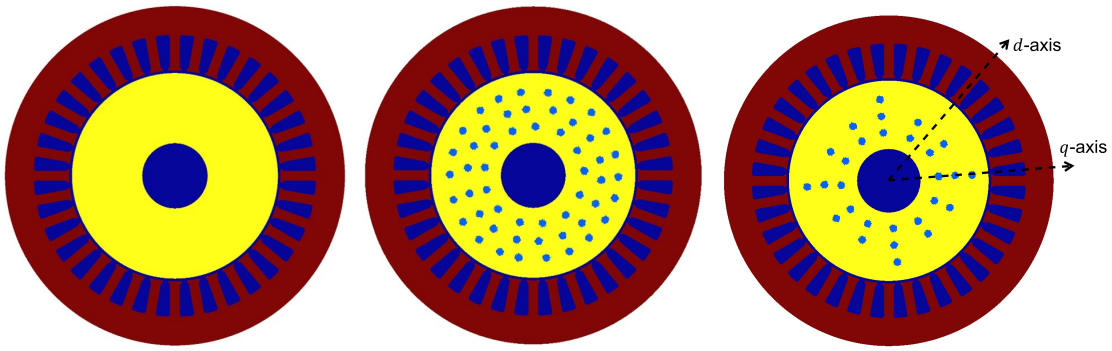

(a) Homogeneous density (b) Holes distribution (c) Holes distribution along $d-q$ axis

Figure 3.6: Different material distributions used for the initialization of the rotor domain.

It is important to note that throughout this thesis, various initial configurations and filter parameters were tested. In this manuscript, we have selected only a subset that provides a comprehensive representation of the findings.

In the following subchapters, we will first present a comparison of the two problem formulations introduced earlier. Next, both formulations will be analyzed using the three different material initialization patterns and two optimization algorithms, Generalized Optimality Criteria (GOC) and Method of Moving Asymptotes (MMA). This analysis will allow us to observe how, in gradient-based TO, the choice of initialization plays a critical role in shaping the final design. Additionally, solving the same problem with different algorithms can lead to slight variations in the final result, highlighting the sensitivity of the process to both the initial conditions and the optimization method used.

3.2.3.1 Comparison of average torque and energy formulation

In this subsection, we focus on comparing the average torque performance of the two different formulations: the traditional average torque formulation and the proposed formulation based on energy differences. The primary objective is to illustrate how the energy-based formulation, designed to maximize saliency, also effectively enhances average torque performance.

To provide a comprehensive comparison, the mean torque of the geometry obtained for the saliency maximization problems is computed at various stages of the algorithm. Specifically, we will compare the results from the two formulations, P_T and P_W, both initialized here with the $d-q$ axis holes distribution and solved using the MMA algorithm. It is important to note that the same outcomes are observed with other algorithms and initializations. The resulting torque evolution are presented in Fig. 3.7.

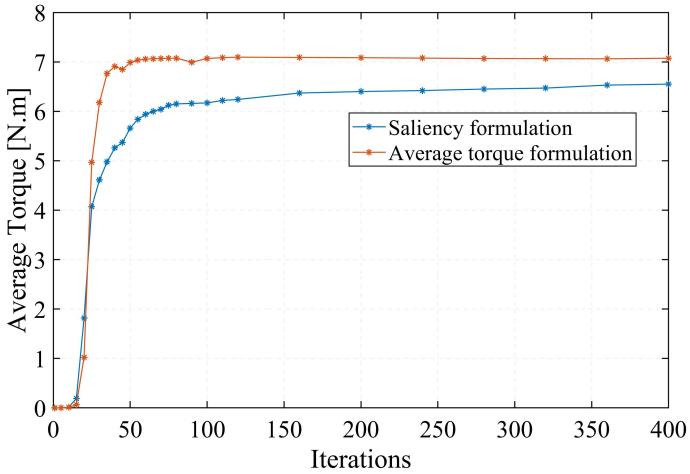

Figure 3.7: Comparison of the average torque value evolution between saliency (P_W) and torque (P_T) maximization problems.

As expected, the first observation is that the average torque increases during the optimization conducted with the saliency formulation, indicating that torque is effectively optimized by maximizing the saliency. The final torque values are 7.07 [N.m] for the average torque formulation and 6.55 [N.m] for the saliency formulation. Despite the slight difference in final torque values, the two formulations yield distinct optimal geometries, which will be detailed in the subsequent sections. Additionally, the figure shows that both formulations require approximately the same number of iterations to stabilize the average torque value. The average torque formulation (P_T) requires 45 finite element analyses (FEA) and an average time per iteration of 200 seconds. In contrast, the saliency formulation (P_W) requires only 2 FEA with an average time per iteration of

20 seconds.

This significant reduction in computational effort highlights the effectiveness of the saliency-based approach. By dramatically reducing the number of finite element analyses, it also lowers the total computational time. Moreover, this approach still results in increased average torque during the optimization process. With its energy-based objective function, the saliency formulation not only enables faster computations but also provides a highly effective means of optimizing torque performance, making it a good alternative for this type of optimization problem. However, it is important to note that the torque-based formulation generally achieves the highest average torque.

3.2.3.2 Average torque formulation results

In this subsection, the results obtained by the problem formulation aimed at maximizing the average torque, referred as P_T, are presented. The figures below illustrate the resulting geometries obtained from solving the optimization problem. Each figure includes three key components: the rotor geometry characterized by the material distribution, the magnetic flux density distribution, and the corresponding torque profile computed over 90 mechanical degrees.

Each figures also highlights how the different material initialization patterns influence the final design. Additionally, results are shown for both optimization algorithms, GOC and MMA, allowing for a comparison of their performance and efficiency in solving the problem. This comprehensive analysis demonstrates the impact of both initialization and algorithm choice on the final rotor design and its overall magnetic performance.

First point, the homogeneous initialization does not result in a multiple-barrier configuration. With this starting point, a resulting large flux guide connects to the d-axis but struggles to form complete flux paths to the shaft. This limitation is likely due to the volume constraint imposed on the problem. On the other hand, the two hole-based initializations yield better material distributions, allowing the creation of multiple flux barriers. This improvement is not only seen in the design but also in performance, as the average torque achieved with the hole-based initializations is noticeably higher than with the homogeneous one. These findings emphasize how strongly the initialization influences the final optimization result, affecting both geometry and performance.

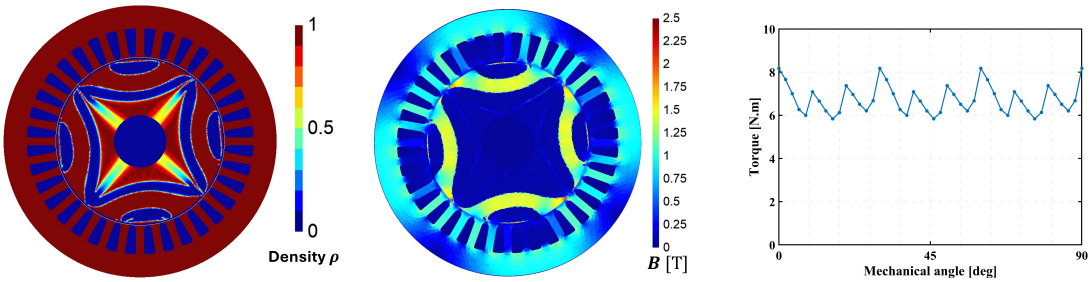

(a) Optimization result GOC (b) Magnetic flux distribution GOC (c) Torque profile GOC

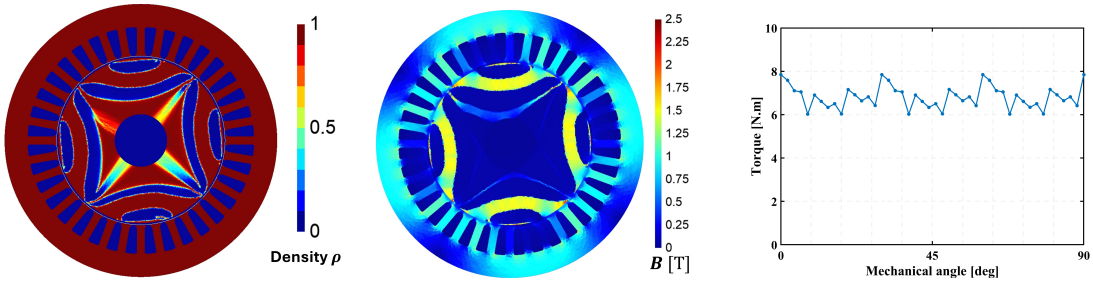

(d) Optimization result MMA (e) Magnetic flux distribution MMA (f) Torque profile MMA

Figure 3.8: Topologies obtained initializing the optimization problem P_T with **homogeneous material distribution**, from GOC (top) and MMA (bottom) algorithms.

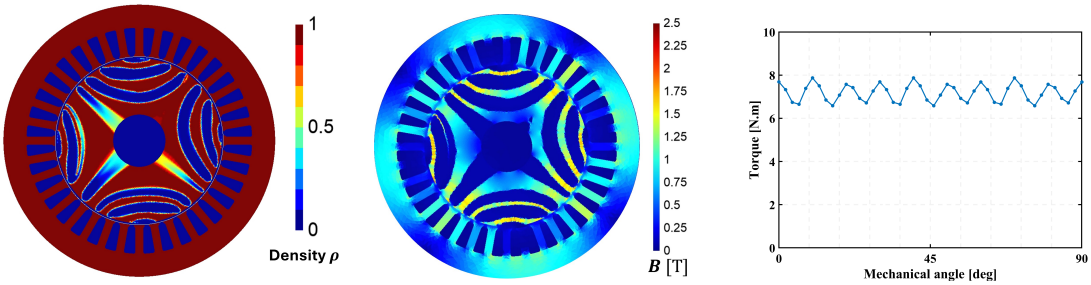

(a) Optimization result GOC (b) Magnetic flux distribution GOC (c) Torque profile GOC

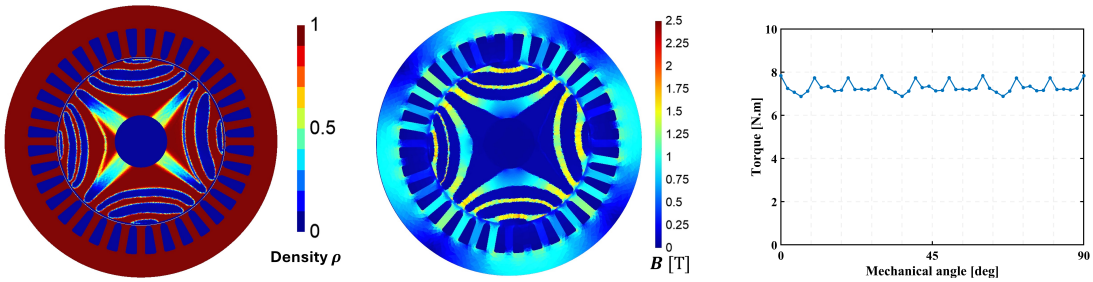

(d) Optimization result MMA (e) Magnetic flux distribution MMA (f) Torque profile MMA

Figure 3.9: Topologies obtained initializing the optimization problem P_T with **holes distribution**, from GOC (top) and MMA (bottom) algorithms.

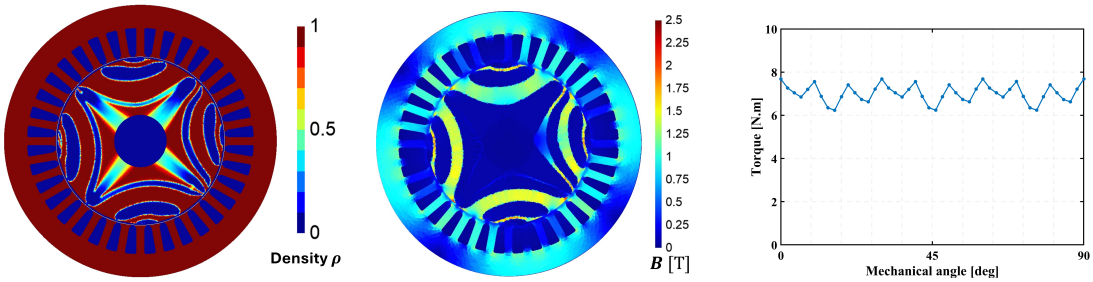

(a) Optimization result GOC (b) Magnetic flux distribution GOC (c) Torque profile GOC

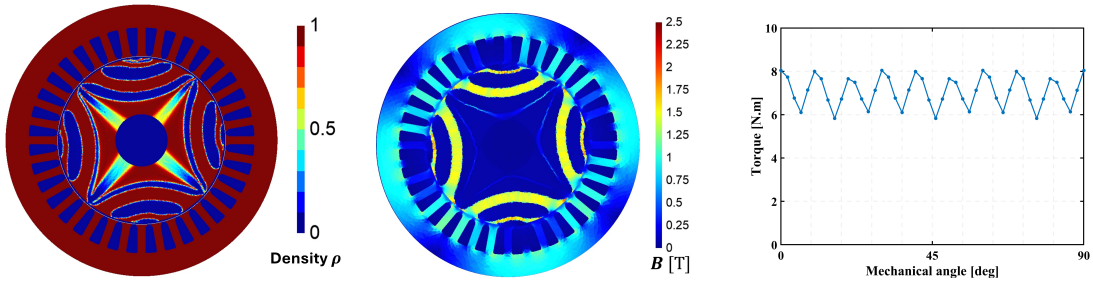

(d) Optimization result MMA (e) Magnetic flux distribution MMA (f) Torque profile MMA

Figure 3.10: Topologies obtained initializing the optimization problem P_T with **d-q axis holes distribution**, from GOC (top) and MMA (bottom) algorithms.

In addition to the effect of initialization, the choice of optimization algorithm also plays a significant role. When comparing GOC and MMA using the same initialization, we observe slight variations in the final designs and torque values. Specifically, MMA tends to offer a marginally higher torque compared to GOC. Each algorithm solves the problem differently, leading to variations in the material distribution, flux path development, and consequently, performance metrics such as the average torque in this case.

The obtained geometries, due to the use of density filter, are composed of smooth flux guides but with some intermediate materials, especially close to the rotor shaft where the magnetic flux is lower. These zones, analysing the magnetic flux distribution shown in Fig. 3.8 and Fig. 3.10, do not contribute to flux canalization. These intermediate materials could be removed using the Heaviside density projection, necessary if we want to manufacture the obtained geometries. Indeed, with the classical manufacturing process, the rotor sheets are composed only of pure ferromagnetic material. Given the current state of technology, it is not feasible to produce sheets composed with intermediate materials. As an example, after applying the Heaviside projection to the geometry in Fig. 3.8a we obtain a slight reduction of the average torque lower than 2%. The projection is made with the equation (2.73), using a value of $\beta = 200$ and $\eta = 0.5$ for the respective

parameters. This phenomenon can be attributed to the magnetic properties exhibited by areas containing intermediate materials, even those with a density $\rho < 1$. This can be better understood by referring to the Fig. 2.5 in Chapter 2, which illustrates the magnetization curve at varying densities. These zones slightly improve the magnetic field, leading to a modest enhancement in magnetization and flux conductivity compared to pure air

Finally, Table 3.2 summarizes the average torque values for the final geometries obtained from the different initializations and algorithms. These results confirm the earlier observations: the average torque obtained with the two hole-based initializations is higher than with homogeneous initialization. These data demonstrate that the choice of initialization significantly impacts the final average torque, with the hole-based designs yielding better outcomes. Additionally, when using the same initialization, solving the problem with different algorithms results in slightly different torque values.Notably, MMA offers a slightly higher final torque value than GOC, with differences ranging from 1$\%$ to 2$\%$ depending on the initialization.

Table 3.2: Average torque of final geometries obtained from the various initializations and the two algorithms (GOC and MMA).

Initialization	Algorithm	Average Torque [N.m]
Homogeneous	GOC	6.74
Homogeneous	MMA	6.82
Holes	GOC	7.18
Holes	MMA	7.30
Holes $d-q$	GOC	7.01
Holes $d-q$	MMA	7.07

In the following section, we will conduct a similar analysis for the problem formulated with saliency maximization. At the end of the analysis, we will compare the average torque values of the resulting geometries to evaluate the effectiveness of the saliency formulation used for optimize the machine and its potential advantages over the average torque formulation.

3.2.3.3 Saliency formulation results

As with the average torque formulation (P_T), the results for the saliency problem formulation (P_W) are obtained using the three different initializations and two algorithms, GOC and MMA. In the following figures are shown the final rotor geometries, highlighting, as discussed before, the influence of both the initial material distribution and the algorithm choice.

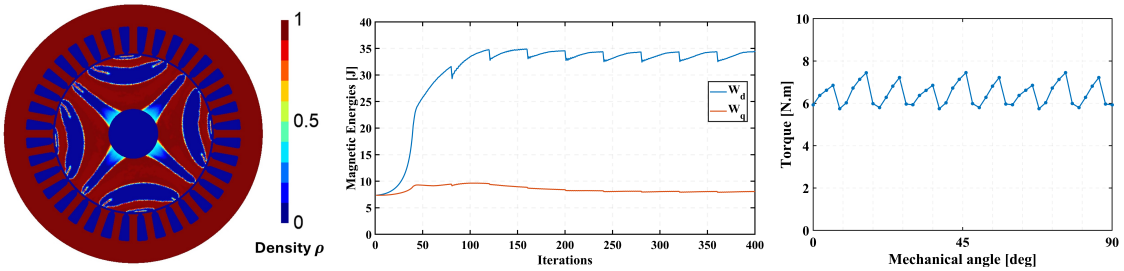

(a) Optimization result GOC (b) Energies evolution GOC (c) Torque profile GOC

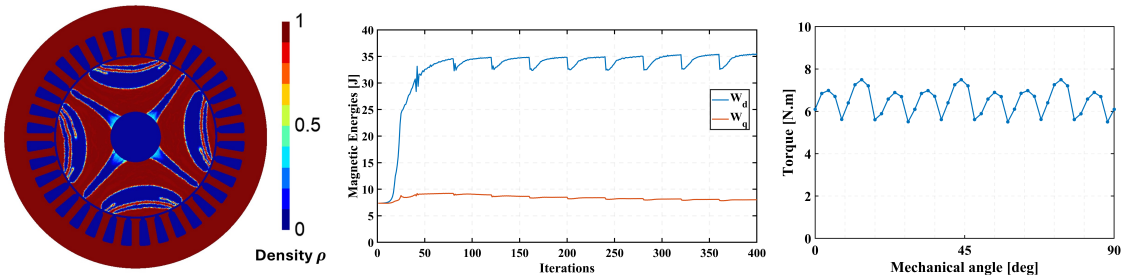

(d) Optimization result MMA (e) Energies evolution MMA (f) Torque profile MMA

Figure 3.11: Topologies obtained initializing the optimization problem P_W with **homogeneous material distribution**, from GOC (top) and MMA (bottom) algorithms.

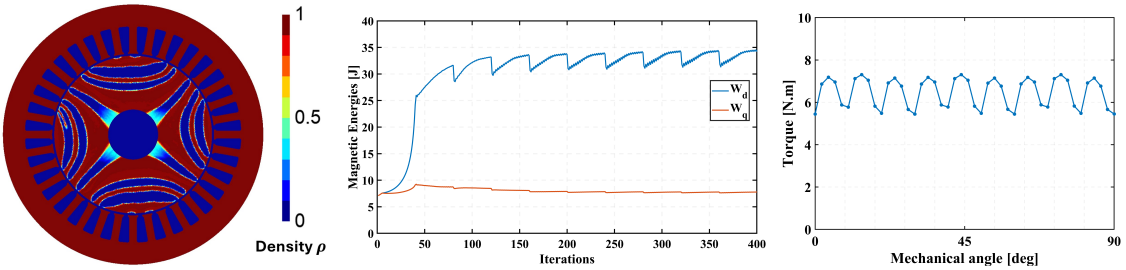

(a) Optimization result GOC (b) Energies evolution GOC (c) Torque profile GOC

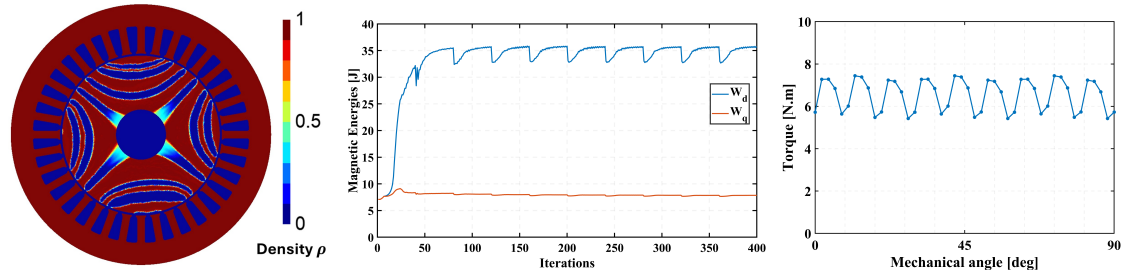

(d) Optimization result MMA (e) Energies evolution MMA (f) Torque profile MMA

Figure 3.12: Topologies obtained initializing the optimization problem P_W with **holes distribution**, from GOC (top) and MMA (bottom) algorithms.

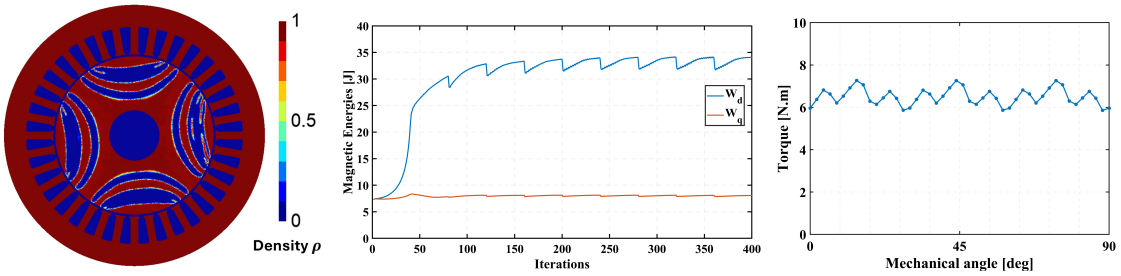

(a) Optimization result GOC (b) Energies evolution GOC (c) Torque profile GOC

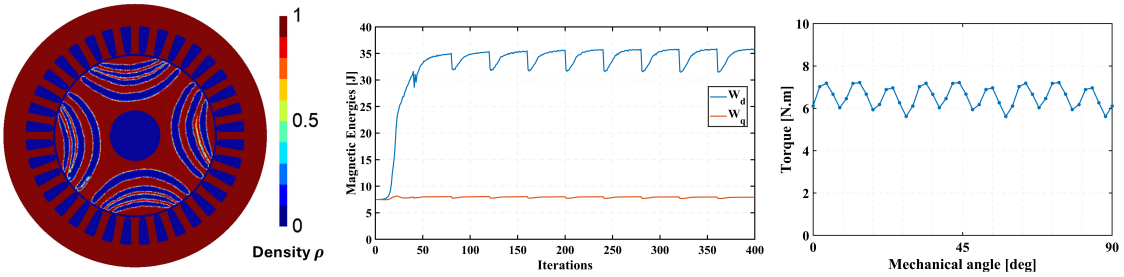

(d) Optimization result MMA (e) Energies evolution MMA (f) Torque profile MMA

Figure 3.13: Topologies obtained initializing the optimization problem P_W with **d-q axis holes distribution**, from GOC (top) and MMA (bottom) algorithms.

Consistent with previous observations, the initialization with predefined holes once again proves to be more effective in creating multiple air barriers. The uniform material initialization struggles to form these barriers, reinforcing the importance of how the TO problem is effected by the starting point. For what concerns the algorithms, MMA continues to outperform GOC in this regard, generating more additional flux guides, as particularly evident in the $d-q$ axis hole initialized designs (Figure 3.13). The results show that, while both algorithms produce comparable results, MMA has a slight edge in producing more effectively designed geometries.

A notable difference between the two formulations (P_T and P_W) is observed in the final material distribution. The average torque formulation tends to retain more intermediate materials during the optimization process. In contrast, the saliency formulation exhibits fewer intermediate material areas and features more distinct separation between ferromagnetic material and air. Consequently, the saliency formulation may offer a more accurate material distribution, potentially minimizing the need for extensive post-processing.

The optimization procedure, running for 400 iterations, achieves similar energy difference values (Δ_W), averaging around 27 J for all the optimization results. While the initialization significantly influences the final geometry, its impact on the energy values remains minimal, as seen in Table 3.3. This consistency in energy values shows that, although the design's shape are

strongly influenced by the initialization, the overall energy value remains steady across different configurations.

Table 3.3: Energy difference values of final geometries obtained from the various initialization and two algorithms

Initialization	Algorithm	Energy difference ($W_d - W_q$) [J]
Homogeneous	GOC	26.3
Homogeneous	MMA	27.4
Holes	GOC	26.5
Holes	MMA	27.8
Holes $d-q$	GOC	26.5
Holes $d-q$	MMA	27.9

As previously stated, the objective of this formulation is to maximize the average torque while requiring only two finite element analyses for each iteration step. Subsequently, a comparison between the two formulations (average torque and saliency) is expected. To achieve this analysis, the average torque of the topologies obtained through the saliency formulation will be computed and compared to the ones obtained from the torque formulation. Additionally, the computation time needed for convergence will be discussed. The instantaneous torque is computed, as for the problem P_T, with 45 magnetostatic analysis over a mechanical angle $\theta = 90°$ and a current phase angle $\phi = 45°$. The average torque values are compared in Table 3.4.

Table 3.4: Average torque comparison between the two problem formulations P_T and P_W

Initialization	Algorithm	Average Torque [N.m] from optimization problem P_T	Average Torque [N.m] from optimization problem P_W
Homogeneous	GOC	6.74	6.45
Homogeneous	MMA	6.82	6.51
Holes	GOC	7.18	6.47
Holes	MMA	7.30	6.53
Holes $d-q$	GOC	7.01	6.50
Holes $d-q$	MMA	7.07	6.55

The comparison shows that the average torque values obtained from the two different problem formulations P_T (for average torque maximization) and P_W (for energy difference maximization or saliency-based formulation) are relatively close. The average torque obtained with saliency formulation is slightly lower (about 4-10$\%$) across all initializations and algorithms. This reduction in torque highlights that the energy difference approach sacrifices a minimal amount of torque, while offering several significant advantages, such as reduced computation time and improved efficiency in generating optimized flux paths.

In terms of computation time, the benefits of the P_W formulation become even more evident. When using the GOC algorithm, the mean computation time for 400 iterations on a laptop is

around 2 hours and 30 minutes for P_W, compared to 24 hours for P_T. Similarly, with the MMA algorithm, the time required is about 3 hours for P_W, whereas P_T takes approximately 28 hours. This substantial reduction in computation time, coupled with the minor torque reduction, demonstrates that the P_W formulation offers a well-balanced compromise, providing comparable torque performance while significantly optimizing computational efficiency and other design factors.

3.2.4 Magnetostatic optimization section summary

This section focused on the magnetostatic optimization of the rotor of a SynRM. Two different problem formulations were proposed, and the first observation was that the saliency formulation, which maximized the magnetic energy difference, offered significant advantages over the average torque formulation. Specifically, this approach not only reduced the computational time but also achieved a comparable mean torque value. Although the average torque obtained with the energy difference formulation was slightly lower (by approximately 4-10$\%$) than the other formulation, it provided a good compromise between performance and computational efficiency.

Additionally, this section highlighted the critical impact of problem initialization and the choice of optimization algorithms. The results demonstrated that different initializations led to distinct final geometries and performance outcomes. Similarly, while both algorithms produced similar results under the same conditions, MMA generally excelled in creating additional flux paths. These observations underlined the importance of both initialization strategies and algorithm selection in achieving optimal designs in magnetostatic optimization

It was also observed that all the obtained designs were characterized by fluid-shaped barriers. This type of shape offered benefits in routing the d-axis flux, increasing the direct inductance, while exhibiting the same behavior of other types of barriers (circular and rectangular) in obstructing of the q-axis flux Gamba et al. (2014) Murataliyev et al. (2022). This made fluid-shaped barriers preferable for improving the performance of SynRMs.

In this problem configuration, optimal magnetostatic topologies of the rotor were obtained. However, the ferromagnetic flux guides were not connected, making the design mechanically infeasible. The rotor, in fact, lacked the mechanical ribs necessary to ensure structural integrity and withstand mechanical stress. This issue arose because optimizing only for electromagnetic performances led to material distribution that minimized flux leakage, which is typically present in ribs. Thus, optimizing only the magnetic performance was not a viable solution from a manufacturing perspective. Consequently, it became essential to consider the mechanical

behavior of the rotor, since mechanical stresses are generated in conjunction with the rotational speed. In the following sections, the mechanical aspects will be addressed in two different ways: a two-stage magneto-mechanical approach and a simultaneous approach.

3.3 Two-step magneto-mechanical optimization

The magnetic topology optimization aims to maximize the average output torque, which tends to eliminate all the rotor mechanical bridges that we usually find in SynRM rotor designs. The integration of structural topology optimization is needed to ensure that the rotor core overall stress is under the material structural limits and the maximum deformation at the air-gap is low. This is accomplished by performing rotor optimization with rotor compliance minimization. Furthermore, the Von-Mises stress is controlled during the optimization process to ensure the stress does not exceed the yield strength of electrical steel at the machine design speed. The ultimate goal is to enhance magnetic performance while simultaneously mitigating mechanical stresses, which presents a multi-physical challenge.

3.3.1 Formulation of the mechanical optimization problem

To tackle the multi-physical problem, a two-step approach is firstly adopted. We will explain this approach in detail. The initial step is to obtain a magnetically optimal geometry, which is achieved by applying the methodology presented in the previous section. This two-step approach consists in using the magnetic optimal topology, previously obtained, as the starting point for further mechanical optimization to ensure a structurally feasible design. For this second step, only the flux barriers composed of air domains constitute the new design domain, defined by Ω_{air}[1]. A similar approach was proposed in Credo et al. (2020), where the magnetic rotor structure is obtained through classical parametric optimization, with the tangential bridges near the air-gap being imposed and topology optimization is employed only for the purpose of obtaining the radial bridges within the flux barriers.

The mechanical optimization is applied in order to generate the optimal shape and the best position for the mechanical bridges. The mechanical loading for the rotor are the centrifugal forces generated by rotational speed. The problem is formulated as:

[1] Note that before this step, a Heaviside projection is applied to the magnetic geometry to ensure that all material in the new non optimizable area are physical.

$$(P_M): \begin{cases} \min\limits_{\rho \in \Omega_{\text{air}}} & C(\rho) \\ \text{s.t.} & \dfrac{1}{V_{tot}} \displaystyle\sum_{e=1}^{N_{\text{air}}} \rho_e \Delta_e \leq V_{\%} \\ & \rho_{\text{min}} \leq \rho_e \leq 1 \end{cases} \tag{3.19}$$

where C is the rotor compliance value, derived from the equation (2.57) and computed over the entire rotor region. N_{air} is the total number of triangle elements that compose the flux barriers. While this number may slightly vary from one geometry to another, it remains around 14000 elements. It is recalled that a reduction in compliance results in a diminution of displacement. Finally, $V_{\%}$ represents the volume constraint, similar to the one applied for magnetic optimization. In this case, the volume ratio is set at 5% in order to improve mechanical behaviour while not disrupting too much the magnetic performances. It is crucial to note that in purely mechanical optimization, if no volume constraint is imposed, the optimization will naturally drive the design towards a full structure to maximize the stiffness. Therefore, when optimizing only the mechanical properties, it is essential to include a volume constraint to prevent the design from defaulting to a solid configuration.

An example of the problem initialization is given in Fig. 3.14, where the new optimization domain Ω_{air} is highlighted in yellow. The red magnetic parts, which represent the magnetic flux paths, are not subject to optimization and remain unaltered throughout the process.

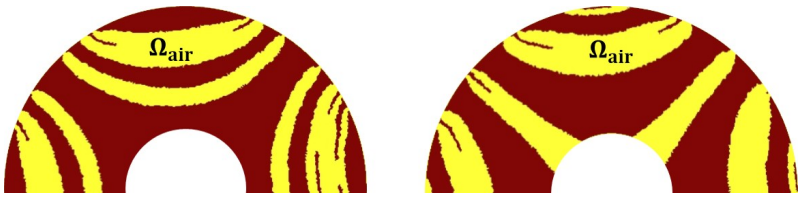

Figure 3.14: Magnetic optimal geometries (from the saliency formulation) with the definition of the new optimization domain Ω_{air} for the optimization problem P_M.

The presence of thin filaments in Fig. 3.14 results from flow paths that did not channel enough magnetic flux to grow and create a complete flux guide. As they interface poorly with the mechanical optimization and do not contribute to the magnetic performances they are filtered out manually before the next optimization step.

The proposed flowchart depicted in Fig. 3.15 illustrates the procedure of the two-step magneto-mechanical topology optimization.

The magnetic optimal geometries that we will consider for further mechanical optimization

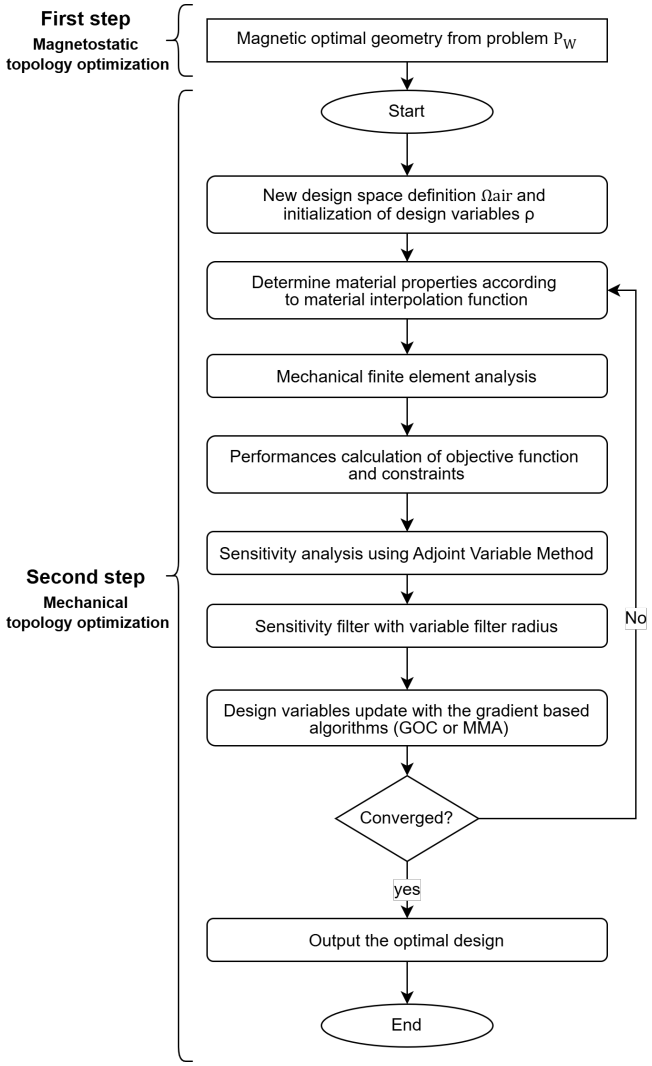

Figure 3.15: Flowchart of the 2-step magneto-mechanical TO procedure, with the different blocks description. In the second step the optimization problem P_M is solved.

result from the P_W saliency problem. After "cleaning" the geometries from the thin filaments when necessary, the solid parts of the design are fixed. A new design domain Ω_{air} is then defined, composed of all elements with a material density $\rho_e = \rho_{\text{min}}$, i.e. the air. This domain is then initialized with a uniform material distribution. The material properties of each element are thusly derived from the interpolation function (2.36) between the Young's modulus of magnetic steel E_{steel} and the one mimicking the air E_{min}. The penalization coefficient $q = 3$ is chosen, as good results have been reported in the literature Bendsøe and Sigmund (2004).

After the gradient calculation by the AVM, a sensitivity filter (see (2.72)) is applied at each iteration step. It is necessary to apply this filter at each iteration in order to prevent the occurrence of checkerboard patterns, which often occur in mechanical topology optimization. This ensures a more stable and physically meaningful material distribution throughout the optimization process.

This filter is applied to the gradient with a weighting function that depends on the radius dimension. The larger the radius is, the more the material distribution is "blurred" (more intermediate materials). An idea is to adjust the filter and make the material tend toward a final distribution almost free of intermediate materials by using a parameter that indicates the relative variation of the objective function. This parameter, named ε_F, is formulated by:

$$\varepsilon_F = \left| \frac{F_{\text{obj}}(\text{k}) - F_{\text{obj}}(\text{k}-1)}{F_{\text{obj}}(\text{k}-1)} \right| \times 100 \tag{3.20}$$

The filter radius is initialized with a values of 2 mm, four times the mesh size. Then, based on the value of ε_F, the radius is reduced. In the optimization process, a conditional update procedure is employed to adjust the mechanical filter radius r_{filter} and the variation limit *Varlim* based on the observed variation in the optimization variable. The procedure is outlined as follows:

Algorithm 1 Update Radius for Gradient Filter

$Varlim = 0.2$
  if $\varepsilon_F < Varlim$ **then**
    $r_{\text{filter}} \leftarrow \max(r_{\text{filter}} - 0.3 \times 10^{-3}, 0.55 \times 10^{-3})$
    new weighting function $w(x_i)$ based on equation 2.70
    $Varlim \leftarrow \max(Varlim - 0.05, 0.001)$
  end if

The main idea behind this procedure is to converge first towards a coarse blurred shape. When the convergence slows down (i.e. when the effect of the gradient and the filter start to cancel out), the radius r_{filter} is reduced, allowing finer and better defined shapes to emerge.

The stopping convergence criteria utilized is the maximum number of iterations of 500 or when the parameter ε_F is lower than 0.001.

Table 3.5 summarizes the material parameters and rotational speed responsible for generating the mechanical loads which are used in the optimization problem. This table will serve as a reference for the subsequent analysis. In the following sections, the focus will shift to the sensitivity analysis of compliance, and finally the results obtained will be thoroughly discussed.

Table 3.5: Mechanical parameters of the ferromagnetic material and considered speed.

Parameter	Value	Unit
Material density (γ)	7800	kg/m^3
Young's modulus (E_{steel})	200	GPa
Poisson's ratio (ν_p)	0.3	-
Yield strength (S_y)	400	MPa
Safety factor (SF)	2	-
Rotational speed	10000	rpm

As mentioned earlier, the objective is to reduce the mechanical compliance. The Von-Mises stress will also be checked during the optimization and the admissible stress σ_{vm} results:

$$\sigma_{vm} \leq \frac{S_y}{SF} \tag{3.21}$$

3.3.2 Sensitivity analysis of compliance

When considering the sensitivity analysis of compliance in mechanical TO problems, it is crucial to account for design-dependent centrifugal forces, especially in rotating machinery like electric machines. Centrifugal forces are inherently design-dependent because they depend on the mass distribution within the structure, which is directly related to the material density ρ. As the density distribution changes during the optimization process, the mass distribution and, consequently, the centrifugal forces will also change. These forces act radially outward from the axis of rotation, and the intensity is computed by 2.56. Considering these design-dependent centrifugal forces, the gradient will result slightly different compared to the one presented in most mechanical TO problems Bendsøe and Sigmund (2004) Deaton and Grandhi (2013) Gao et al. (2020). The compliance C is given by the expression:

$$C = F^T U = U^T K_s U \tag{3.22}$$

For applying the AVM, the residual r of the mechanical problem results in $r = K_s(\rho)U - F(\rho) = 0$, and the sensitivity of the compliance is written, considering the adjoint state variable λ as:

$$\frac{dC}{d\rho} = \frac{\partial C}{\partial \rho} + \lambda^T \frac{\partial r}{\partial \rho} \tag{3.23}$$

where λ is obtained from:

$$\frac{\partial r}{\partial U}\lambda = -\frac{\partial C}{\partial U} \tag{3.24}$$

It results that:

$$\begin{aligned} \lambda &= -2U \\ \frac{\partial r}{\partial \rho} &= \frac{\partial K_s}{\partial \rho}U - \frac{\partial F}{\partial \rho} \end{aligned} \tag{3.25}$$

The substitution of 3.25 into 3.23 yelds:

$$\frac{dC}{d\rho} = 2\frac{\partial F}{\partial \rho}U^T - U^T \frac{\partial K_s}{\partial \rho}U \tag{3.26}$$

where, the first term accounts for the direct influence of density on the centrifugal forces

applied to the rotor and the second term represents the contribution from changes in structural stiffness due to the density variations. It is seen that the sensitivity of the compliance can be both positive and negative. It may even change sign when the value of the design variable is changed. Therefore, the compliance exhibits non-monotonous behavior. The derivative for one element of the mechanical stiffness matrix and centrifugal loading forces with respect to the element density variable is easily found as:

$$\begin{aligned} \frac{\partial K_{se}}{\partial \rho_e} &= q(E_{steel} - E_{min})\rho_e^{q-1} K_{s_e}^{(0)} \\ \frac{\partial F_e}{\partial \rho_e} &= m_e r_e \omega^2 \end{aligned} \tag{3.27}$$

When the TO problem is constrained only by external forces that act outside the optimization domain, the gradient formulation simplifies. For example, in the case of stator optimization under fixed magnetic forces exerted on the stator teeth. As a result, the first component comprising the load vector F vanishes, thereby leading to the conventional formulation:

$$\frac{dC}{d\rho} = -\mathbf{U}^T \frac{\partial \mathbf{K_s}}{\partial \rho} \mathbf{U} \tag{3.28}$$

Incorporating centrifugal forces in the optimization process ensures that the resulting structure not only optimizes static compliance but also considers the dynamic effects induced by rotation. This is particularly important in applications such as electric motors, turbines, and other rotating machinery, where failure to account for these forces could lead to suboptimal or even unsafe designs.

3.3.3 Mechanical problem optimization results

In the process of analyzing the magnetostatic optimal geometry, it becomes evident that evaluating the mechanical performance of this geometry lacks practical significance. The key issue arises from the absence of any mechanical connections or material continuity that would ensure the structural integrity of the design.

When such disconnected parts are subjected to mechanical analysis, the resulting displacement and stress fields reveal significant deficiencies. Specifically, the compliance of the structure will be undesirably high, indicating a lack of rigidity. Furthermore, the displacement values, particularly in the flux guides that are not mechanically connected to the rotor or shaft, will be excessively large, often reaching magnitudes of several centimeters. In reality, these unconnected parts would have no structural support and would not remain in place. Therefore, the observed displacement values are purely a consequence of the chosen numerical stiffness of

the air and have no physical meaning.

To illustrate this point, Fig. 3.16 shows the displacement field of the magnetostatic optimal geometry under centrifugal force loads. The displacement field in 3.16b is presented using two different scales to highlight the displacement differences. In this figure, it is apparent that while the central part of the motor, which is mechanically anchored to the shaft, exhibits minimal displacement, the flux guides show significant displacements values, further emphasizing the impracticality of this geometry from a mechanical point of view.

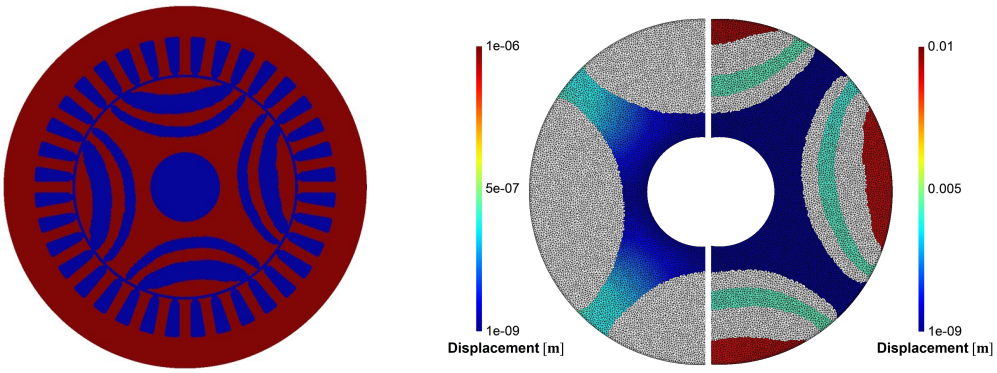

(a) Magnetostatic optimal geometry (b) Rotor displacements

Figure 3.16: Rotor displacements of the magnetostatic geometry obtained from one the previous optimization problems (P_W).

For the mechanical optimization, four geometries are selected from the previous magnetostatic optimization. We selected the two geometries derived from the distribution of holes on the $d-q$ axis, obtained from both algorithms. Subsequently, the others two are the geometry derived from the initial homogeneous distribution with GOC and the geometry derived from the random holes with MMA. Fig. 3.17 illustrates the geometries mentioned above. In some of these figures, we removed the previously observed material filaments, resulting in a much cleaner geometry compared to those shown in Fig. 3.14.

Using the methodology previously outlined, we now present the results obtained from the mechanical topology optimization. We begin by examining the outcome for geometry in Fig. 3.17a. Our first aim is to demonstrate how the variation of the filter radius influences the material distribution. Specifically, when the filter radius is large, the material distribution becomes more diffuse, or 'blurred', leading to a higher compliance value due to the intermediate material density that compose the bridges. As the filter radius is gradually reduced, the mechanical bridges transition towards a more solid material distribution with thinner, more defined structures. The impact of the proposed technique is illustrated in Fig. 3.18.

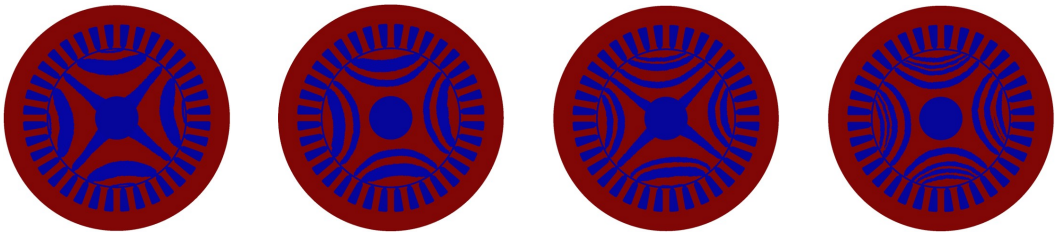

(a) GOC with homogeneous initialization

(b) GOC with d-q axis holes initialization

(c) MMA with random holes initialization

(d) MMA with d-q axis holes initialization

Figure 3.17: Geometries utilized as starting point for the mechanical topology optimization.

Initially, with a larger radius, the algorithm begins by placing material at optimal locations to form bridges. As the compliance value stabilizes, the filter radius is decreased, resulting in these bridges becoming less blurred and more sharply defined, ultimately converging towards the final optimized solution with almost a total iron composition.

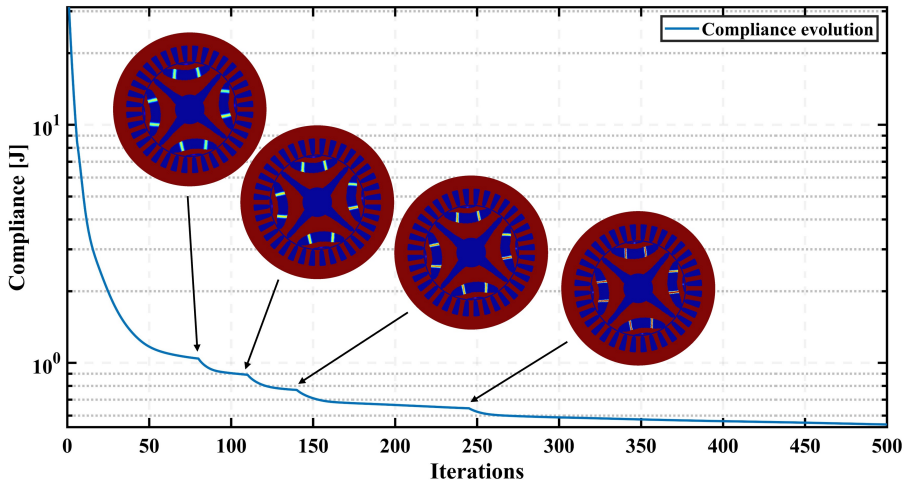

Figure 3.18: Compliance and geometry evolution with the effect of filter radius reduction during the optimization.

The optimization domain Ω_{air} is initialized with a homogeneous density $\rho = 0.05$ equal to the applied volume constraint. For this reason, the initial value of mechanical compliance is high.

The final material distribution resulting after the application of the density projection, the displacement map and Von-Mises stress distribution, are presented in Fig. 3.19. These results offer a comprehensive overview of the structural performance for the optimized geometry. The principal values derived from this analysis will be summarized in Table 3.6, after the presentation of supplementary results from the other geometries under analysis.

The following figures show the final material distributions, displacement maps, and Von Mises stress distributions.

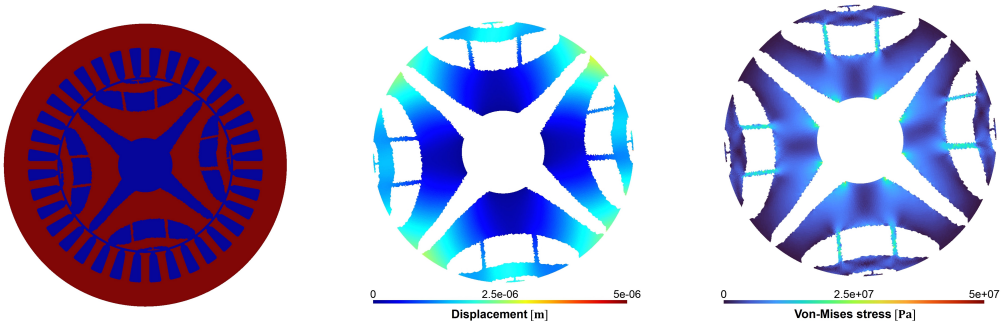

(a) Mechanical result (b) Displacements in meters (c) Von-Mises stress in Pascal

Figure 3.19: Mechanical TO result obtained using GOC and starting from the magnetostatic geometry 3.17a with the associated displacement (b) and Von-Mises stress distribution (c).

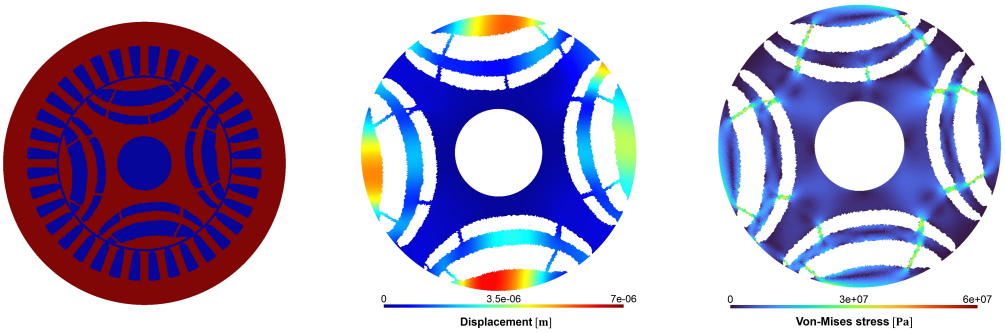

(a) Mechanical result (b) Displacements in meters (c) Von-Mises stress in Pascal

Figure 3.20: Mechanical TO result obtained using GOC and starting from the magnetostatic geometry 3.17b with the associated displacement (b) and Von-Mises stress distribution (c).

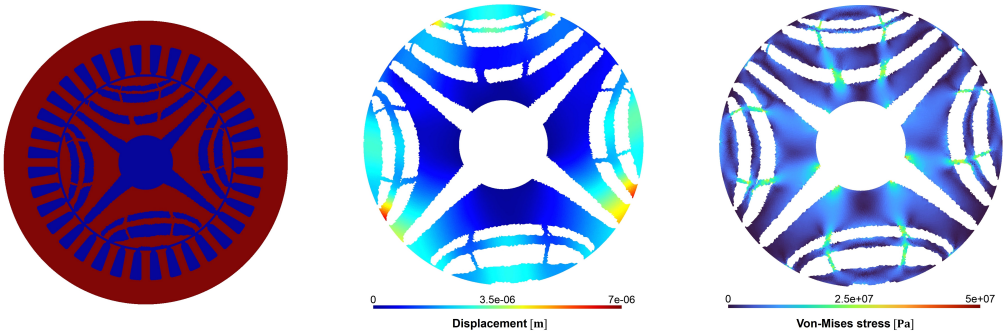

(a) Mechanical result (b) Displacements in meters (c) Von-Mises stress in Pascal

Figure 3.21: Mechanical TO result obtained using MMA and starting from the magnetostatic geometry 3.17c with the associated displacement (b) and Von-Mises stress distribution (c).

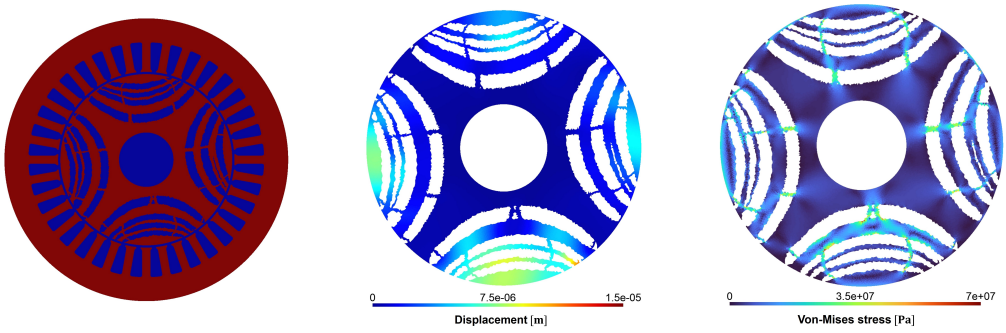

(a) Mechanical result (b) Displacements in meters (c) Von-Mises stress in Pascal

Figure 3.22: Mechanical TO result obtained using MMA and starting from the magnetostatic geometry 3.17d with the associated displacement (b) and Von-Mises stress distribution (c).

The mechanical topology optimization applied to the air barrier regions of the synchronous motor geometries has yielded some interesting results. By the introduction of mechanical bridges within these domains, we've managed to improve the mechanical rigidity of the rotor. These bridges help to reduce both the maximum displacement and the Von-Mises stress.

However, in the new "optimal" design, magnetic performances are reduced as mechanical bridges also act as magnetic flux paths, disrupting the torque. To better illustrate this effect, the flux distribution before and after the addition of the bridges is shown in Fig. 3.23.

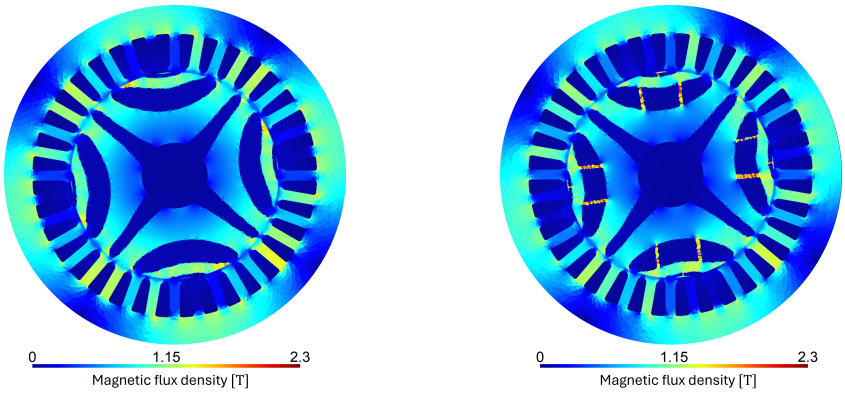

(a) Magnetic flux distribution of magnetostatic optimized geometry

(b) Magnetic flux distribution after mechanical optimization

Figure 3.23: Magnetic flux distribution before (a) and after (b) the mechanical topology optimization.

The detailed results of all the mechanical optimizations are summarized in the Table 3.6 below. This will allow us to directly compare the mechanical performance with the original magnetically optimized geometry and better understand the impact of these changes.

The results presented in Table 3.6 provide valuable insights into the effects of the two-step

Table 3.6: Performances results with the magnetic performances comparison (before/after mechanical optimization) and summary of mechanical criterion values

Starting Geometry	$C[J]$	u_{max} [mm]	σ_{max} $[MPa]$	T_{avg} [N.m] before mechanical TO	T_{avg} [N.m] after mechanical TO
3.17a	0.52	0.0048	37	6.45	5.76 (-10.7%)
3.17b	0.98	0.0061	55	6.50	5.63 (-13.4%)
3.17c	0.75	0.0064	40	6.53	6.04 (-7.5%)
3.17d	1.22	0.0113	65	6.55	5.90 (-9.9%)

topology optimization approach, particularly with regard to the mechanical performance of the rotor's structures. The mechanical optimization problem, P_M, primarily aims to minimize the compliance (C), which is a measure of the rotor mechanical rigidity under loading.

From the table, it is also evident that the mechanical optimization significantly reduces the maximum displacement (u_{max}) across all geometries, ensuring structural rigidity. This, combined with the fact that the Von Mises stress (σ_{max}) remains below the 200 MPa safety threshold, highlights that the compliance minimization has been successful in achieving a robust design without exceeding material limits.

Among the four geometries, the one initialized with 3.17d, which features the highest number of air barriers, exhibits the highest compliance value (1.22 J), along with the largest displacement and stress value. This can be attributed to the more complex structure, as more air barriers introduce greater mechanical complexity, requiring stronger ribs and increased material to maintain stiffness and stability.

However, while the compliance and mechanical strength have been improved, these changes come at the expense of magnetic performance. The introduction of mechanical bridges causes magnetic flux paths to be disrupted. This leads to a decrease in average torque after the mechanical optimization. Specifically, the reduction ranges from 7.5% to 13.4%, as indicated by the change in torque values before and after the mechanical optimization.

This trade-off between mechanical strength and magnetic performance is a key consideration for the design, and will be further analyzed in the next section to assess how these factors can be balanced in future iterations.

3.3.3.1 Trade-off between magnetic and mechanical performances

In this section, we explore the inherent trade-off between the magnetic performances represented by the average torque T_{avg}, and the mechanical performances represented by the compliance C. For doing this analysis, we solve the TO P_M problem (3.19) setting the volume constraint to different values ranging from 3% to 15%. The starting magnetic geometry chosen for this analysis

is the one obtained from the $d-q$ axis holes initialization with the use of MMA algorithm (Fig. 3.17d). The optimized designs obtained with different volume constraints are shown in Fig. 3.24. Following, the average torque and compliance correlation with the variation of volume constraint is given in Fig. 3.26. To facilitate visualization and interpretation, compliance is presented as its reciprocal, stiffness. Thus, higher stiffness values correspond to a more rigid structure and lower compliance, while lower stiffness values indicate greater compliance values.

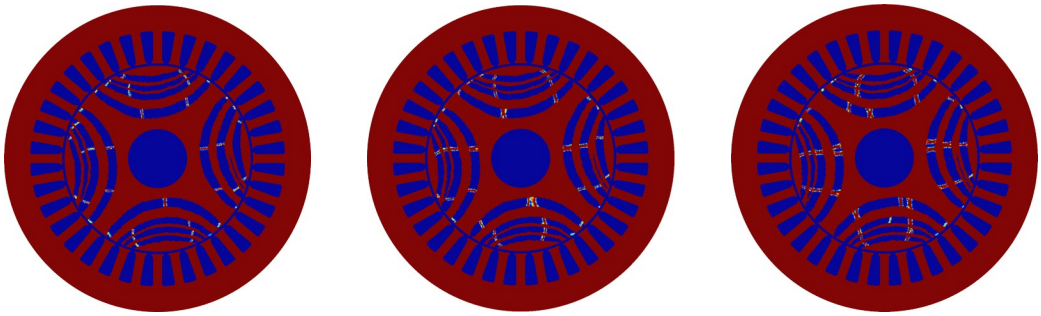

(a) $V_{\%} = 3\%$ (b) $V_{\%} = 6\%$ (c) $V_{\%} = 9\%$

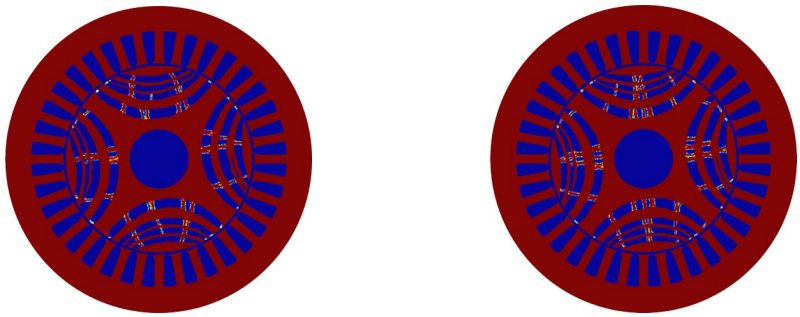

(d) $V_{\%} = 12\%$ (e) $V_{\%} = 15\%$

Figure 3.24: Mechanical TO problem (P_M) results obtained from different volume constraints $V_{\%}$.

In Fig. 3.24 we observe that at lower volume constraints, such as $V_{\%} = 3\%$, the mechanical bridges are composed predominantly of intermediate-density material, as the volume constraint is insufficient to generate fully dense structures. The aforementioned intermediate-density bridges are most evident and are illustrated in Fig.3.25 (left side).

As the volume constraint is relaxed bridges start to appear becoming thicker and more defined as more material is allowed in the design area. Specifically, we observe the formation of multiple bridges in the air barrier regions. With the highest volume constraints, the multiple bridges also start to concentrate along the $q-$axis as illustrated in Fig.3.25 (right side), further reinforcing the structure and enhancing mechanical support at the expense of degrading the magnetic performance.

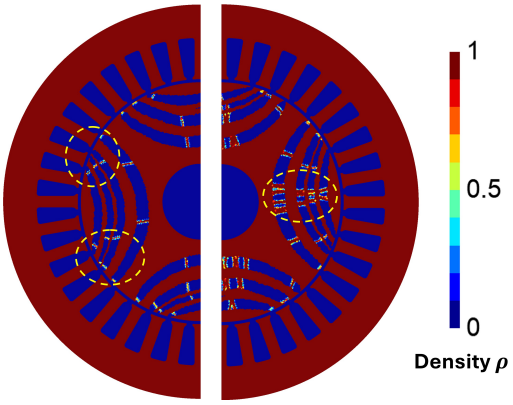

Figure 3.25: Material distribution in air barriers areas. On the left side the geometry with $V\% = 3\%$ highlighting the intermediate-density bridges. On the right side the geometry with $V\% = 15\%$ highlighting multi-bridges along the $q-$axis.

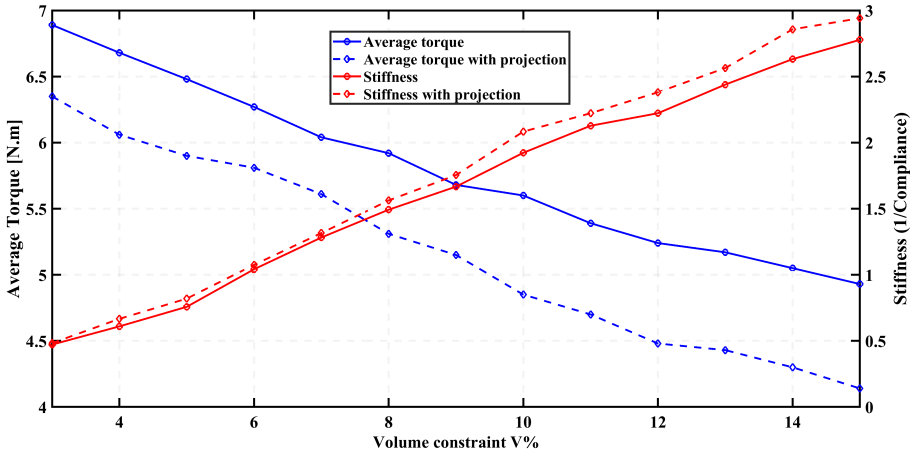

Figure 3.26: Relationship between mechanical volume constraint, average torque and compliance without and with Heaviside density projection.

The Fig. 3.26 illustrates the clear trade-off between average torque and stiffness. As the volume constraint increases, the rotor's stiffness improves, at the cost of reduced average torque. The torque and compliance after the Heaviside density projection are also computed and illustrated in the figure. A comparison of the various curves reveals that, after the projection, there is only a slight variation in stiffness, whereas there is a notable decrease in magnetic torque, amounting to a reduction of between 7 and 15 $\%$.

This trend highlights the inverse relationship between the magnetic and mechanical performances. The reason is that increasing the volume constraint results in thicker rotor ribs, which carry more magnetic flux, leading to higher flux leakage through the rotor ribs. This, in turn, reduces the available magnetic saliency and, consequently, the torque of the machine. In the figure above, we can clearly observe how the magnetic torque, initially around 6.9 $N.m$ at a minimum volume constraint of 3%, experiences a significant reduction of approximately 30%,

ultimately reaching a value of 4.9 $N.m$ as the volume constraint increases. Conversely, the compliance shows a notable improvement, decreasing from a value of 2 to a value of 0.36.

A closer analysis of the flux distribution in the rotor for geometries with 3% and 15% volume constraints reveals the increased flux leakage in rotor ribs, as showed in Fig. 3.27.

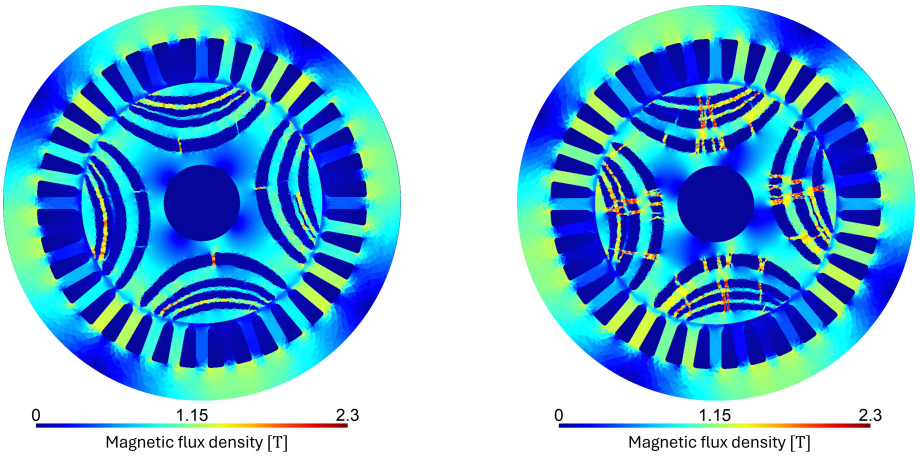

(a) Magnetic flux distribution from $V_{\%} = 3\%$

(b) Magnetic flux distribution from $V_{\%} = 15\%$

Figure 3.27: Magnetic flux distribution comparison with different volume constraints.

In summary, increasing the volume constraint allows for more material to be distributed throughout the rotor, enhancing structural rigidity through the formation of additional and thicker bridges. However, this increased material for mechanical optimization negatively impacts the machine's average torque, highlighting the inherent trade-off to be considered between mechanical and electromagnetic performance. This trade-off is a crucial consideration in the design process, as it requires balancing the need for mechanical strength with the desired electromagnetic efficiency. The results demonstrate that this trade-off must be carefully considered based on the specific performance requirements. For example, in high-speed applications where speeds reach 20,000 to 30,000 rpm, mechanical bridges become more critical than magnetic performance, as they ensure structural integrity under extreme operating conditions Babetto et al. (2018b).

3.3.4 Discussion on the two-step optimization approach

This two-step optimization approach enhances the mechanical properties of the design but raises a critical question: how can we ensure that the mechanical optimization step does not significantly compromise the performance achieved during the initial magnetostatic optimization. In particular, we observe that mechanical optimization often leads to a reduction in average

torque.

Ideally, the optimization process should simultaneously address both magnetic and mechanical performances. By considering these two objectives together, a balanced problem formulation can be developed, ensuring that the design optimized for magnetic performance also satisfies key mechanical constraints without sacrificing significant torque or other functional properties. This raises an intriguing question: would a combined, simultaneous optimization of both magnetic and mechanical objectives yield better overall results? This will be further explored in the next chapter, where a unified approach is examined to see whether it can offer a more effective trade-off between mechanical integrity and magnetic efficiency.

3.4 Coupled magneto-mechanical optimization

Simultaneous optimization of magnetic and mechanical aspects is crucial in designing efficient and robust synchronous reluctance motors. Some of the proposed methods in the literature separate these two aspects with a sequential geometry evolution, first optimizing the magnetic performance to enhance torque and then addressing the mechanical design to ensure structural integrity Lee et al. (2023); Credo et al. (2020). While this approach simplifies the optimization problem, it often leads to compromises where improving one aspect negatively effect the other, as we observed in the previous section. The coupled magneto-mechanical topology optimization allows to consider the two physics simultaneously and balance the two factors during the optimization procedure.

In this section, we explore a method that allows for the simultaneous optimization of both the magnetic and mechanical properties of a SynRM rotor. The critical challenge is to achieve an appropriate balance: it is essential that the rotor be capable of efficiently guide the magnetic flux to generate sufficient torque while simultaneously exhibiting sufficient structural integrity to withstand the mechanical loads to which it is subjected. Achieving this requires an accurate problem formulation that can handle the complex interactions between the magnetic and mechanical fields. In what follows, we will first address the flowchart of the optimization problem, after which the formulation of the magneto-mechanical problem will be discussed.

3.4.1 Formulation of the coupled magneto-mechanical optimization problem

The flowchart of the proposed coupled magneto-mechanical optimization problem combines several blocks used in previous optimizations, but is not very different from what has been presented so far. The flowchart is illustrated in Fig. 3.28.

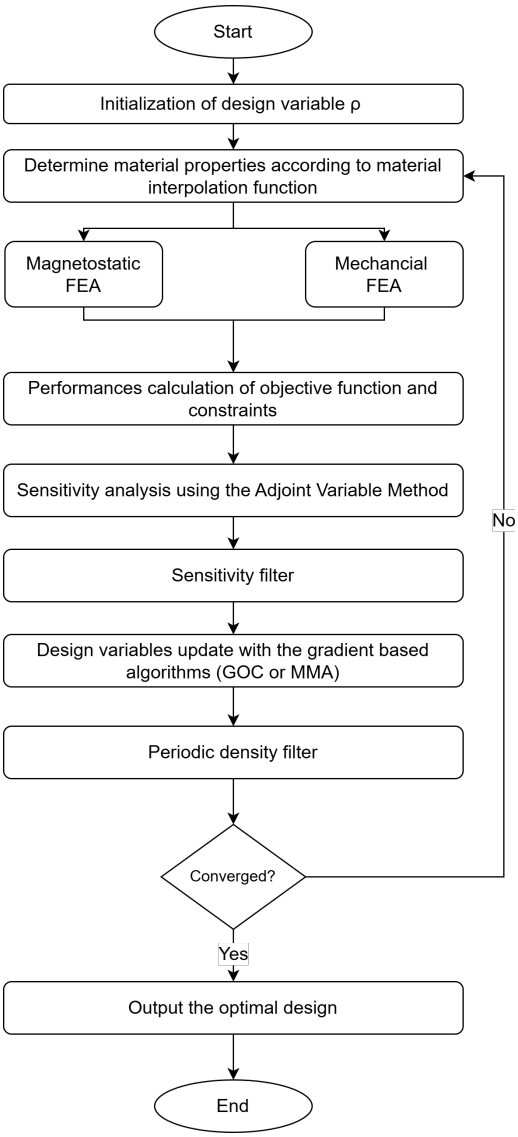

Figure 3.28: Coupled magneto-mechanical topology optimization procedure flowchart.

The entire rotor domain is selected as the optimization region. After the initialization of the design variable, the material properties are assigned through the material interpolation functions. Unlike the purely mechanical optimization where a penalty coefficient $q = 3$ is used, here $q = 8$ is applied. This adjustment is necessary because, with $q = 3$, the magnetic effects dominate, preventing the formation of mechanical bridges. In Sigmund and Maute

(2013) is reported that the determination of a penalty parameter strongly depends on the multi-physics problem being considered. In our magneto-mechanical optimization, by increasing q to 8, the mechanical behaviour is better represented, allowing the optimization to generate viable mechanical structures. The FEAs are done in parallel and the performances of the optimization problem are computed with the respective sensitivity analysis using the AVM. The formulation of the problem and the critical decision of what to define as the objective function and what to treat as constraints will be discussed in the following section. It will be shown that this choice significantly influences the outcome of the optimization process. The sensitivity filter is then applied to both magnetic and mechanical gradients, as previously mentioned, this filter helps to avoid the formation of checkerboard patterns. In this coupled problem, the two filter radii do not vary during the optimization process and for the magnetic and mechanical gradients are fixed respectively at $0.6mm$ and $1mm$. The radius for the magnetostatic formulation is chosen to be close to the average mesh dimension ($0.5mm$) to not impact the optimization process. With the filtered gradient information, the new design variable distribution is obtained with the use of two possible algorithms: GOC or MMA. Finally, the density filter is applied with a periodicity of 40 iterations.

An observation of the entire flowchart reveals that it incorporates all the previously utilized filters, which were employed separately for the magnetic and mechanical problems.
In the following section, the choice of the optimization problem will be discussed. All the results are obtained with the material initialization derived from the $d-q$ axis holes initialization (Fig. 3.6c). This initialization has proven to be effective in achieving a multi-barrier flux configuration with appropriate symmetry. Additionally, this setup challenges the magneto-mechanical optimization problem, as it promotes the formation of multiple flux barriers while maintaining mechanical stability through carefully distributed bridges.

3.4.2 Choice of the optimization problem formulation

The magneto-structural optimization problem can be approached in two distinct ways: either by using electromagnetic performance as the objective function with mechanical performance as the constraint, or by inverting this relationship, making mechanical performance the objective while treating electromagnetic properties as constraints. In this study, we begin by choosing magnetic energy as the objective function, with mechanical compliance serving as the constraint, as detailed in the following formulation:

$$(P_{M-M}1): \begin{cases} \min\limits_{\rho\in\Omega} & -\Delta W(\rho) = -(W_d(\rho) - W_q(\rho)) \\ \text{s.t.} & C(\rho) \leq C_0 \\ & \rho_{\text{min}} \leq \rho_e \leq 1 \end{cases} \tag{3.29}$$

where the objective function is formulated to maximize the magnetic energy difference in $d-q$ axis and thus to maximize the average torque of the machine. The mechanical behaviour of the rotor is guarantee imposing a constraint, where C_0 is the maximum allowable compliance value. Here, C_0 is set to 0.8, referencing the previous optimization results from the 2-step optimization in Table 3.6. The volume constraint is not considered in this formulation as the simultaneous optimization will generate an optimal material distribution without the need to constraint a maximum allowable volume. For the pure mechanical optimization, with no volume constraint the algorithm will completely fill the air-barrier as a full geometry will have a lower compliance value. Here, the two physics are in opposition and then a non-full geometry will be naturally obtained.

This formulation, however, is not well suited to solve the coupled magneto-mechanical problem. Two results are presented in Fig.3.29, using the two algorithms (GOC and MMA). The dominance of magnetostatics over mechanics prevents the formation of mechanical bridges. Consequently, the inability of mechanics to create bridges gives rise to a more compact geometry in which the presence of multiple air barriers is precluded. The associated compliance and average torque are 0.76 J and 4.09 N.m for Fig.3.29a, 0.79 J and 4.15 N.m for Fig.3.29b. In both cases, the energy difference ΔW is approximately 20 J, which correlates to a relatively low average torque output. Therefore, it can be concluded that this specific problem formulation restricts the design's ability to achieve good performance, making this formulation unsuitable. The reduced design freedom impedes a good balance between mechanical integrity and electromagnetic efficiency, proving that this approach does not adequately address the complete performance requirements.

The second problem formulation is obtained inverting the objective and the constraint, leading to the following problem:

$$(P_{M-M}2): \begin{cases} \min\limits_{\rho\in\Omega} & C(\rho) \\ \text{s.t.} & W_d(\rho) - W_q(\rho) \geq \Delta W_{min} \\ & \rho_{\text{min}} \leq \rho_e \leq 1 \end{cases} \tag{3.30}$$

In this problem formulation, the mechanical compliance C is the objective function to be

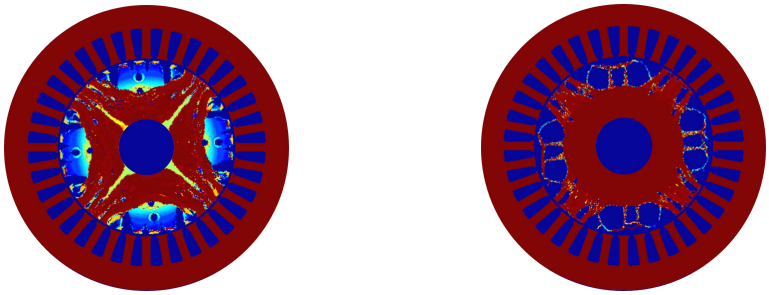

(a) GOC algorithm (b) MMA algorithm

Figure 3.29: Geometries obtained from the first optimization problem formulation, respectively with the two algorithms GOC (a) and MMA (b).

minimized, while ensuring magnetic performance by imposing a constraint on the $d-q$ magnetic energy difference by ΔW_{min}. The energy constraint is set at 25 J, value derived from the previous results in the magnetostatic and magneto-mechanical two-step optimizations.

Although this formulation yielded improved results compared to the previous approach, the GOC algorithm encountered significant difficulties in balancing the competing magnetic and mechanical physics. The main issue is the binary activation and deactivation of constraints controlled by a multiplier derived from the bisection method. This simplistic approach caused the magnetic behavior to dominate the optimization, leading to the formation of magnetic flux guides but failing to establish solid mechanical connections, an example in Fig. 3.30a with a final average torque of 5.20 N.m but a high compliance of 7.70 J.
Numerous tests were conducted to fine-tune the parameters, but none provided satisfactory results (Fig. 3.30b ,3.30c). Compliance could not be reduced effectively (around 2 J) despite the variation of the constraint multipliers for the magnetic energy. Moreover, one of the significant drawbacks of the GOC method is that for every change in the optimization problem or motor design, the parameters would need to be recalibrated, which would be time-consuming and inefficient.

To address these challenges, the MMA algorithm is adopted as a more suitable algorithm for this coupled magneto-mechanical optimization problem. It demonstrated smoother convergence behavior by managing the constraints more effectively through the optimization process.

In the next part, we will explore the results of the coupled optimization problem solved with MMA, including a detailed analysis of magnetic and mechanical performances.

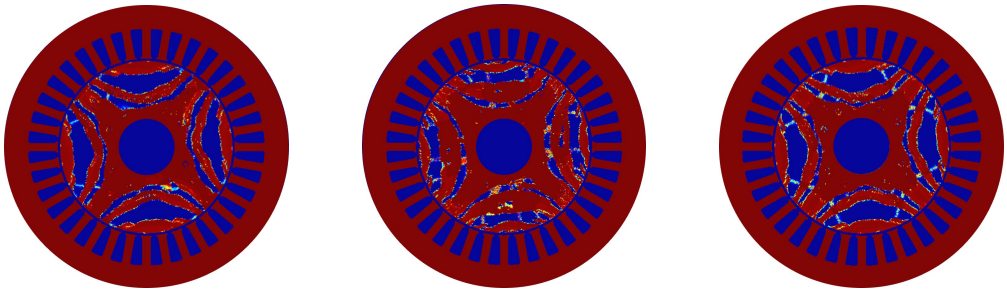

(a) Initial result (b) Result tuning the multiplier values (c) Result tuning the multiplier values

Figure 3.30: Results from the second optimization problem formulation, obtained with GOC algorithm.

3.4.3 Optimization results

In this section, we present the results of the magneto-mechanical coupled topology optimization. The optimization problem formulation $P_{M-M}2$ (3.30) is selected for the magneto-mechanical optimization and the optimization process is performed using the previously described framework in Fig. 3.28. Initializing with the $d-q$ axis hole distribution we obtain a clear multi-barrier rotor configuration and the presence of mechanical bridges in the air barrier, the final material distribution is illustrated in Fig. 3.31.

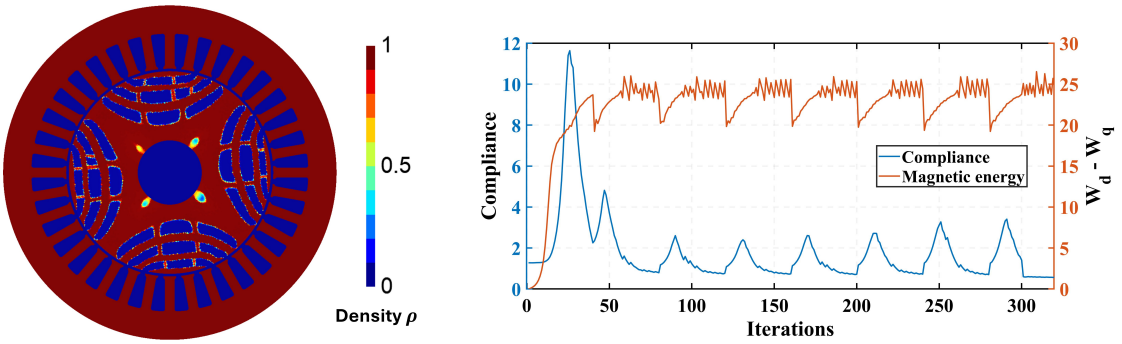

(a) Optimization result (b) Convergence evolution

Figure 3.31: Optimal magneto-mechanical geometry (a) and convergence evolution of objective function and constraint (b).

From the convergence curve (Fig. 3.31b) we can observe the evolution of two key metrics during the optimization process: the mechanical compliance (blue line) and the $d-q$ magnetic energy difference constraint (orange line). The compliance is successfully minimized, reaching a final value of $C = 0.6$ J, close to the values obtained from the two-step optimization. Additionally, the displacement and Von-Mises stress values align with the expectations for mechanical performance ($u_{max} = 10 \times 10^{-6}\, m$ and $\sigma_{max} = 57\, MPa$), remaining within the material and geometric limits

without exceeding critical thresholds. The compliance shows a peak at approximately 25 iterations, it arises as the material distribution first forms magnetic structures before establishing mechanical bridges, which later reduce the compliance value. The additional periodic peaks, on the other hand, are caused by the periodic density filter applied every 40 iterations. For the magnetic energy difference, once the quantity reach the minimum admissible value $\Delta W_{min} = 25J$ it oscillates around it.

The behavior of the opposing physics is clearly observed when comparing the gradients of the magnetic and mechanical functions. In Fig. 3.32, we see how these gradients provide insight into the underlying competition between magnetic and mechanical physics. Specifically, the mechanical bridges, highlighted in the circled area, show opposing gradient behavior.

The negative magnetic gradient shows that magnetostatic performance would benefit from thinner or nonexistent bridges, as material removal would decrease the flux leakage. On the other hand, the positive mechanical gradient demands material addition to maintain structural integrity.

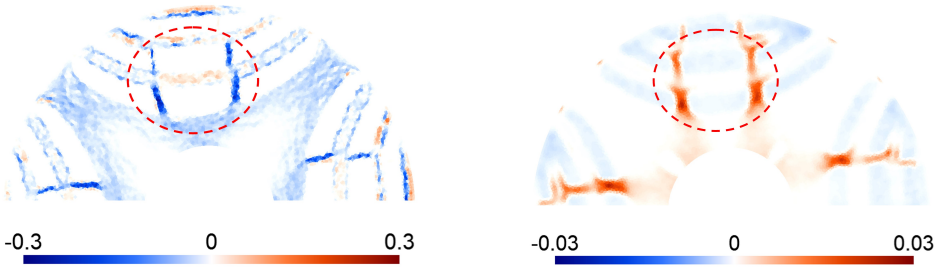

(a) Magnetic gradient (b) Mechanical gradient

Figure 3.32: Gradients of the magnetostatic function (a) and mechanical function (b).

This struggle between the need for material in mechanical bridges and its removal for optimal magnetic performance illustrates the inherent conflict in optimizing both domains simultaneously. The balance of these gradients is critical to achieve a geometry that satisfies electromagnetic and structural requirements without significant compromise in performance.

To verify the magnetic performance of the optimized geometry, the average torque was computed, yielding a value of 5.85 N.m. Additionally, we calculated the average torque at various stages of the algorithm and compared with the energy difference, the evolution curve is shown in Fig. 3.33. Due to oscillations in energy value, only a few points have been selected to provide a more effective visualization. It is noteworthy that the torque is again increased by formulating the magnetic problem as the difference of the d and $q-$axis energy, as we already shown in the magnetostatic optimization section.

The optimization results demonstrate that the final geometry achieves a robust balance

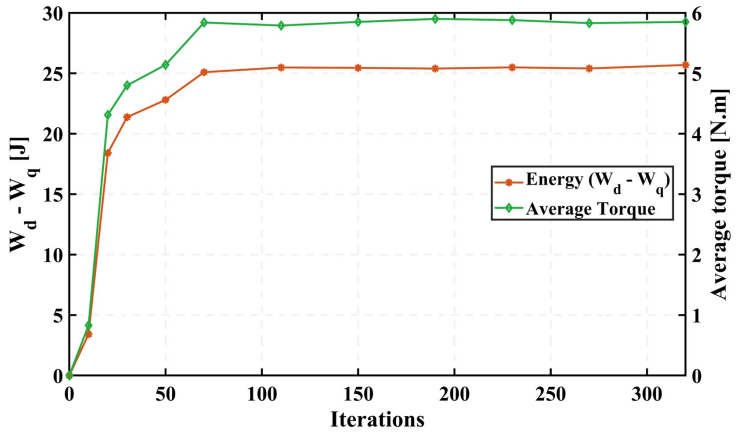

Figure 3.33: Magnetic energy difference ($W_d - W_q$) and average torque evolution during the optimization process.

between the competing magnetic and mechanical requirements. Mechanical bridges were formed effectively within the air barriers, leading to reduced displacements and improved structural integrity under mechanical loads. The optimized structure also ensured that Von-Mises stress values remain within safe limits, with a maximum value not exceeding the imposed safety limit of 200 MPa.

The geometry in Fig. 3.31 exhibits intermediate density regions, particularly in the mechanical bridges. To address the presence of these intermediate densities, a post-processing step utilizing Heaviside density projection can be applied to eliminate them and refine the structure. The resulting geometry, shown in Fig. 3.34, demonstrates a slight enhancement in mechanical performance, characterized by a compliance of 0.48 J and reduced displacement and Von-Mises stress values ($u_{max} = 5.8 \times 10^{-6}\, m$ and $\sigma_{max} = 43\, MPa$).

However, the magnetic analysis indicates a decrease in magnetic performance, with the average torque dropping to 4.70 N.m, presenting a 20 $\%$ reduction compared to the pre-projection configuration.

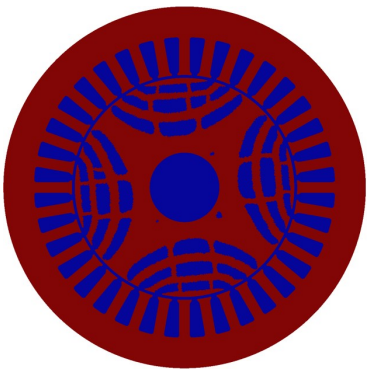

Figure 3.34: Geometry after the Heaviside density projection, with a full/void material distribution.

The performances before and after the projection are resumed in Table 3.7.

Table 3.7: Final design performance comparison

	Optimized geometry Fig. 3.31	Projected geometry Fig. 3.34
$W_d - W_q$ [J]	25	22.4
Mean torque [N.m]	5.85	4.70
Compliance [J]	0.57	0.48
Max Von Mises [MPa]	57	43
Max displacement [m]	10×10^{-6}	5.8×10^{-6}

As already discussed, we can observe the magnetic performances decrease with the projection, while the mechanical performances increase. This is because the bridges are made of solid material after being projected. The material has the physical properties of pure ferromagnetic material, which results in increased leakage flux and greater mechanical strength. The optimization results indicate that using intermediate materials with lower ferromagnetic properties for the bridges can improve magnetic performance by reducing leakage flux. This finding is consistent with previous studies in the literature that have explored the use of nonmagnetic bridges in rotor designs, such as Panda et al. (2020). However, the performance of electrical machines could be further improved by utilizing additive manufacturing techniques and their latest advancements Selema et al. (2022b). For example, additive manufacturing can be used to produce lattice structures for bridges, allowing for the creation of complex geometries that are challenging to achieve with traditional manufacturing methods.

3.4.4 Comparison between simultaneous and 2-step magneto-mechanical optimization

In this section, the results of the two optimization methods, two-step and simultaneous, are compared, both starting from the same initial density distribution. The comparison focuses on key mechanical and magnetic performance quantities, specifically torque and compliance. The motivation for this comparison is to understand the trade-offs and advantages of addressing mechanical and magnetic objectives sequentially versus simultaneously.

For the simultaneous approach, a Pareto front can be obtained varying the energy constraint ΔW_{min} from 27 to 15 J, and plotting the average torque and compliance for each optimum design. Additionally, the results of the two-step approach illustrated in Fig. 3.26 can be rearranged in order to obtain another Pareto front to be compared with the one obtained with the simultaneous approach. Fig. 3.35 shows the points obtained from the two-step and simultaneous topology

optimization approach.

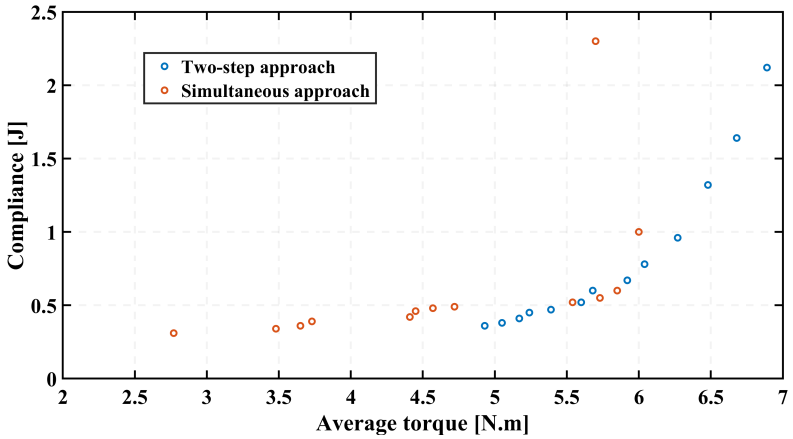

Figure 3.35: Pareto front obtained from the two-step approach (varying the mechanical volume constraint) and simultaneous approach (varying the energy constraint).

This figure demonstrates the trade-off between mechanical and magnetic performance in the designing of electrical machines when employing different optimization strategies. The two-step approach favors higher torque at the cost of higher compliance, particularly at higher torque values. In contrast, the coupled approach achieves a more balanced trade-off, maintaining relatively low compliance across the range of torque values. However, it does not achieve the highest possible torque values as the two-step method.

The results suggest that the coupled optimization approach may be more suitable for applications where mechanical robustness and deformation are critical, while the two-step approach could be beneficial when maximizing torque output is a priority, even if this leads to a significant increase in mechanical deformation.

With the two-step approach, we can control the mechanical volume fraction and, thus, the mechanical properties of the two physics. This allows us to increase or decrease mechanical quantities such as compliance, Von-Mises stress, and displacements. However, since this is done separately, the magnetic geometry remains unchanged. On the other hand, while offering lower torque, the coupled approach provides more balanced performances across both domains. Additionally, the resulting geometry from the coupled approach is more symmetric, particularly in the bridges, where the design benefits from improved structural integrity and stress distribution compared to the more asymmetric geometries of the two-step approach.

In conclusion, the coupled approach provides more mechanically stable designs for a given range of torque outputs, while the two-step method may offer better electromagnetic performance at the cost of mechanical integrity. One approach may be preferred depending on the specific design objectives (mechanical versus magnetic).

3.5 Chapter conclusions

In this chapter, we applied the topology optimization to the rotor design of a synchronous reluctance machine, investigating both electromagnetic and mechanical performance aspects. The study was divided into two main phases: an initial magnetostatic optimization and a following magneto-mechanical optimization.

For magnetostatic optimization, we examined two problem formulations: the conventional method based on average torque maximization and an alternative approach based on maximizing the magnetic energy difference between the d-axis and q-axis. The energy approach takes advantage of the idea that we can improve the machine saliency by optimizing the difference in stored magnetic energy between the two axes. This method simplifies the optimization process by directly focusing on the core principle that drives torque generation in synchronous reluctance machines. When comparing the two, the energy formulation demonstrated its ability to improve torque performance. Additionally, this formulation significantly reduces computational time, as it requires only two finite element simulations per iteration, in contrast to the multiple simulations needed for torque-based optimization. The results confirm that the energy difference formulation provides a valuable alternative to conventional methods.

For magneto-mechanical optimization, two different strategies were investigated:

1. Two-step approach: The magnetic optimization was followed by a separate mechanical optimization phase. By varying the volume constraint, this method provided control and adjustment of mechanical parameters such as compliance and displacements. However, this strategy resulted in a reduction in average torque, thus necessitating a trade-off between magnetic and mechanical performances.

2. Simultaneous approach: The magnetic and mechanical optimizations were conducted simultaneously. This approach ensured a balanced result by considering both physics together. The outcomes highlighted that this approach maintains mechanical integrity while achieving good electromagnetic performance.

Both optimization approaches offer unique benefits. The two-step method allows for the separate optimization of mechanical and electromagnetic characteristics, offering more flexibility in meeting particular performance specifications. This process, however, requires a trade-off, as the mechanical optimization in the second step results in the loss of average torque. On the other

hand, the simultaneous optimization method offers an optimized solution with a harmonious trade-off between electromagnetic efficiency and mechanical strength. Furthermore, the coupled optimization approach also offers new material possibilities, particularly in utilizing intermediate-density materials in rotor bridges. This enables better structure and magnetic performance and a promising path toward future synchronous reluctance machine design improvement.

Chapter 4

Topology optimization and vibration reduction

This chapter is dedicated to the topology optimization of an electrical machine, with the objective of reducing vibrations and resonances that occur during specific operating conditions. The motor design under analysis in this study is derived from the magneto-mechanical topology optimization carried out in the previous chapter.
In general, the study of vibrational behavior in electrical machines involves two fundamental analyses:

- **Electromagnetic analysis**: this part evaluates the forces arising from the electromagnetic interaction between the stator and rotor. These forces act as the primary drivers of vibration in the machine.
- **Mechanical analysis**: here, the natural modes of the machine's geometry are first evaluated, alongside the corresponding deformations and resonances that are induced by the electromagnetic forces. The mechanical analysis helps identify the critical frequencies at which resonance may occur.

The diagram in Fig. 4.1 illustrates the process of noise generation in electrical machines, while also providing an overview of the methodology employed to estimate the corresponding vibration response.

The vibration response analysis proceeds through several steps. First, the 2D electromagnetic forces acting on the teeth surfaces of the motor are calculated using the finite element (FE) method. Next, a structural FE model of the stator, including any additional housing, is developed. A modal

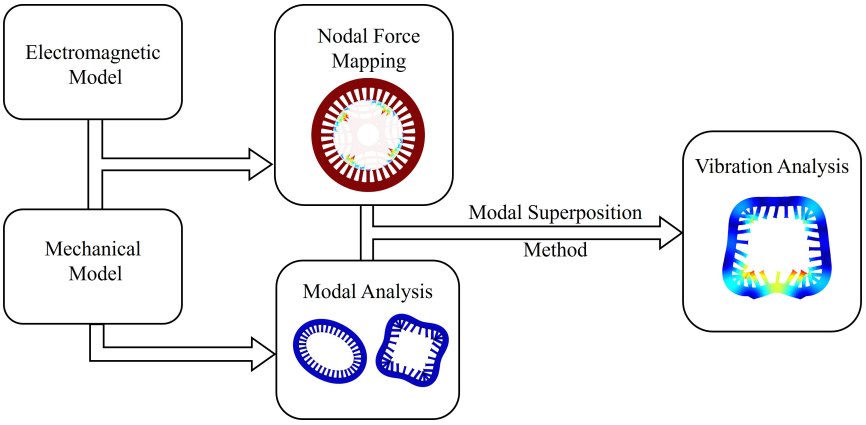

Figure 4.1: Overview of the magneto-vibratory analysis.

analysis is then performed to determine the modal parameters, specifically the mode shapes and natural frequencies. Finally, by combining the calculated electromagnetic forces with the modal data, a dynamic analysis is conducted to obtain the frequency response of the machine under the specified conditions.

This chapter is structured into three main sections. The first section introduces the origin of vibrations in electrical machines and outlines the steps required for conducting a dynamic analysis to obtain the vibration response. The second section summarizes the main applications of topology optimization in dynamic problems and discusses the different possible problem formulations. In the final section, the optimization problem is formulated and applied to the electrical machine. The results are analyzed, showing that this optimization approach is feasible, with opportunities for further refinement through additional analysis.

4.1 Vibrations in electrical machine

The overall noise level of an electrical machine arises from three main sources: mechanical noise, aerodynamic noise, and electromagnetic noise. Mechanical noise originates from components such as bearings, gears, and other moving parts. Aerodynamic noise is primarily associated with the saliency of the machine and its ventilation system, both of which contribute to increased noise levels as the motor rotational speed increases. However, in modern electrical machines, electromagnetic noise is often the dominant contributor, especially at lower speeds with minimal aerodynamic noise. For these reasons, this work will focus exclusively on noise generated by electromagnetic sources.

Electromagnetic noise is characterized by the production of distinct frequency peaks that fall

within the most sensitive frequency range of the human ear (100 Hz to 15 kHz). These frequency components are perceived as particularly disturbing and contribute significantly to the overall acoustic discomfort. The electromagnetic noise produced by an electric machine is inherently related to the deformation of motor components, such as the stator core and rotor parts, under the influence of electromagnetic forces Vijayraghavan and Krishnan (1999).

Electromagnetic forces can be classified into three categories: Maxwell forces, Laplace (or Lorentz) forces, and magnetostrictive equivalent forces. Among these, Maxwell forces play a dominant role in generating electromagnetic noise. Magnetostrictive equivalent forces, which arise due to local changes in the mechanical properties of the material under the influence of a magnetic field, are often neglected in acoustic noise analysis. While their impact is not inherently negligible Mininger et al. (2007), they are typically ignored due to computational complexity. Laplace forces are also neglected, considering that the flux density in the stator windings is generally insufficient to induce significant vibrations that can propagate to the stator yoke.
Thus, in the context of electromagnetic noise in electric machines, Maxwell forces are regarded as the primary source of vibration and noise generation. This thesis focuses on analyzing these Maxwell forces, calculated using the virtual work method, as detailed in Section 2.3.4.3.

An important phenomenon to consider in vibration analysis is resonance. If the mode and frequency of the magnetic force wave coincide with the mode and natural frequency of the stator structure, a resonance condition will occur. Under such conditions, even a relatively small electromagnetic excitation force can induce substantial vibrations, leading to excessive noise and potentially accelerating wear and fatigue of machine components. Therefore, understanding and avoiding resonance conditions is crucial for optimizing the noise characteristics of electrical machines. To quantify the impact of electromagnetic forces, these forces are used as inputs for a mechanical FEA. This analysis is employed to determine the mechanical accelerations and deformations of the stator and other structural components. The electromagnetic forces computed from the electromagnetic FEA are then mapped onto the mechanical model of the stator, allowing for a comprehensive evaluation of the vibration behavior.

In the following subsections, the focus will be on detailing the various aspects of the vibroacoustic analysis of the stator, beginning with the introduction of the virtual work method for calculating Maxwell electromagnetic forces. We will then proceed to describe the dynamic mechanical model, followed by a discussion of modal analysis and the mode superposition

method. Together, these methods form a comprehensive framework for the vibration analysis of the stator, providing crucial insights into the underlying mechanisms of electromagnetic noise generation in synchronous reluctance machines.

4.1.1 Electromagnetic forces calculation

As mentioned above, while vibrations are present throughout the machine, the stator is the primary contributor to acoustic radiation. Therefore, we need to determine the magnetic forces distribution on each point of the stator boundary. Consequently, by applying the virtual work principle with equation 4.1, the local magnetic forces for each node k in $x - y$ directions are computed Bastos and Sadowski (2003) with the relation:

$$F_k = -\frac{1}{2}\nu \mathbf{A}^T \frac{\partial K}{\partial x}\mathbf{A} \tag{4.1}$$

These electromagnetic forces generated from the stator and rotor interaction have a tangential and a radial component. The tangential component generates the electromagnetic torque and the radial component acts as the main vibration source of the stator. Thus, in general, the tangential force is neglected for vibration analysis, as its effect on the structural response of the stator is much smaller compared to the dominant influence of radial forces Zou et al. (2024). With the forces in $x - y$ directions, the radial component $\mathbf{F}_r$ is obtained as:

$$\mathbf{F}_r(\theta, t) = \mathbf{F}_x(\theta, t)\cos\theta + \mathbf{F}_y(\theta, t)\sin\theta \tag{4.2}$$

Where $\mathbf{F}_x$ and $\mathbf{F}_y$ are the x and y component of the electromagnetic force, θ is the mechanical node angle and t is the time step. An example of the radial component of Maxwell forces for a single rotor position and over the whole stator is illustrated in Fig. 4.2.

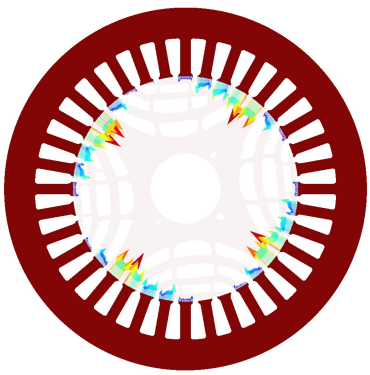

Figure 4.2: Radial force distribution for a static rotor position.

As the electric machine rotates, for the vibration response we need to compute the force distribution over a complete rotation of the rotor with fixed steps. This methodology gives a mapping of the magnetic forces. It is then possible to observe the radial forces distributions over the entire inner stator circumference (same position of Fig. 4.2) and a tooth node's force evolution as a function of rotor position, as shown in Fig. 4.3.

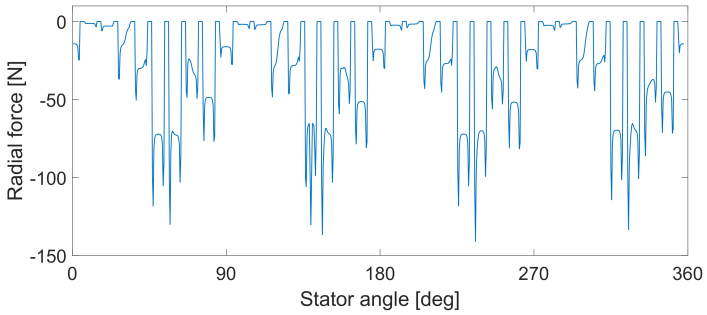

(a) Force distribution over the entire inner stator circumference.

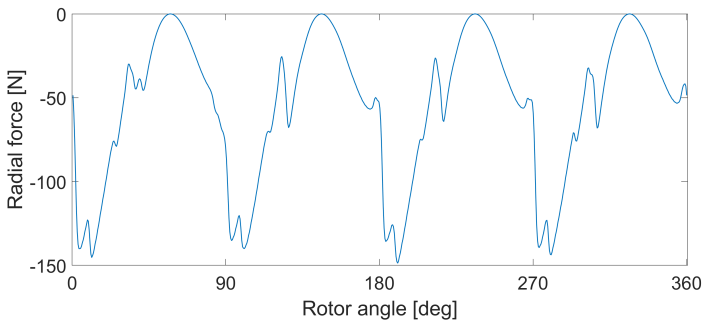

(b) Force evolution on a stator node for an entire rotation of the rotor.

Figure 4.3: Force distributions.

With the mapping of the forces it is possible to obtain a 2D-plane stator tooth surface of the radial force distribution, as represented in Fig. 4.4. With this representation is noticeable the effect of the 36 stator teeth on the stator angular position axis (also called spatial order). Looking at the rotation angle axis (also called time order) the effect of the 4 pole is visible. Additionally, a constant zone of low forces independent of the rotation angle, that can be attributed to the slot opening, is also observable.

With the 2D-plane forces distribution surface, the harmonic content of the magnetic force can be studied, both in terms of spatial harmonic and time harmonic. To do so, a 2-D Fast Fourier Transformation (FFT) can be done, as shown Fig. 4.5.

With this graphic it is possible to determine which harmonic can generate the resonances. For example the mode 0 can be excited by the 12th, 24th, and 36th harmonic. The mode 4 can

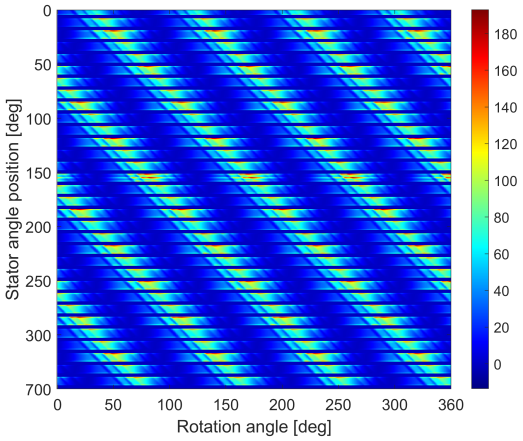

Figure 4.4: Radial force distribution for a static rotor position.

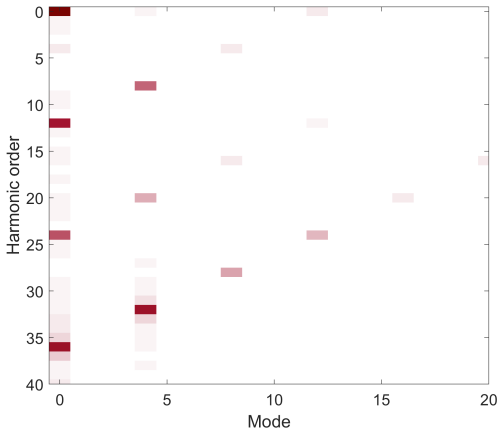

Figure 4.5: 2D FFT of the forces distribution.

be excited by the 8th, 20th, and 32th harmonic. The following modal analysis will clarify the relationship between the mode and harmonic order.

4.1.2 Dynamic mechanical model

The vibration response of the stator structure is governed by the system of equilibrium differential equations that represents the dynamic behavior. As a reminder, the equilibrium equation is expressed as:

$$M_s\ddot{\mathbf{u}}(t) + C_s\dot{\mathbf{u}}(t) + K_s\mathbf{u}(t) = \mathbf{F}(t) \tag{4.3}$$

where M_s is the mass matrix, C_s is the damping matrix, and K_s is the stiffness matrix. The vectors $\ddot{\mathbf{u}}$ and $\dot{\mathbf{u}}$ represent respectively the vector of nodal accelerations and the vector of nodal velocities, and $\mathbf{u}$ the vector of displacements. The force vector $\mathbf{F}(t)$ represents external forces applied to the structure, which can vary with time t. In this case, the vector $\mathbf{F}(t)$ correspond to the electromagnetic force $\mathbf{F}_r$ calculated with equation 2.35. Using complex notations, the vectors $\mathbf{u}(t)$, $\dot{\mathbf{u}}(t)$, $\ddot{\mathbf{u}}(t)$; and $\mathbf{F}(t)$ are time-dependent and can be expressed in harmonic form as:

$$\begin{aligned}
\mathbf{u}(t) &= \mathbf{u}\mathrm{e}^{j\omega t} \\
\dot{\mathbf{u}}(t) &= j\omega\mathbf{u}\mathrm{e}^{j\omega t} \\
\ddot{\mathbf{u}}(t) &= -\omega^2\mathbf{u}\mathrm{e}^{j\omega t} \\
\mathbf{F}(t) &= \mathbf{F}\mathrm{e}^{j\omega t}
\end{aligned} \tag{4.4}$$

To solve the system of equations, two main approaches can be employed: the direct method and the modal superposition method.

The direct method involves solving the matrix system directly, which can be computationally intensive. In contrast, the modal superposition method takes advantage of the results from modal analysis, where the problem is projected onto the modal basis obtained from the natural frequencies and mode shapes of the structure. In this approach, the overall solution is formed as a linear combination of the responses of each mode. This method is computationally more efficient, particularly for large systems, and is well-suited for our study given the assumptions of a linear structure and decoupled modes Bathe (1996).

The natural vibratory behavior of a mechanical structure is characterized by its eigenfrequencies and eigenmodes.

4.1.3 Modal analysis

Modal analysis is the most important step to be considered during the vibrational analysis for exploring the intrinsic structural properties of the system. The objective of the modal analysis is to determine the stator's natural frequencies (eigenfrequencies) and the corresponding modal shapes (eigenmodes), which are fundamental for predicting the resonance, evaluating the structural characteristics, and understanding the vibration behavior.

Modal analysis is performed under the assumption that the system is in free vibration, meaning there are no external forces acting on the structure. Another key assumption is that damping is negligible, allowing the eigenfrequencies to be treated as independent of any damping effect. This assumption is generally valid in the analysis of electrical machines, where damping is typically very low Zhao et al. (2020). Neglecting damping and excluding external loads, such as forces or displacements, the equation is then reduced to its associated homogeneous version:

$$M_s\ddot{\mathbf{u}}(t) + K_s\mathbf{u}(t) = 0 \tag{4.5}$$

The non-trivial solution of equation 4.5 provides the free vibration system. To solve this, we assume a particular type of solution in which all components of displacement depend on the same time function, such as $u(t) = \phi sin(\omega t)$, where ϕ represents the mode shape, and ω represents the natural angular frequency. Substituting this into the previous equation yields:

$$-\omega^2 M_s\phi(\omega) + K_s\phi(\omega) = 0 \tag{4.6}$$

This leads to a generalized eigenvalue problem. Non-trivial solutions exist only if the determinant of the system matrix is zero:

$$\text{det}[K_s - \omega_i^2 M_s] = 0 \tag{4.7}$$

Solving this eigenvalue problem provides both the natural frequencies and their corresponding eigenmodes.
With this approach, the modal analysis of the stator is conducted, yielding several natural vibration frequencies and the corresponding deformation patterns, as shown in Fig. 4.6.

The eigenmodes and their corresponding natural frequencies obtained from the modal analysis provide crucial insights into the potential vibration behavior of the electric motor. In electric machines, if the electromagnetic forces generated during operation align spatially with

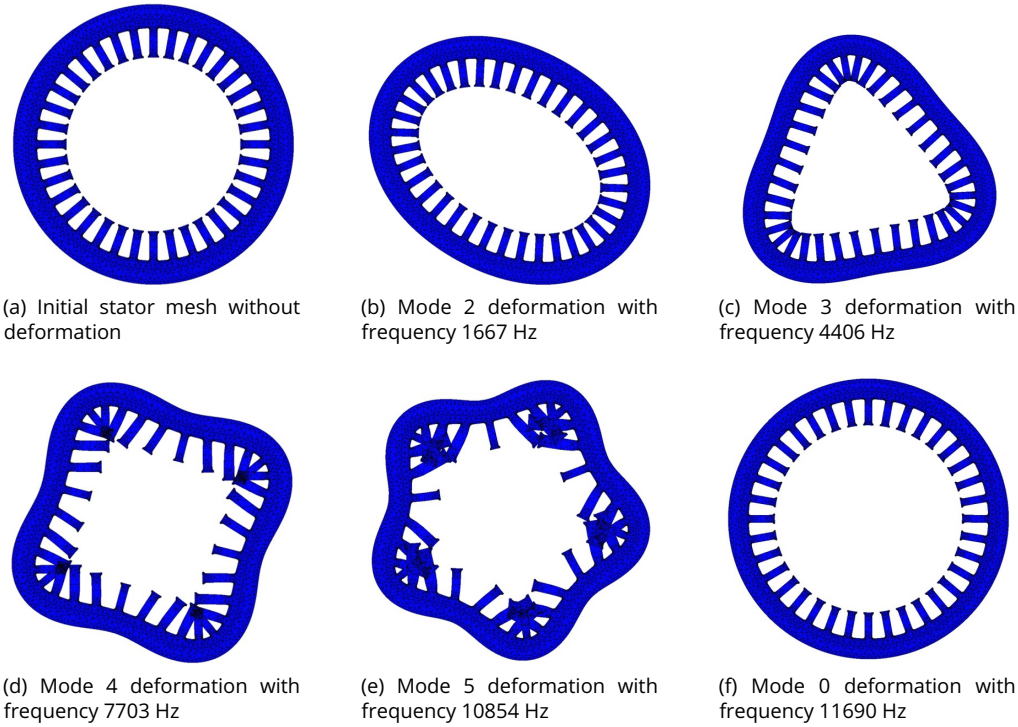

(a) Initial stator mesh without deformation

(b) Mode 2 deformation with frequency 1667 Hz

(c) Mode 3 deformation with frequency 4406 Hz

(d) Mode 4 deformation with frequency 7703 Hz

(e) Mode 5 deformation with frequency 10854 Hz

(f) Mode 0 deformation with frequency 11690 Hz

Figure 4.6: Modes shape of the stator with the associated natural frequencies.

one of these resonant modes, there is a strong likelihood that significant mechanical vibrations will be produced.

Modal analysis serves as the foundation for predicting the system's dynamic response under operational conditions. To evaluate how the electric machine will respond to time-varying forces, the mode superposition is employed. This method takes advantage of the natural modes obtained from the modal analysis to express the total response as a combination of individual mode shapes, each scaled according to the input forces.

4.1.4 Modal superposition method

Focusing now on the machine's vibratory behavior, the principle of modal superposition is useful for understanding the nature of its response to magnetic forces. The principle of modal superposition allows the behavior of a structure to be expressed in terms of its modal base, previously computed by modal analysis. Using this method, the vibration response can be approximated by a superposition of a small number of its first natural modes. The displacement and acceleration at a point on the structure can then be computed at low computational cost.

Consequently, the mode superposition method consists in expressing the displacement $u(t)$

presented in equation 4.3 as a linear combination of mode shapes (eigenvectors) weighted by time-dependent modal coordinates $q(t)$:

$$\mathbf{u}(t) = \mathbf{\Phi}\, q(t) \tag{4.8}$$

where $\mathbf{\Phi}$ is the modal matrix which is constructed with the eigenvectors ϕ_i from the solution of 4.6 and $q(t)$ is the vector of modal coordinates, which indicate how much each mode contributes to the total displacement at time t.
Using this expression in equation 4.3 and multiplying by $\mathbf{\Phi}^T$ yields to:

$$\mathbf{\Phi}^T M_s \mathbf{\Phi}\, \ddot{q}(t) + \mathbf{\Phi}^T C_s \mathbf{\Phi}\, \dot{q}(t) + \mathbf{\Phi}^T K_s \mathbf{\Phi}\, q(t) = \mathbf{\Phi}^T\, \mathbf{F}(t) \tag{4.9}$$

Using the orthogonality properties of the mode shapes Lengvarský and Bocko (2013), the matrices $\mathbf{\Phi}^T M_s \mathbf{\Phi}$ and $\mathbf{\Phi}^T K_s \mathbf{\Phi}$ become diagonal. This property significantly simplifies the problem, as it essentially decouples the coupled differential equations in the original physical coordinates. However, the damping matrix $\mathbf{\Phi}^T C_s \mathbf{\Phi}$ is generally not diagonal, which prevents full decoupling.

To address this, the damping matrix C_s is often assumed to be a linear combination of the mass and stiffness matrices, leading to a form of damping known as Rayleigh damping Hughes (2003). This assumption allows the diagonalization of the modal damping matrix, and it is expressed as:

$$C_s = \alpha M_s + \beta K_s \tag{4.10}$$

where α and β are the damping coefficients.
Using the properties of the mode shapes and applying the Rayleigh damping assumption, the resulting system of equations in the modal space becomes:

$$m_i\, \ddot{q}_i(t) + c_i\, \dot{q}_i(t) + k_i\, q_i(t) = f_i(t) \tag{4.11}$$

where m_i, c_i, and k_i are the elements of the diagonal matrices representing mass, damping, and stiffness for mode i, and $f_i(t)$ is the modal force corresponding to that mode. The system represents a set of n uncoupled second-order differential equations, where n is the number of modes considered. Each mode is now independent of the others, making the solution process significantly simpler and computationally efficient.

Once the modal coordinates $q_i(t)$ are determined for each mode solving 4.11, the physical displacement $u(t)$ can be reconstructed using equation 4.8. Similarly, the acceleration $\ddot{\mathbf{u}}(t)$ can

be obtained by differentiating the modal displacements. Thus, the physical displacement and acceleration are represented as a linear combination of the contributions from each mode.

With the structural dynamic model established and the computed electromagnetic force, the vibration response computations of the stator is evaluated by a FEA model implemented in Matlab. By integrating the electromagnetic-structural coupling process introduced earlier, the radial electromagnetic forces acting on the inner surface of the stator are used as excitation sources. These forces are coupled to the stator teeth for a harmonic response analysis in the frequency domain.

The electromagnetic forces are decomposed into a series of harmonics, and the mode superposition method enables a precise and computationally efficient way to predict and understand the stator response to these electromagnetic excitations.

4.1.5 Vibration analysis of the stator

The previously introduced structural dynamic model, which makes use of the modal superposition method, serves as the basis for the vibration analysis of the stator. The vibrational response is determined by applying the computed radial electromagnetic forces to the stator tooth surface, where these forces act as harmonic components distributed across each node on the surface. The vibration behavior of the stator is primarily influenced by its structural shape, material properties, and then natural frequencies.

Considering the relationship between electrical frequency and rotational speed, the frequency f_{kh} associated at each force harmonic k is computed according to:

$$f_{kh} = \frac{N}{60} * 2p * k \tag{4.12}$$

where k is the number of the harmonic order, N is the speed in rpm, and p is the number of pole pairs. At a specific speed case, these orders are meant to cross the structural modes at their corresponding frequency and thus induce an amplification of the acoustic noise due to resonance.

As shown in Fig. 4.5, the mode 4 could be excited by the 8th force harmonic. For instance, let us consider mode 4, which has a natural frequency of 7703 Hz. Using equation 4.12, we can determine the speed at which the 8th harmonic will resonate with mode 4. By setting $f_{kh} = 7703$ Hz and $k = 8$, we find a corresponding rotational speed of $N = 14437$ rpm.

With these information, we can perform the vibrational analysis of the stator geometry. First of all, a dynamic analysis is carried out with the 8th harmonic as excitation and the vibrational response of the stator geometry is analyzed. The result, shown in Fig.4.7, confirms what we deduced through the $2DFFT$ of the radial forces. The deformation shape generated by the 8th harmonic order of the forces is very close to the deformation obtained with the modal analysis, confirming that if the frequencies of mode and force harmonic coincide, a resonance occurs.

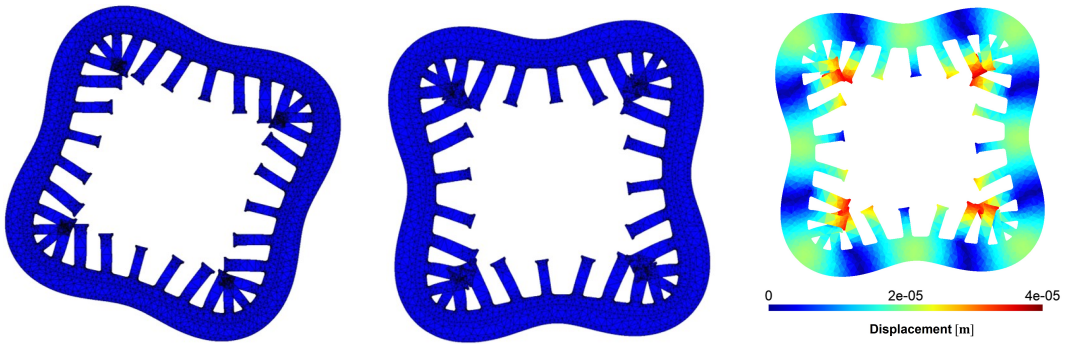

(a) Mode 4 deformation with frequency 7703 Hz.

(b) Deformation due to the 8th force harmonic.

(c) Displacements map with a multiplier coefficient of 500.

Figure 4.7: Comparison between the natural mode deformation and the 8th force harmonic deformation with the associated displacement values.

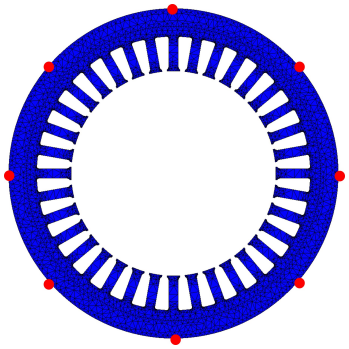

(a) Points (in red) used for the acceleration analysis.

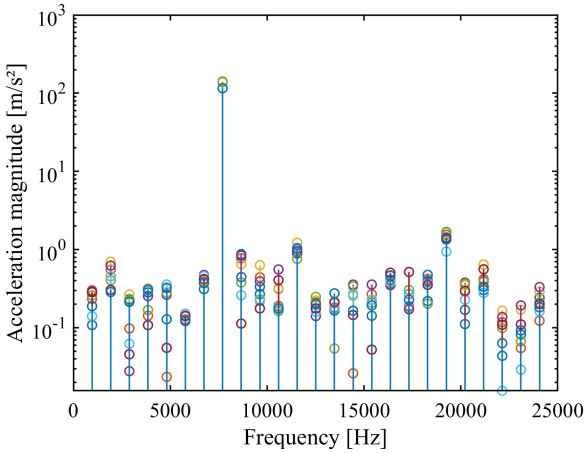

(b) Acceleration response at the selected points.

Figure 4.8: Location of the stator surface points selected for acceleration analysis and respective frequency spectrum of the acceleration response.

Furthermore, the resulting acceleration response is computed and analyzed on different top surface points of the stator as shown in Fig. 4.8a. The points are distributed on the external circumference at eight different positions. Fig. 4.8b shows the vibration acceleration distribution

of the outer stator surfaces at the rated speed. The resonance at 7703 Hz is evident, caused by the frequency of the corresponding harmonic being close to the intrinsic frequency of the stator.

These results suggest that mitigating resonance and reducing vibrations in the motor require careful optimization of the system design. The vibrations induced by electromagnetic forces have a significant impact, not only leading to increased acoustic noise but also degrading overall system performance and reliability. Thus, it is crucial to explore different methods to minimize these effects.

Various approaches have been investigated in the literature to reduce structural vibrations Król et al. (2023); Qin et al. (2020) . Common methods include current harmonic injection and geometry modifications introducing notches or changes to the stator teeth or rotor geometry. These changes can influence the distribution of forces and alter the modes susceptible to resonance.

However, modifying the geometry of the rotor and stator, which are key electromagnetic design factors, may have unintended effects on the motor's electromagnetic performance, potentially reducing torque output or impacting efficiency.

An alternative approach, explored in this thesis, is to modify the motor housing for vibration reduction. The motor housing serves as a thermal and structural design factor that could influences vibration characteristics without affecting electromagnetic performance and torque output. This makes the housing an ideal target for vibration mitigation efforts.

To optimize the motor housing effectively and reduce resonance at critical operating speeds, such as 14437 rpm, topology optimization is employed. This approach aims to identify the optimal shape and material distribution in the housing to minimize the impact of vibration at critical frequencies. However, it must be noted that altering the geometry of the motor (including both stator and housing) will inherently change the natural frequencies of the structure, potentially shifting them either higher or lower. The goal of the optimization process is to ensure that these natural frequencies do not coincide with the excitation frequencies encountered during normal motor operation.

Thus, topology optimization provides a powerful method for improving mechanical stability and reducing vibrations by focusing on the motor housing, effectively balancing performance and mitigating negative impacts on noise and reliability.

4.2 Topology optimization for vibration reduction

Topology optimization in the dynamics context addresses the design of structures that must operate under time-varying or oscillatory loads, as opposed to static conditions. This field has gained attention as it is highly applicable in real-world engineering environments where dynamic forces dominate, such as wind-induced loads on bridges, vibrations in machinery, or harmonic excitation in electrical motors. However, dynamic topology optimization is significantly less developed compared to static problems, largely due to the increased complexity of dealing with inertia and resonance.

The first notable work considering the dynamic behavior of structures in topology optimization was presented by Díaaz and Kikuchi (1992), focusing on natural frequency optimization. Earlier, in 1995, Ma et al. (1995) used an homogenization method to optimize structures under harmonic excitation, effectively reducing resonance effects. This was an early approach to addressing harmonic response problems using topology optimization. The concept of dynamic compliance, introduced by JOG (2002), further enhanced the dynamic optimization approach by offering a measure of the global response of a structure under dynamic loads. Many different works could be found in the literature since then Du and Olhoff (2007); Yang and Li (2013); Bai et al. (2023).

Dynamic topology optimization problems can generally be classified into two main categories Liu et al. (2015):

- **Eigenfrequency optimization**: this category involves maximizing specific eigenfrequencies or optimizing the gap between consecutive eigenfrequencies. Increasing the fundamental eigenfrequency or ensuring a wider separation between eigenfrequencies reduces the risk of resonance, which is particularly important for applications such as buildings, bridges, and automotive components.
- **Dynamic response optimization**: this category addresses minimizing the response of a structure under time-dependent loading. Here, dynamic compliance is a common objective, which aims to minimize the energy or deformation induced by external dynamic forces, thereby maximizing the structure's dynamic stiffness. For practical applications, methods have also been developed for reducing local dynamic responses, particularly at points of interest or subdomains within the structure, which is crucial for improving localized vibrational behavior in components.

The dynamic topology optimization have also been extended beyond traditional structural fields. For instance, it has been applied to piezoelectric devices, which face vibrational challenges similar to mechanical systems. In such devices, topology optimization methods are used to determine the optimal distribution of active and passive materials to achieve effective vibration control, enhancing both mechanical stability and energy efficiency Zhang and Kang (2013); Luo et al. (2009).

Electrical machines represent another area where dynamic topology optimization has been explored, albeit to a limited extent. Notably, there are only a few studies available in the literature. The first study came from 2002 by Yoo (2002), where the stator of a switched reluctance motor was optimized with the optimization problem formulated to minimize the frequency response and solved using the homogenization method. The objective function was formulated by the square of the mean compliance and only three static position of the rotor with the relative magnetic forces were analyzed and optimized, giving different optimal topologies according to the relative position (Fig. 4.9a). The proposed approach was more similar to the classical static problem but it provided the first insight for application to vibration reduction. The same author proposed in Yoo and Kikuchi (2002) a similar optimization for a stator tooth. In both papers, the stator topology exhibited empty parts, which negatively influenced performance. For this reason, the author proposed changing the material properties of some regions, which remains challenging even today with additive manufacturing.

Subsequently, over the past few years, two additional works have emerged that address vibration reduction in electric motors.

In Jang et al. (2021) topology optimization of the motor housing is applied to reduce vibration at a specific frequency, caused by electromagnetic force generated by a permanent magnet synchronous motor. The problem was formulated to minimize the acceleration magnitude at the selected frequency and was solved using the homogenization method. Acceleration was computed at a single node on the housing, with two different housing shapes used as starting points. Fig. 4.9b shows the results with the optimized housings. These results are promising, however, the algorithm used is not fully disclosed, and the homogenization method is employed instead of the simpler alternative. Furthermore, calculating the acceleration at a single point is not a recommended approach, as in some instances, it may represent a static fulcrum point where deformations are minimal and close to zero.

Another study, Sun et al. (2024), applied topology optimization to the rotor tooth design of a switched reluctance machine to reduce stator vibration caused by resonance, while retaining

the output torque as possible. The optimization was performed using the evolutional NGnet method and solved employing a genetic algorithm. The objective function was formulated to minimize the average displacement of the stator surface and maximize the average torque. The resulting rotor design was anchor-shaped with an inner hole, as shown in Fig. 4.9c, achieving the resonance-induced displacement reduced by 42% with a 5% average torque loss to the initial geometry.

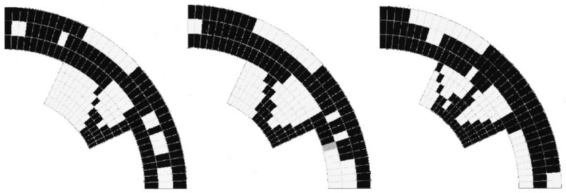

(a) Optimal rotor shapes at three different positions.

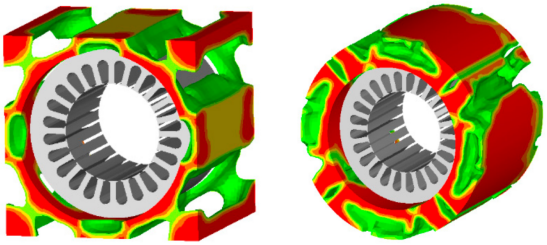

(b) Result of topology optimization for a square and circular housing.

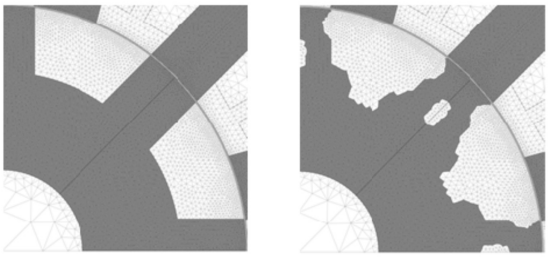

(c) Initial (left) and optimal (right) rotor design of a switched reluctance motor.

Figure 4.9: Examples of electrical machine topology optimization for vibration reduction in the literature.

In this thesis, the application of topology optimization for vibration reduction is inspired by the work of Jang et al. (2021). Adding an external housing to the stator of the electric machine and optimizing its design to reduce resonances based on vibration responses observed at critical rotational speeds.

In our work, the objective function is formulated using dynamic compliance for the combined stator and housing system. This formulation allows us to account for the global vibrational

behavior of the system rather than focusing on a specific point on the outer surface. Dynamic compliance is a widely considered objective function in such contexts, as minimizing it directly correlates with maximizing the structure's dynamic stiffness, thereby reducing the global response of the system to external forces.

To the best of our knowledge, this is the first time such a methodology, integrating dynamic compliance to reduce resonance in an electrical machine through external housing design, has been implemented. This makes the approach presented in this work a novel contribution to the field of topology optimization in electrical machine design.

4.3 Application to an electrical machine

This section presents the application of topology optimization to minimize the vibrational response of an electrical machine using the proposed method. The primary objective is to improve the vibrational behavior of the motor without altering its performance. The optimization targets the external housing design, specifically for rotational speeds where resonance is likely to occur, and aims to reduce the resonance-induced vibrations.

In this study, the active components of the motor, including rotor and stator, are assumed to be fixed. These parts have been optimized earlier in the coupled magneto-mechanical topology optimization, presented in the previous chapter. This separation ensures that structural changes in the housing do not interfere with the magnetic properties of the motor's active parts. The initial geometry configuration is illustrated in Fig.4.10.

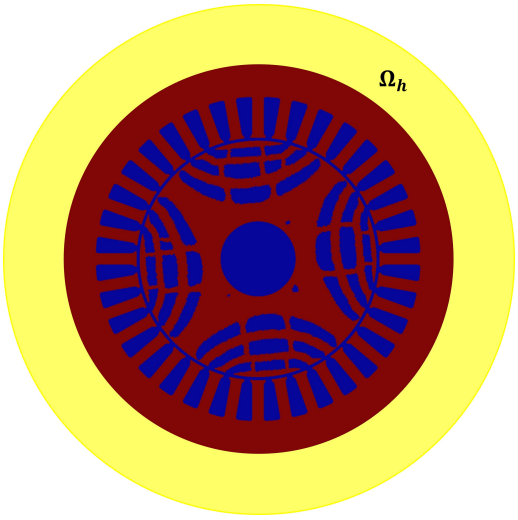

Figure 4.10: Initial configuration for the stator and housing yellow domain Ω_h.

The housing is represented by the yellow domain, defined by Ω_h, and the objective is to

refine the housing design to minimize the vibrations caused by specific electromagnetic forces frequencies. This leads to improved vibration control at predetermined resonance conditions while maintaining the motor's operational integrity. The optimization framework utilizes dynamic compliance as the objective function, which allows for a global consideration of the structural vibrational response rather than focusing on isolated points of interest. The overall aim is to minimize vibrations while also minimizing the material volume used for the external housing.

The problem formulation, as well as the detailed computational process, will be discussed in the following subsection.

4.3.1 Formulation of the optimization problem

In contrast to the established practice of compliance minimization in static topology optimization, a range of objective functions have been proposed in the literature to address the response of vibrating structures Niu et al. (2017). These include power flow, vibration transmission, and dynamic compliance, among others. In this work, dynamic compliance is chosen as it effectively captures the overall structural behavior under dynamic loading conditions.

The dynamic compliance is defined as $C_d = |\mathbf{F}^T\mathbf{u}|$, where the absolute value is used since the product may be negative when the load and the displacement are out of phase. Here, $\mathbf{F}$ denotes the vector of amplitudes of a given external time-harmonic electromagnetic force vector as $\mathbf{F}(t) = \mathbf{F}\mathrm{e}^{j\omega_i t}$, with ω_i the selected excitation harmonic frequency. For the case of static loading $\omega_i = 0$, the expression directly reduces to the traditional definition of static compliance seen in the previous chapter. Moreover, $\mathbf{u}$ is the vector of magnitudes of the corresponding structural displacement response vector $\mathbf{u}(t) = \mathbf{u}\mathrm{e}^{j\omega_i t}$ from the superposition method. Thus, $\mathbf{F}$ and $\mathbf{u}$ satisfy the dynamic equilibrium equation (4.3). In order to render the problem differentiable, the objective function is chosen as the square of the dynamic compliance C_d. The optimization problem is written as follows:

$$\begin{cases} \min\limits_{\rho\in\Omega_{\mathsf{h}}} & C_d^2(\rho) \\ \text{s.t.} & \dfrac{1}{V_{tot}}\displaystyle\sum_{e=1}^{N_{\mathsf{air}}}\rho_e\Delta_e \leq V_{\%} \\ & \rho_{\mathsf{min}} \leq \rho_e \leq 1 \end{cases} \tag{4.13}$$

The optimization domain Ω_{h} corresponds to the housing region. A maximum volume constraint $V_{\%}$ is considered to limit the amount of material in the housing. The square of C_d can be written as:

$$C_d^2 = (\mathbf{F}^T\mathbf{u})\overline{(\mathbf{F}^T\mathbf{u})} \tag{4.14}$$

Where the over-bar indicate the conjugate of a complex quantity as the load amplitude could be real or complex. The optimization problem is performed assuming that the frequency ω_i of the resonance harmonic i matches the natural frequency of the mode shape. Formulating the equilibrium equation in the frequency domain, and omitting the term $\mathrm{e}^{j\omega_i t}$ the equation (4.3) is written as:

$$(-\omega_i^2 M_s + j\omega_i C_s + K_s)\mathbf{u}(\omega_i) = \mathbf{F}(\omega_i) \tag{4.15}$$

From this, we can define the global dynamic stiffness matrix G_s as:

$$G_s = -\omega_i^2 M_s + j\omega_i C_s + K_s \tag{4.16}$$

The sensitivity of the objective function is defined as:

$$\frac{dC_d^2}{d\rho} = -2Re\left[\overline{\mathbf{F}^T\mathbf{u}}\left(\mathbf{u}^T\frac{\partial G_s}{\partial \rho}\mathbf{u}\right)\right] \tag{4.17}$$

where Re means the real part of the quantity. For the detailed development of the sensitivity see Niu et al. (2017).

The optimization procedure applied to solve the TO problem and design the stator housing is shown in Fig. 4.11.

Initially, for the given rotor geometry, the electromagnetic forces are computed giving the nodal forces mapping for the subsequent mode superposition in the dynamic analysis. After this, the natural frequencies of the stator are analyzed. Combining this result with the spatio-temporal characteristic obtained by the forces 2D-FFT, critical rotation speed where resonances occur are estimated, finding the frequency target ω to use for C_d computation.

Subsequently, the topology optimization step is started with the initialization of the design variables ρ for the housing domain. The SIMP method is employed to interpolate the material properties, such as stiffness and mass, based on the design variables ρ, as:

$$\begin{aligned} K_s(\rho) &= K_s^{(0)}(E_{min} + (E_{steel} - E_{min})\rho^{q_k}) \\ M_s(\rho) &= M_s\rho^{q_m} \\ C_s(\rho) &= \alpha M_s(\rho) + \beta K_s(\rho) \end{aligned} \tag{4.18}$$

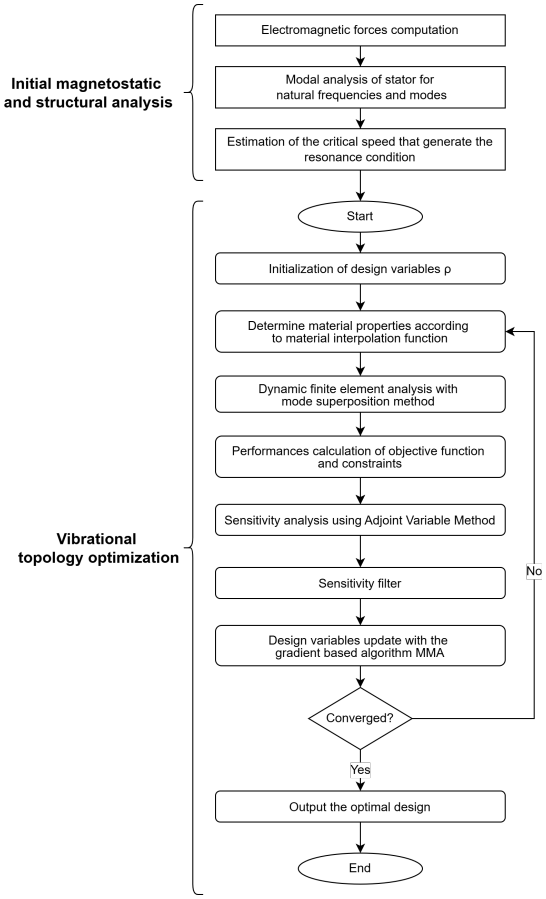

Figure 4.11: Flowchart of the proposed method, considering the electromagnetic force evaluation step.

where $K^{(0)}$ is the stiffness matrix constructed without considering the Young's modulus material properties, M_s is the solid material stiffness matrix, and the damping matrix $C_s(\rho)$ is constructed from the previously interpolated matrices. The penalty coefficients chosen are respectively $q_k = 3$ and $q_m = 6$, as discussed in Du and Olhoff (2007). The mechanical properties, as the Young's modulus and material density, are the same used for the static mechanical analysis. The mode superposition is employed to solve the dynamic problem and compute the displacements and accelerations. To solve the optimization problem, sensitivity analysis is performed to compute the gradient of the objective function with respect to the design variables ρ, computed by equation (4.17) using the adjoint variable method. A sensitivity filter is used, with a radius of 1.5 mm, to smooth the gradient field. Finally, MMA algorithm is employed to solve the optimization problem (4.13).

This methodology is applied and the results are presented in the following section.

4.4 Vibrational problem results

The optimization is performed on the circular housing with boundary conditions set to zero displacement at two points on the stator base, simulating a fixed attachment to a surface. These boundary constraints influence the natural modes and associated frequencies, necessitating adjustments to the rotational speed at resonance. While we could also consider the case without boundary conditions, it would be less realistic for practical applications. The housing is optimized to minimize dynamic compliance at a targeted frequency.

4.4.1 Configuration with boundary conditions

The configuration with boundary conditions, shown in Fig. 4.12, is analogous to a pure stator anchored at two points on the base, closely resembling to a real fixed support scenario. These boundary conditions alter the natural frequencies compared to the free or unsupported configuration.

The new natural frequencies are summarized in Table 4.1. With the specified boundary conditions, each mode is characterized by two distinct and disparate frequencies. Some of the specific mode shapes that correspond to these frequencies are illustrated in Fig. 4.13. The figures demonstrate how the modes are affected when boundary conditions are introduced, with a particular focus on mode 0.

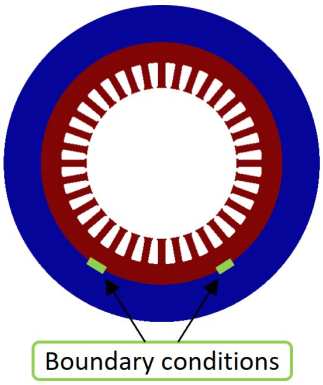

Figure 4.12: Zero displacement boundary conditions applied to the stator base (in green).

Table 4.1: Mode number and associated natural frequencies

Mode	Frequency [Hz]
0	9154
2	621 - 1587
3	3132 - 4848
4	6898 - 8691
5	11420 - 11560

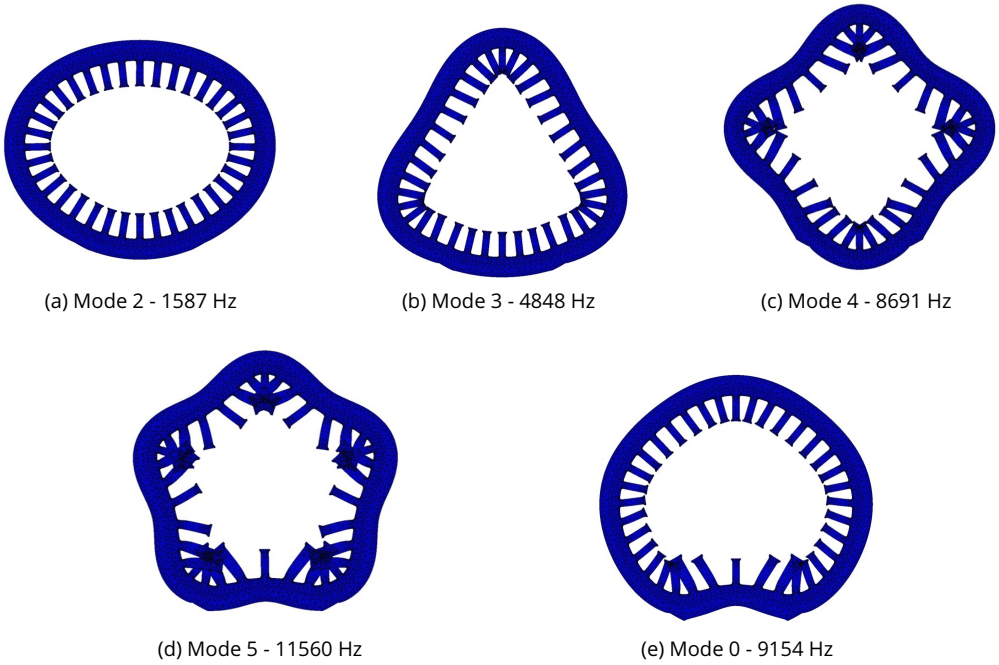

(a) Mode 2 - 1587 Hz (b) Mode 3 - 4848 Hz (c) Mode 4 - 8691 Hz

(d) Mode 5 - 11560 Hz (e) Mode 0 - 9154 Hz

Figure 4.13: Modes shape of the stator considering boundary conditions, and associated natural frequencies.

From these results, since the natural frequencies are changed, a new rotational speed will need to be computed to find the match between the 8th force harmonic and the natural frequency of mode 4. Among the two distinct frequencies, this study focuses on the one at 8691 Hz. The resulting speed is 16296 rpm, which is slightly higher than the previous speed of 14437 rpm. A vibrational analysis was then conducted to assess the impact of this new speed, examining the deformation generated by the 8th harmonic and the resulting displacements. The results confirmed the resonance, as illustrated in Fig. 4.14. The deformation generated by the force, visualized with a multiplier of 5000, matches perfectly with the mode 4.

The optimization process is initialized with a uniform distribution of the density variable design $\rho = \rho_{\text{min}}$. Initializing with ρ_{min} is essential to ensure the problem begins in a resonance condition, effectively simulating a scenario with no housing material. If the initialization is done with any value of ρ other than ρ_{min}, the resulting structure will exhibit shifted natural frequencies, which may lead to convergence issues during optimization. The maximum volume fraction constraint chosen for this problem is 20%, this value is used to see the effectiveness of the optimization (with high volume constraint it will fill the housing region, shifting the resonance).

The resulting housing design with the dynamic compliance evolution are shown in Fig. 4.15.

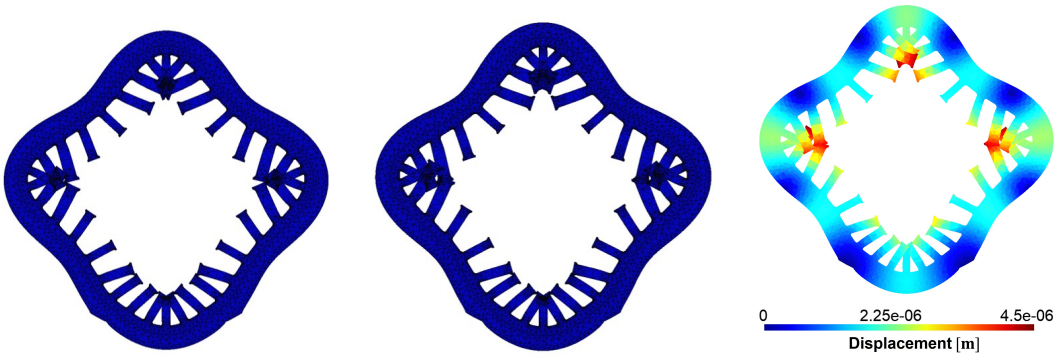

(a) Mode 4 deformation.

(b) Deformation by the 8th force harmonic with a multiplier coefficient of 5000.

(c) Displacements map with a multiplier coefficient of 5000.

Figure 4.14: Comparison between the natural mode deformation and the 8th force harmonic deformation with the associated displacement values.

The dynamic compliance value exhibits a pronounced decline during the initial 25 iterations, subsequently attaining a stable value after 371 iterations.

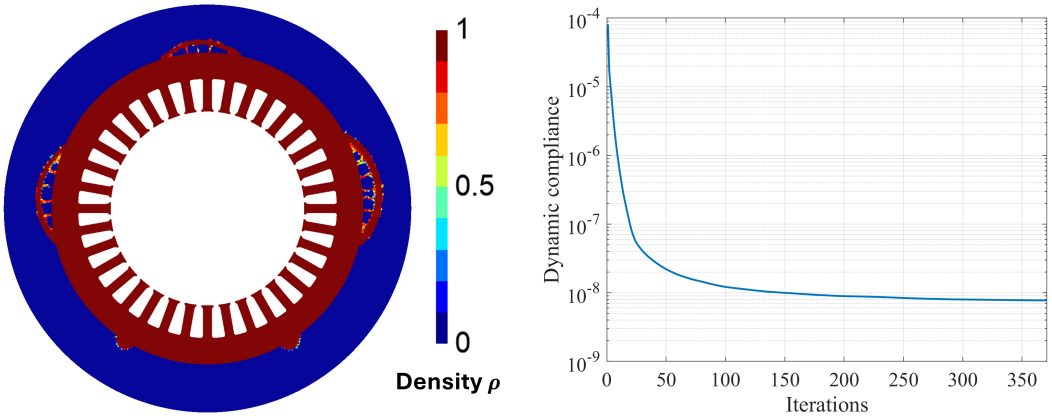

(a) Optimization result

(b) Dynamic compliance evolution

Figure 4.15: Resulting housing geometry (a) and convergence evolution dynamic compliance (b).

The optimization process added material primarily in three specific points of the geometry, where the deformation was most significant. Additionally, some material was distributed around the boundary conditions points. However, in the final material distribution, a few intermediate material remain, indicating areas where the optimization did not fully converge to a clear solid-void solution. This material distribution effectively strengthens the initial structure, which originally consisted of the pure stator. Fig. 4.16 shows the comparison between the initial and final deformation of the structure, generated only by the 8th force harmonic. As illustrated in Fig. 4.16b, the deformed structure demonstrates how the material in the housing region constrains

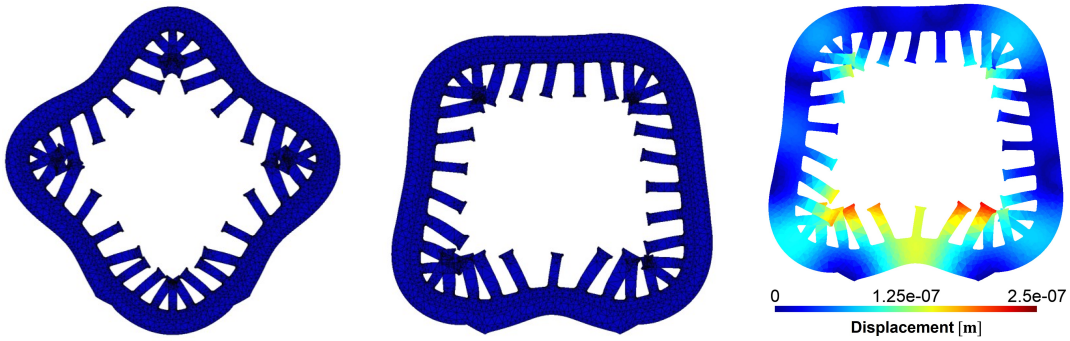

(a) Initial deformation with a multiplier coefficient of 5000.

(b) Final deformation with a multiplier coefficient of 100000.

(c) Final displacements map with a multiplier coefficient of 100000.

Figure 4.16: Comparison between initial and final structure deformation.

the deformations at the points where they were previously the most elevated. Furthermore, an examination of the maximum displacement (Fig. 4.16c) reveals that it has decreased by almost a factor of twenty.

The material, other to strengthening the rotor structure, modifies the initial natural frequencies. This result is expected: as the modal analysis strongly depends on the matrices K_s and M_s, the addition of material change the physical properties and thus the matrices. The evolution of the frequencies is shown in Fig. 4.17.

Not surprisingly, minimization of the dynamic compliance drives the design away from the resonance at 8691 Hz, yielding a structure whose eigenfrequencies are away from the excitation frequency of the electromagnetic force.

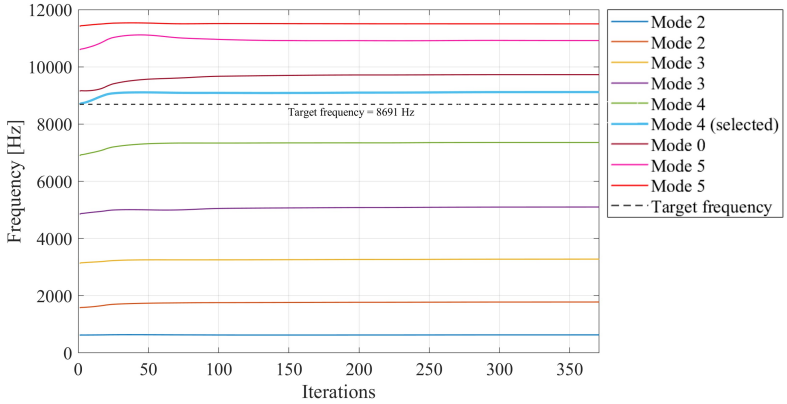

Figure 4.17: Eigenfrequencies evolution for the first five modes.

The results are resumed in Table 4.2 allowing the comparison of initial and final values.

Table 4.2: Comparison between initial and final geometry

	Initial geometry	Final geometry Fig. 4.15a
Dynamic compliance	7.97 $\times 10^{-5}$	7.73 $\times 10^{-9}$
Max displacement [m]	4.37 $\times 10^{-6}$	2.46 $\times 10^{-7}$
Mode 4 eigenfrequency [Hz]	8691	9119
Max acceleration amplitude [m/s²]	139	6

The acceleration magnitude is measured at eight points on the surface of the stator, and only the maximum value is considered in the analysis. As shown in Fig.4.18, the optimization process resulted in a significant decrease in the peak acceleration from 139 m/s² in the initial design to 6 m/s² in the optimized geometry. This substantial reduction highlights the effectiveness of the proposed method in mitigating vibrations caused by resonance. However, it is important to note that while the specific target acceleration is reduced, we observed some minor increases in acceleration at other frequencies.

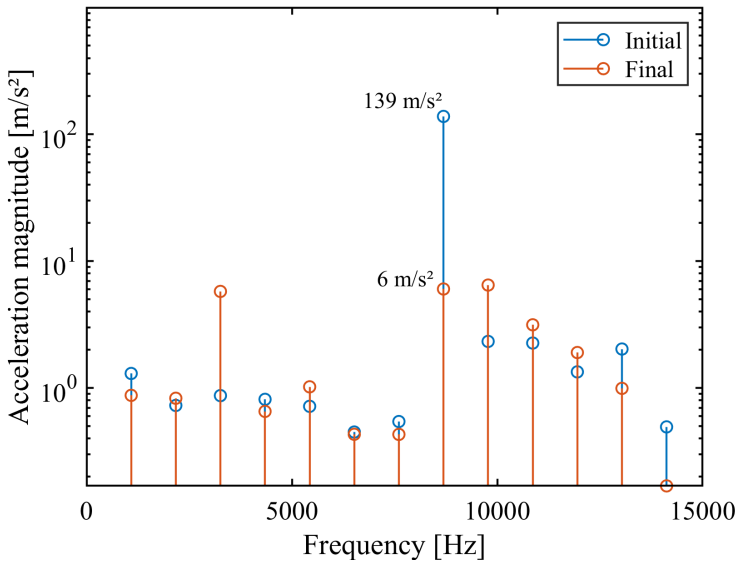

Figure 4.18: Acceleration response spectrum comparison of initial and final geometry.

4.5 Chapter conclusions

In this chapter, we proposed a topology optimization methodology for designing the housing of an electrical machine with the objective of reducing vibrations and mitigating resonance effects under specific operating conditions. The study began with an analysis of the origins of vibrations in electrical machines, focusing on the impact of electromagnetic forces and structural dynamics. A dynamic analysis was conducted to obtain the vibration response of the stator, identifying critical natural frequencies and rotational speeds where resonances occur.

To address the topology optimization problem, dynamic compliance was selected as the objective function due to its effectiveness in capturing the structural response under dynamic loading. The problem was formulated with a constraint on the material volume fraction and solved using the SIMP method combined with the MMA algorithm. The optimization process incorporated the rotor geometry, obtained from the previous chapter, and the corresponding electromagnetic forces. Using the mode superposition method, we identified that the 8th harmonic of the excitation force coincided with the natural frequency of mode 4 at 8691 Hz, leading to a critical rotational speed of 16296 rpm.

The optimization process successfully minimized dynamic compliance, reducing its value from 7.97 $\times 10^{-5}$ to 7.73 $\times 10^{-9}$, indicating a significant improvement in the structural response. Material redistribution within the housing led to a substantial reduction in vibrational effects, with the maximum displacement decreasing from 4.37 $\times 10^{-6}$ to 2.46 $\times 10^{-7}$ m. Similarly, the maximum acceleration amplitude, measured at critical points, dropped from 139 m/s² to just 6 m/s², demonstrating the optimization's effectiveness in mitigating resonance-induced vibrations. Furthermore, the optimized structure exhibited a shift in the natural frequency of mode 4, increasing from 8691 Hz to 9119 Hz, effectively moving it away from the excitation frequency and further reducing resonance effects.

In conclusion, the proposed topology optimization approach successfully addressed the vibrational challenges of the stator housing by significantly reducing dynamic compliance, displacements, and acceleration amplitudes while shifting natural frequencies to avoid resonance. These results confirm the effectiveness of dynamic compliance minimization in enhancing the stability and performance of structures subjected to dynamic loading. The study highlights the potential of this approach for improving the vibrational behavior of electrical machine components, contributing to more robust and reliable designs.

Conclusions and perspectives

Summary and contributions

In this thesis, we focused on advancing topology optimization techniques specifically for the design and optimization of electrical machines. The proposed methodology relies on the density-based approach, more specifically the SIMP method. Our research addressed multi-physics challenges and extended the applications of TO to include vibrational analysis. The primary objectives of our work included establishing a comprehensive methodology for magnetic and mechanical TO, applying and comparing multiple optimization strategies such as two-step and simultaneous optimization using different algorithms, proposing a novel objective function formulation, and introducing vibration reduction through TO.

The detailed synthesis and contributions of this thesis are summarized as follows:

- **Methodology development, Chapter 2**

  A methodology for applying topology optimization to electrical machines was developed, considering SIMP method. This chapter provides a comprehensive flowchart detailing the key steps, formulations, and computational processes, offering a clear framework for comprehension and further replication and application. The inclusion of material interpolation strategies, sensitivity analysis, and regularization techniques gives the tools for tackling the magneto-mechanical multi-physics problem.

- **Rotor optimization for synchronous reluctance machines, Chapter 3**

  - **Novel problem formulation**: A new objective function was introduced to optimize the average torque of a synchronous reluctance machine. Unlike the traditional average torque formulation, which requires multiple FEAs, the proposed method based on the energy difference between the d-axis and q-axis necessitates only two FEAs, significantly reducing computational cost. Numerical results show that, for a typical magnetostatic optimization, the computation time with the conventional average torque formulation is approximately

one day, whereas with the energy difference formulation it is reduced to around three hours. Beyond the notable gain in computational efficiency, the proposed approach also maintained a comparable torque performance. Although the mean torque achieved with the energy difference formulation was slightly lower (by approximately 4–10%) compared to the conventional method, it offered a valuable compromise between torque performance and computational efficiency, making it particularly suitable for extensive optimization processes.

- **Algorithm comparison**: The analysis includes an investigation of the Generalized Optimality Criteria (GOC) algorithm, comparing its performance with the widely used Method of Moving Asymptotes (MMA). By employing and comparing two optimization algorithms in the context of multi-physics topology optimization (TO) problems, this work contributes to a better understanding of algorithmic behavior under complex coupled conditions.

The comparison was conducted across different problem initializations, revealing that the choice of initial material distribution strongly influenced the final optimized topology. Different initializations often led to distinct final geometries and, consequently, different performance levels.

Under the same conditions, both GOC and MMA produced comparable results in single-physics optimizations. However, with MMA tending to generate additional flux paths that offered slightly increased magnetic performance. Significant differences emerged in coupled multi-physics problems, where only the MMA algorithm proved capable of optimizing simultaneously conflicting magnetic and mechanical objectives, while GOC, despite testing several problem formulations, was unable to deliver satisfactory results. These findings highlight the importance of selecting the optimization algorithm according to the complexity and the multi-physical nature of the problem.

- **Multi-physical optimization and numerical validation**: This thesis addresses the challenges of coupling electromagnetic and mechanical performance metrics in a single optimization framework, providing insights into the interaction between these physical domains. Various problem formulations are validated numerically, taking into account different problem initializations. One specific initialization method is highlighted for its effectiveness in creating multiple magnetic flux barriers.

The multi-physic optimization was conducted using two different strategies: a two-step sequential approach, where the physics are optimized separately, and a simultaneous integrated approach, where both physics are treated within a single optimization problem. Regularization techniques were employed to support the optimization process. A periodic

density filter was applied during the magnetostatic optimization to promote smooth material distributions, while an adapted filter was used in the mechanical phase to facilitate the formation of structural elements such as mechanical bridges. Additionally, Heaviside projection was used during post-processing to sharpen the material boundaries and obtain clear solid-void designs.

In the two-step approach, the mechanical optimization was applied after the magnetic optimization, allowing targeted refinement of mechanical properties such as compliance and Von-Mises stress through control of the mechanical volume fraction. The magnetic geometry remained unchanged during the mechanical phase, sometimes resulting in asymmetric designs. In contrast, the simultaneous optimization approach integrated both physics in the same problem, seeking a material distribution that balanced electromagnetic and mechanical properties. Although it did not achieve the absolute highest torque values compared to the two-step method, it maintained relatively low compliance across a range of torque outputs and produced more symmetric and mechanically robust designs with lower values of compliance. Finally, the two approaches were compared, revealing complementary benefits depending on design priorities. Results demonstrated that the two-step method can achieve higher torque at the cost of mechanical compliance, making it better suited for applications prioritizing maximum torque output at the expense of mechanical robustness. Conversely, the simultaneous approach provides a more balanced and stable design, yielding more mechanically stable designs for a given range of torque outputs, ideal for applications where mechanical reliability and reduced deformation are critical.

- **TO extension to vibration reduction, Chapter 4**

  In this last chapter, the topology optimization framework was extended to address vibration reduction caused by harmonic magnetic forces in electric machines. Starting from one of the improved rotor designs developed in Chapter 3, an external housing structure was added and included in the optimization. The goal was to mitigate resonances induced by specific harmonics of the electromagnetic forces, particularly at operating speeds where the excitation frequencies aligned with the structure natural modes. A material distribution optimization was performed on the housing, aiming to shift its eigenfrequencies away from the dominant excitation harmonics and to reduce vibration amplitudes. Numerical results confirmed the effectiveness of this approach, showing a significant reduction in vibrational responses at critical harmonics. The housing optimization successfully suppressed resonance peaks without altering the magnetic performance of the motor. This

work introduces an innovative vibration control strategy based on optimizing the passive mechanical response of the motor structure, offering a practical solution to enhance noise and vibration performance in electric machines.

Perspectives

We believe that this thesis work opens several future research directions, many of which emerged during and after the completion of this work. These perspectives represent opportunities to expand the scope and impact of topology optimization in the design of electrical machines. Key areas for further exploration are detailed below:

1. **Reduction of torque ripple using magnetic energy formulation**

   In this thesis, the average torque of synchronous reluctance machines was maximized using a novel problem formulation based on the energy difference between the d- and q-axes. A promising direction for future research would involve extending this formulation to simultaneously address torque ripple minimization. Torque ripple is a critical design factor, directly influencing the motor operation and its noise characteristics. Developing a new energy-based formulation that incorporates ripple reduction could eliminate the need for extensive rotor position evaluations while achieving both objectives (high average torque and low ripple) in a computationally efficient manner.

2. **Multi-objective optimization and expanded problem formulations**

   This thesis focused primarily on optimizing average torque while ensuring mechanical robustness. A natural extension would involve developing multi-objective formulations that simultaneously consider multiple magnetic and mechanical performance metrics, such as torque ripple, iron losses, current density, and optimal current angle. Incorporating these additional objectives would enable a more comprehensive optimization process, leading to designs that are better balanced across different performance criteria.

3. **Vibration reduction across multiple operating points**

   In this work, vibration reduction was targeted by optimizing the external housing for specific resonances under fixed operating conditions. A key future direction would be to extend this approach to consider multiple working points and speeds, reflecting real-world operating conditions of electric machines. Additionally, optimizing active components such as the rotor and stator for vibrational behavior could further enhance noise reduction and structural stability, offering a deeper integration between magnetic, mechanical, and vibrational performance.

4. **Prototyping and experimental validation via additive manufacturing**

   To bridge the gap between computational results and practical application, fabricating a prototype based on topology-optimized designs using 3D printing techniques represents

an important next step. Experimental validation through test-bench analysis would allow for performance assessment under real operating conditions, providing valuable feedback for further refinement of the optimization methodologies and confirming the feasibility of the proposed designs.

Synthèse en Français

L'Union Européenne (UE) s'est engagée à réduire progressivement sa dépendance aux combustibles fossiles, avec pour objectif la neutralité carbone d'ici 2050 Khaleel et al. (2024).Cette initiative nécessite des avancées significatives dans les technologies de conversion d'énergie, notamment les dispositifs de conversion électromécanique, essentiels pour les systèmes d'énergie renouvelable et la mobilité électrique. Les machines électriques remplacent progressivement les moteurs à combustion et les actionneurs hydrauliques dans divers domaines. L'émergence des voitures électriques, l'électrification des réseaux ferroviaires, ainsi que des systèmes embarqués dans l'aviation, en sont quelques exemples marquants. Cependant, l'utilisation croissante de ces machines pose des défis de conception et d'optimisation, notamment en termes d'efficacité, de bruit et d'interférences électromagnétiques, tout en réduisant leur impact environnemental Bianchi et al. (2021).

Cette thèse s'inscrit dans ce cadre actuel de transition énergétique et s'intéresse à l'application de l'optimisation topologique pour la conception des machines électriques. Le but principal est de développer des approches innovantes pour résoudre des problèmes complexes et multi-physiques liés à l'optimisation des moteurs synchrones à réluctance. En tenant compte des performances magnétiques, mécaniques et vibratoires, l'objectif est d'explorer de nouvelles conceptions et de dépasser les limites des méthodes d'optimisation traditionnelles.

La première partie de cette thèse présentera le contexte et les différentes techniques d'optimisation actuellement appliquées aux machines électriques. La conception des machines électriques se décompose en deux phases principales : la conception initiale et l'optimisation. La phase de conception initiale vise à trouver une configuration réalisable en fonction des exigences de l'application, tandis que la phase d'optimisation améliore les performances de la machine en ajustant le design initial FONTCHASTAGNER and MESSINE (2023).

Trois stratégies principales peuvent être employées pour optimiser la structure d'un dispositif : l'optimisation paramétrique, l'optimisation de forme et l'optimisation topologique. L'optimisation

paramétrique ajuste les dimensions des composants existants, l'optimisation de forme modifie les contours, et l'optimisation topologique se concentre sur la distribution du matériau dans une zone définie. Chacune de ces techniques présente des avantages et des inconvénients. Une analyse approfondie de l'application de ces trois techniques sera menée, en se concentrant particulièrement sur l'optimisation du rotor des machines électriques. Cette analyse portera sur deux types de machines : les moteurs synchrones à réluctance (SynRM) et les moteurs synchrones à aimants permanents (PMSM). La Fig. 4.19 présente des exemples illustrant l'application des trois types d'optimisation.

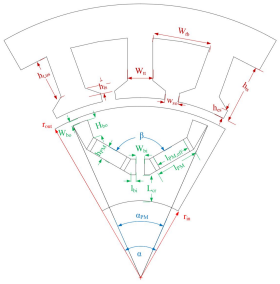

(a) Variables géométriques d'optimisation pour un PMSM Darmani et al. (2024).

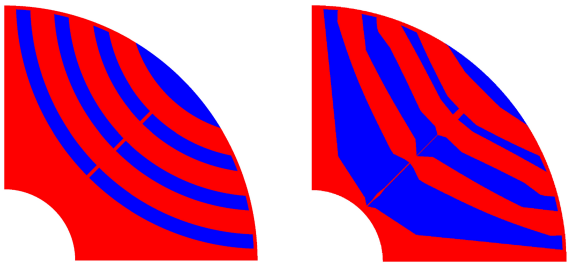

(b) Optimisation de forme d'un SynRM : géométrie initiale (à gauche) et géométrie optimisée (à droite) Brun et al. (2023).

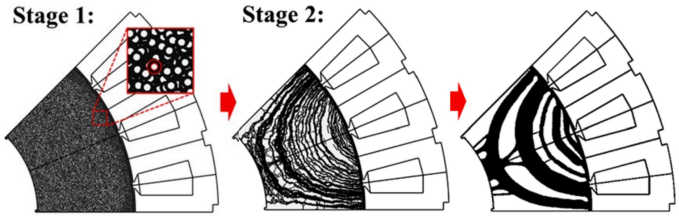

(c) Optimisation topologique du SynRM : géométrie initiale (à gauche), géométrie optimisée magnétiquement (au centre) et géométrie optimisée magnéto-mécaniquement (à droite). Lee and Jang (2023b).

Figure 4.19: Exemples tirés de la littérature des differentes techniques pour l'optimisation paramétrique des machines electriques.

L'optimisation topologique, comme on peut constater dans la figure, se distingue des autres techniques d'optimisation par sa capacité à explorer un éventail plus vaste de solutions de conception. Elle permet de générer des configurations innovantes qui repoussent les limites des approches traditionnelles, bien qu'elle exige une complexité numérique plus élevée.

Introduite à la fin des années 1980 par les travaux fondateurs de Bendsøe and Kikuchi Bendsøe and Kikuchi (1988), cette méthode d'abord utilisée dans le cadre de la mécanique des structures a progressivement gagné en popularité dans divers domaines physiques. Ces dernières années, son développement a été accéléré par les avancées en fabrication additive, rendant possible la concrétisation de structures complexes conçues grâce à cette approche Tiismus et al. (2022b).

Appliquée aux machines électriques, elle permet d'optimiser la répartition des matériaux tels que l'air, le fer, les conducteurs, et les aimants, tout en contournant les limitations des méthodes classiques. Contrairement à ces dernières, l'optimisation topologique ne nécessite ni paramétrisation préalable, ni définition géométrique initiale stricte, offrant ainsi une flexibilité unique.

L'objectif principal de l'optimisation topologique est de déterminer la distribution optimale du matériau dans un domaine donné, en tenant compte des contraintes et des objectifs de performance. Elle repose sur plusieurs méthodologies. Les plus utilisées sont : ON-OFF, les approches à densité, et les méthodes de lignes de niveau Lucchini et al. (2022). Ces outils ont été appliqués avec succès à la conception de machines électriques Nishanth and Wang (2022). Nous proposons également une revue de ces méthodologies appliquées aux machines électriques, en mettant en avant leur pertinence et leur potentiel pour relever les défis de conception actuels.

Le **Chapitre 2** introduit en détail la méthodologie utilisée pour appliquer l'optimisation topologique dans la conception des machines électriques, en mettant particulièrement l'accent sur les formulations magnéto-statiques et mécaniques. L'objectif est de détailler chaque aspect et de fournir tous les outils nécessaires à la compréhension et à la reproduction de cette méthodologie. Pour cela, la présentation se fait sous la forme d'un diagramme en blocs, avec des explications détaillées de chaque composante.

L'optimisation topologique repose sur plusieurs étapes fondamentales. Tout d'abord, une formulation claire du problème d'optimisation, spécifiant les objectifs de performance (comme le couple électromagnetique ou la rigidité mécanique) et les contraintes à respecter (telles que le volume de matériau, les limites mécaniques ou magnétiques). Cette formulation est suivie d'un processus de calcul comprenant la modélisation aux éléments finis, la répartition de matière dans le domaine d'optimisation avec les propriétés physiques définies par l'interpolation des matériaux, l'analyse de sensibilité et l'optimisation proprement dite.

Cette section intègre deux modèles physiques principaux et leurs formulations respectives aux éléments finis :

- **Modèle magnétostatique**: Il décrit le comportement électromagnétique du système, en utilisant des formulations basées sur l'énergie magnétique et le couple électromagnétique. Les propriétés des matériaux, la formulation par éléments finis et les quantités d'intérêt comme la différence d'énergie entre les axes d et q sont détaillées.

- **Modèle mécanique**: Ce modèle analyse la rigidité et la résistance structurelle de la géométrie optimisée, en tenant compte des propriétés mécaniques comme le module de Young et les contraintes de Von Mises.

L'interpolation des matériaux est réalisée à l'aide de la méthode à densité SIMP (Solid Isotropic Material with Penalization), qui permet de moduler les propriétés des matériaux en fonction d'une densité continue entre 0 (matériau absent) et 1 (matériau plein). Cette approche simplifie la transition entre les zones de matériau et de vide avec une fonction interpolante et un facteur de pénalisation qui peut être adapté selon le problème. La Fig. 4.20 illustre un exemple de cette approche.

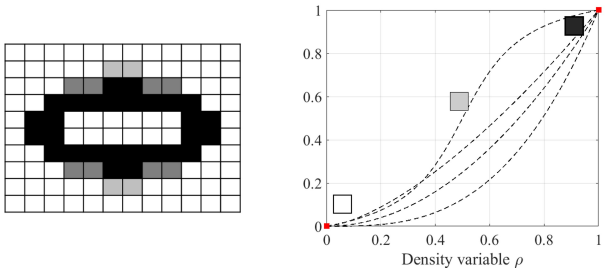

Figure 4.20: Illustrations de la distribution des matériaux (à gauche) et des différentes fonctions d'interpolation (à droite).

Sur la gauche, un domaine rectangulaire est discrétisé en un ensemble d'éléments finis (ici, des carrés). Chaque élément se voit attribuer une densité ρ. La partie droite de la figure présente différentes fonctions d'interpolation possibles reliant la variable de densité ρ à la propriété effective du matériau. Ces courbes démontrent comment la propriété matérielle évolue en fonction de la densité, mettant en évidence l'impact potentiel du choix de la fonction et du facteur de pénalisation sur le comportement de l'optimisation.

En simplifiant la transition entre les zones de matériau et de vide grâce à cette approche continue et pénalisée, la méthode SIMP permet d'utiliser des algorithmes d'optimisation efficaces basés sur les gradients pour déterminer la distribution optimale de matériau. Cependant, l'application de ces méthodes basées sur le gradient exige le calcul des dérivées de la fonction objective et des contraintes par rapport à des milliers de variables de conception. Une approche classique par différences finies pour calculer ces gradients serait prohibitivement coûteuse. C'est pourquoi cette thèse adopte la méthode de l'adjoint Cea (1986), une approche reconnue pour son efficacité dans le calcul rapide des gradients globaux, indépendamment du nombre de variables de conception.

Pour garantir la convergence et la robustesse des solutions obtenues, des techniques de

régularisation sont utilisées, telles que les filtres basés sur la densité ou la projection de Heaviside Sigmund and Petersson (1998). Ces techniques réduisent les dépendances au maillage et améliorent la qualité des solutions en éliminant les zones de densité intermédiaire et l'apparition des artefacts de type damier (checkerboard).

Dans cette thèse, deux algorithmes différents seront utilisés : la méthode des asymptotes mobiles (Method of Moving Asymptote, MMA) Svanberg (1987) et le Generalized Optimality Criteria (GOC) Kim et al. (2021). Le premier, bien connu et très souvent utilisé dans plusieurs domaines de l'optimisation topologique. Le deuxième, plus récemment proposé, repose sur l'amélioraton d'un algorithme plus connu Optimality Criteria (OC) Bendsøe (1995).

Le chapitre présente un exemple concret d'optimisation appliquée à une inductance, illustrant l'efficacité de la méthode pour résoudre des problèmes pratiques.

Dans le **Chapitre 3**, la méthodologie précédemment présentée sera utilisée pour l'optimisation topologique magnéto-mécanique appliquée à la conception du rotor d'un moteur synchrone à réluctance. Dans ce moteur, la géométrie du stator est imposé, ainsi que le bobinage et le nombre de pôles. La Fig. 4.21 présente la géometrie de la machine étudiée.

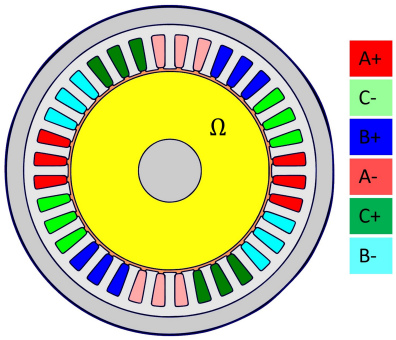

Figure 4.21: Géométrie de la machine avec la configuration de distribution des enroulements utilisée et l'espace de conception du rotor jaune Ω où l'optimisation topologique est appliquée.

La méthodologie introduite dans le chapitre précédent est appliquée pour cela. En complément des deux algorithmes utilisés, trois initialisations différentes du problème d'optimisation sont également testées (distribution de matière homogène, distribution de trous dans le domaine et distribution arrangée de trous suivant les axes $d-q$). Cette approche permet d'explorer diverses configurations et de mieux comprendre l'influence des choix initiaux sur les performances et la convergence de la solution finale, offrant ainsi une analyse plus complète et nuancée.

Dans un premier temps, l'optimisation magnétique est abordée à travers deux formulations

distinctes, ayant pour objectif de maximiser le couple moyen du moteur. Cette étape permet notamment de comparer une nouvelle fonction objective, proposée dans ce travail de these, basée sur l'énergie magnétique.

- **Maximisation du couple moyen** : Cette approche repose sur une méthode traditionnelle où l'objectif est d'optimiser la moyenne des valeurs instantanées du couple, calculées pour différentes positions du rotor. Plus le nombre de positions N considérées est élevé, plus le calcul sera précis, bien que cela se fasse au détriment d'un temps de calcul accru.
- **Maximisation de la différence d'énergie magnétique** : Cette nouvelle formulation propose de maximiser la différence d'énergie magnétique entre les axes d et q. En conditions linéaires, les inductances des deux axes peuvent être calculées en fonction des énergies magnétiques respectives et des courants. Cette approche permet de réduire le temps de calcul tout en offrant des performances de couple comparables à la méthode traditionnelle.

Les résultats numériques montrent que, pour une optimisation magnétostatique typique, le temps de calcul avec la formulation conventionnelle du couple moyen est d'environ une journée, tandis qu'avec la formulation basée sur la différence d'énergie, il est réduit à environ trois heures. Cette amélioration s'explique notamment par le fait que la méthode basée sur l'énergie ne nécessite que deux analyses par éléments finis (FEA) par itération, contre 45 utilisées pour la méthode classique. Au-delà du gain notable en efficacité de calcul, l'approche proposée permet de maintenir des performances de couple comparables. Bien que le couple moyen obtenu avec la formulation par différence d'énergie soit légèrement inférieur d'environ 4 à 10 $\%$ par rapport à la méthode conventionnelle (voir tableau 4.3), cette approche représente un compromis intéressant entre performance et efficacité de calcul, la rendant particulièrement adaptée aux processus d'optimisation de grande envergure.

Table 4.3: Comparaison du couple moyen entre les deux formulations de problème

Initialisation	Algorithme	Couple moyen [N.m] pour le problème d'optimisation du couple moyenne	Couple moyen [N.m] pour le problème d'optimisation de la différence d'énergie
Homogène	GOC	6.74	6.45
Homogène	MMA	6.82	6.51
Trous	GOC	7.18	6.47
Trous	MMA	7.30	6.53
Trous d–q	GOC	7.01	6.50
Trous d–q	MMA	7.07	6.55

La seconde partie du chapitre est consacrée à l'optimisation multiphysique du rotor, avec

l'optimisation magnéto-mécanique. Cette optimisation est appliquée selon deux méthodologies différentes :

- **Approche en deux étapes** : Cette méthode consiste à optimiser d'abord les performances magnétiques, puis à améliorer la robustesse mécanique en ajoutant des ponts mécaniques dans les zones d'air du rotor. Les résultats, résumés dans les quatre premières lignes du tableau 4.4, montrent que cette approche permet de réduire la compliance (une mesure de la rigidité mécanique) et les déplacements maximaux, mais au détriment des performances magnétiques. En effet, l'ajout de ponts mécaniques perturbe les chemins de flux magnétique, réduisant ainsi le couple moyen.

- **Optimisation simultanée** : Cette méthode équilibre les performances magnétiques et mécaniques pendant tout le processus d'optimisation. La formulation du problème consiste à minimiser la compliance tout en imposant une contrainte sur la différence d'énergie magnétique. Les résultats, présentés dans la dernière ligne du tableau 4.4, montrent que cette approche offre des conceptions équilibrées, avec des performances mécaniques et magnétiques satisfaisantes.

Table 4.4: Résumé des performances mécaniques et magnétiques avant et après optimisation mécanique

Géométrie initiale	C [J]	u_{max} [mm]	σ_{max} [MPa]	T_{avg} [N.m] mag.	T_{avg} [N.m] mag.+méc.
GOC homogène	0.52	0.0048	37	6.45	5.76 (-10.7%)
GOC trous d–q	0.98	0.0061	55	6.50	5.63 (-13.4%)
MMA trous	0.75	0.0064	40	6.53	6.04 (-7.5%)
MMA trous d–q	1.22	0.0113	65	6.55	5.90 (-9.9%)
Optim. simultanée	0.57	0.0103	57	—	5.85

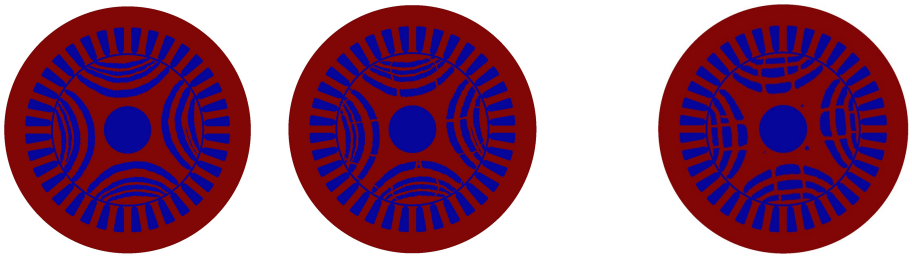

(a) Approche en deux étapes : optimisation magnétique (à gauche) et optimisation mécanique (à droite).

(b) Approche simultanée avec le résultat magnéto-mécanique.

Figure 4.22: Géométries obtenues à partir de la même initialisation pour les deux approches différentes.

Les figures (Fig.4.22a et 4.22b) illustrent les résultats obtenus pour ces deux approches d'optimisation : l'approche en deux étapes et l'optimisation simultanée. Elles mettent en évidence les différences en termes de distribution de matériau, et permettent une comparaison visuelle des effets de chaque méthode sur la conception finale du rotor.

La dernière section de ce chapitre propose une comparaison entre les résultats obtenus avec les deux differentes approches.

Le **Chapitre 4** explore l'optimisation topologique comme méthode pour réduire les vibrations dans les machines électriques. Ces vibrations, principalement induites par les forces électromagnétiques résultant de l'interaction entre le rotor et le stator, représentent une source majeure de bruit acoustique et de dégradations mécaniques. Si elles ne sont pas maîtrisées, elles peuvent entraîner une diminution de la durée de vie des composants et compromettre la fiabilité globale de la machine.

L'objectif principal de cette étude est donc de minimiser ces vibrations tout en maintenant les performances électromagnétiques optimales. Nous nous concentrerons uniquement sur les vibrations du stator. L'optimisation vise à minimiser la réponse vibratoire à des fréquences spécifiques, améliorant ainsi la stabilité mécanique et réduisant le bruit sans affecter les performances électromagnétiques.

L'étude commence par une analyse approfondie des vibrations dans les machines électriques, en distinguant trois sources principales de bruit : mécanique, aéroacoustique et électromagnétique. Cependant, dans les machines modernes, le bruit électromagnétique domine, notamment à des vitesses de rotation modérées. Il est particulièrement gênant, car ses fréquences se situent dans la plage de sensibilité auditive humaine (100 Hz à 15 kHz).

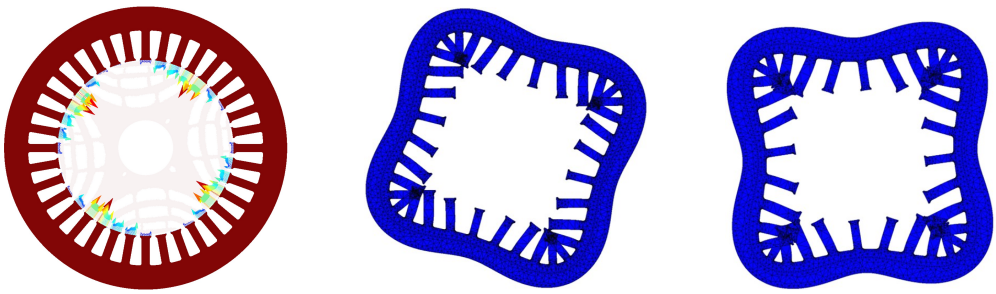

(a) Distribution des forces pour une position statique du rotor.

(b) Déformation du mode 4 avec une fréquence de 7703 Hz.

(c) Déformation due à la 8e harmonique de force.

Figure 4.23: Différentes étapes de l'analyse des vibrations du stator du moteur électrique analysé.

La première étape consiste en une analyse détaillée des forces électromagnétiques à l'origine des vibrations. Ces forces sont calculées à l'aide de la méthode des travaux virtuels, qui permet d'obtenir une estimation précise de leur distribution sur les dents du stator (Fig. 4.23a). Ces forces sont ensuite intégrées dans un modèle méca-dynamique.
Ce modèle permet, dans un premier temps, d'effectuer une analyse modale afin d'identifier les fréquences naturelles de la structure et de caractériser les modes de vibration associés, un exemple est montré dans la Fig. 4.23b . Conséquemment, la méthode de superposition modale est utilisée pour évaluer la réponse dynamique du stator face aux sollicitations électromagnétiques. Plus précisément, elle permet de cibler les harmoniques des forces qui génèrent des résonances (Fig. 4.23c). Ce processus d'analyse offre une compréhension approfondie des fréquences critiques où les vibrations sont les plus intenses, et où des modifications structurelles pourraient être nécessaires pour améliorer la stabilité mécanique.

Dans une deuxième partie, l'optimisation topologique est utilisée pour atténuer les vibrations, une approche largement étudiée en mécanique mais encore peu explorée dans le domaine des machines électriques. Cette méthode vise à réduire la compliance dynamique, une mesure de la réponse vibratoire, en ajustant la répartition des matériaux dans des zones critiques, tout en respectant des contraintes de volume.

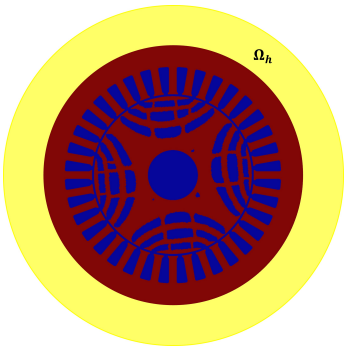

(a) Configuration initiale du moteur électrique et du domaine d'optimisation du carter Ω_h en jaune.

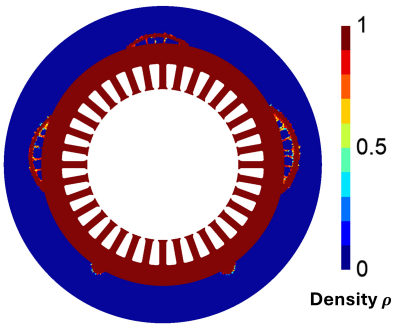

(b) Résultat de l'optimisation.

Figure 4.24: Application de l'optimisation topologique à la conception du carter pour réduire les vibrations.

L'accent est mis sur la conception du carter, un élément clé qui influence les caractéristiques vibratoires sans compromettre les performances électromagnétiques du rotor et du stator. Le rotor utilisé pour le calcul de la force ainsi que le domaine de conception du carter sont montrés dans la Fig. 4.24a. L'approche s'appuie sur la méthode SIMP et utilise l'algorithme MMA

pour résoudre le problème d'optimisation. En ciblant les fréquences critiques pour éviter les résonances, cette stratégie permet de minimiser efficacement les vibrations en sortant de la zone de résonance.

Les résultats obtenus sont significatifs (Fig. 4.24b), montrant une réduction drastique des vibrations. Par exemple, l'amplitude des accélérations maximales a été diminuée de 139 m/s^2 à 6 m/s^2. Les fréquences naturelles de la structure ont été déplacées pour éviter les harmoniques des forces électromagnétiques, améliorant ainsi la stabilité mécanique globale. Ces avancées démontrent la pertinence de l'optimisation topologique pour résoudre les problèmes de vibrations dans les machines électriques, tout en garantissant leur fiabilité et leur performance.

Ce chapitre met en lumière le potentiel de l'optimisation vibratoire pour les machines électriques. Bien qu'encore à un stade préliminaire, les résultats obtenus sont prometteurs et ouvrent la voie à des développements plus complexes et approfondis.

En conclusion, cette thèse explore les capacités des techniques d'optimisation topologique appliquées à la conception et à l'optimisation des machines électriques, avec une attention particulière portée aux problèmes multi-physiques. En s'appuyant sur la méthode SIMP, ce travail a permis de développer une méthodologie complète englobant l'analyse magnéto-mécanique et vibratoire. Des contributions notables incluent une nouvelle formulation pour maximiser le couple moyen dans les machines, ainsi que l'extension de l'optimisation topologique à la réduction des vibrations, notamment par le biais d'un carter optimisé.

Les résultats présentés sont prometteurs, et de nombreuses perspectives restent à explorer. Parmi celles-ci figurent l'intégration d'objectifs supplémentaires, tels que la minimisation des ondulations de couple, la formulation d'un problème d'optimisation multi-objectif, ainsi que l'approfondissement de l'analyse vibratoire. Par ailleurs, le prototypage et l'analyse expérimentale en conditions réelles constituent des étapes essentielles pour valider ces approches et affiner leur applicabilité dans des situations concrètes.

Bibliography

M. Abdalmagid, M. H. Bakr, and A. Emadi. A linesearch-based algorithm for topology and generative optimization of switched reluctance machines. *IEEE Transactions on Transportation Electrification*, 9(3):3849–3866, 2023. doi: 10.1109/TTE.2023.3245992.

G. Allaire, F. Jouve, and A.-M. Toader. A level-set method for shape optimization. *Comptes Rendus Mathematique*, 334(12):1125–1130, 2002. ISSN 1631-073X. doi: https://doi.org/10.1016/S1631-073X(02)02412-3. URL https://www.sciencedirect.com/science/article/pii/S1631073X02024123.

A. Arkkio. *Analysis of induction motors based on the numerical solution of the magnetic field and circuit equations*. PhD thesis, Väitöskirja, Hki, 1987.

C. Babetto, G. Bacco, and N. Bianchi. Design methodology for high-speed synchronous reluctance machines. *IET Electric Power Applications*, 12(8):1110–1116, 2018a. doi: https://doi.org/10.1049/iet-epa.2017.0872. URL https://ietresearch.onlinelibrary.wiley.com/doi/abs/10.1049/iet-epa.2017.0872.

C. Babetto, G. Bacco, and N. Bianchi. Synchronous reluctance machine optimization for high-speed applications. *IEEE Transactions on Energy Conversion*, 33(3):1266–1273, 2018b. doi: 10.1109/TEC.2018.2800536.

J. Bai, P. Sun, R. Wang, and W. Zuo. Dynamic topology optimization of continuum structures considering moving mass excitations. *Engineering Structures*, 291:116433, 2023. ISSN 0141-0296. doi: https://doi.org/10.1016/j.engstruct.2023.116433. URL https://www.sciencedirect.com/science/article/pii/S0141029623008489.

B. Ban, S. Stipetic, and M. Klanac. Synchronous reluctance machines: Theory, design and the potential u se in traction applications. volume 2019-September, pages 177–188. KoREMA, 9 2019. ISBN 9781728103891. doi: 10.1109/EDPE.2019.8883905.

B. Ban, S. Stipetic, and T. Jercic. Minimum set of rotor parameters for synchronous reluctance machine and improved optimization convergence via forced rotor barrier feasibility. *Energies*, 14 (10), 2021. ISSN 1996-1073. doi: 10.3390/en14102744. URL https://www.mdpi.com/1996-1073/14/10/2744.

R. Bargallo. Finite elements for electrical engineering. *Electrical Engineering Department. Universitas Politécnica De Catalunya. Barcelona*, 2006.

J. P. A. Bastos and N. Sadowski. *Electromagnetic modeling by finite element methods*. CRC press, 2003.

K. Bathe. *Finite Element Procedures*. Prentice Hall International editions. Prentice Hall, 1996. ISBN 9780133496970. URL https://books.google.fr/books?id=MrBEPgAACAAJ.

M. Bendsøe. Bendsoe, m.p.: Optimal shape design as a material distribution problem. structural optimization 1, 193-202. *Structural Optimization*, 1:193–202, 01 1989. doi: 10.1007/BF01650949.

M. Bendsøe and O. Sigmund. Material interpolation schemes in topology optimization. *Archive of Applied Mechanics*, 69:635–654, 11 1999. doi: 10.1007/s004190050248.

M. P. Bendsøe. *Optimization of Structural Topology, Shape, and Material*. Springer Berlin Heidelberg, 1995. ISBN 9783662031155. doi: 10.1007/978-3-662-03115-5. URL http://dx.doi.org/10.1007/978-3-662-03115-5.

M. P. Bendsøe and N. Kikuchi. Generating optimal topologies in structural design using a homogenization method. *Computer Methods in Applied Mechanics and Engineering*, 71(2):197–224, 1988. ISSN 0045-7825. doi: https://doi.org/10.1016/0045-7825(88)90086-2. URL https://www.sciencedirect.com/science/article/pii/0045782588900862.

M. P. Bendsøe and O. Sigmund. *Topology Optimization*. Springer Berlin Heidelberg, 2004. ISBN 9783662050866. doi: 10.1007/978-3-662-05086-6. URL http://dx.doi.org/10.1007/978-3-662-05086-6.

C. Bergeron. *Conception de dispositifs électromagnétiques par optimisation de répartition de matière*. PhD thesis, 2023. URL http://www.theses.fr/2023COMP2782. Thèse de doctorat dirigée par Vivier, Stéphane Génie Électrique : Unité de recherche en Mécanique - Laboratoire Roberval (FRE UTC - CNRS 2012) Compiègne 2023.

M. Besbes. *Contribution à la modélisation numérique des phénomènes couplés magneto-élastiques : Application à l'étude des vibrations d'origine magnétique dans les MRV*. PhD thesis, Université

Pierre et Marie Curie (Paris / 1971-2017), École normale supérieure (Cachan, Val-de-Marne), LESIR, 1995.

N. Bianchi, C. Babetto, and G. Bacco. *Synchronous Reluctance Machines: Analysis, optimization and applications*. 12 2021. ISBN 9781839532634. doi: 10.1049/PBPO186E.

A. Bossavit. Virtual power principle and maxwell's tensor: Which comes first? *Compel-the International Journal for Computation and Mathematics in Electrical and Electronic Engineering - COMPEL-INT J COMPUT MATH ELEC*, 30:1804–1814, 11 2011. doi: 10.1108/03321641111168110.

G. Bramerdorfer, J. A. Tapia, J. J. Pyrhönen, and A. Cavagnino. Modern electrical machine design optimization: Techniques, trends, and best practices. *IEEE Transactions on Industrial Electronics*, 65(10):7672–7684, 2018. doi: 10.1109/TIE.2018.2801805.

O. Brun. *Méthodes et outils numériques pour l'optimisation de la forme et de la topologie des machines électriques*. PhD thesis, Université Grenoble Alpes, 2024. Thèse de doctorat dirigée par Chadebec, Olivier et Gerbaud, Laurent Génie électrique Université Grenoble Alpes 2024.

O. Brun, O. Chadebec, P. Ferrouillat, I. Niyonzima, J. Siau, L. Gerbaud, F. Vi, and Y. Le Floch. Magneto-Mechanical Free Shape Optimization of Synchronous Reluctance Machines. In *17th International Workshop on Optimization and Inverse Problems in Electromagnetism (OIPE'2023)*, Graz, Austria, Sept. 2023. URL `https://hal.science/hal-04214785`.

O. Brun, O. Chadebec, P. Ferrouillat, I. Niyonzima, Z. Luo, Y. Le Floch, J. Siau, F. Vi, and L. Gerbaud. A level-set-based topology optimization for maximizing the torque of synchronous reluctance machines. *IEEE Transactions on Magnetics*, 60(3):1–4, 2024. doi: 10.1109/TMAG.2023.3326878.

T. Bruns and D. Tortorelli. Topology optimization of non-linear structures and compliant mechanisms. *Computer Methods in Applied Mechanics and Engineering*, 190:3443–3459, 03 2001. doi: 10.1016/S0045-7825(00)00278-4.

J.-K. Byun and S.-y. Hahn. Topology optimization of switched reluctance motor using mutual energy method. *International Journal of Applied Electromagnetics and Mechanics*, 13:421–426, 01 2001. doi: 10.3233/JAE-2002-349.

F. Campelo, J. Ramirez, and H. Igarashi. A survey of topology optimization in electromagnetics: considerations and current trends. *Academia*, 46:2010, 2010.

A. Carlsson, V. Josefsson, J. Fagerberg, K. Ahlgren, C. Sandström, and G. Puccio. Parametric optimization of flux barriers for torque ripple and tooth force minimization in permanent

magnet synchronous machines. In *2024 International Conference on Electrical Machines (ICEM)*, pages 1–7, 2024. doi: 10.1109/ICEM60801.2024.10700202.

J. Cea. Conception optimale ou identification de formes, calcul rapide de la dérivée directionnelle de la fonction coût. *Mathematical Modelling and Numerical Analysis*, 20:371–402, 1986. URL https://api.semanticscholar.org/CorpusID:124913901.

H. Chen and C. H. T. Lee. Parametric sensitivity analysis and design optimization of an interior permanent magnet synchronous motor. *IEEE Access*, 7:159918–159929, 2019. doi: 10.1109/ACCESS.2019.2950773.

L. Chen, J. Wan, X. Chu, and H. Liu. Parameterized level set method for structural topology optimization based on the cosserat elasticity. *Acta Mechanica Sinica*, 37(4):620–630, Jan. 2021. ISSN 1614-3116. doi: 10.1007/s10409-020-01045-z. URL http://dx.doi.org/10.1007/s10409-020-01045-z.

X. Chen. Topology optimization of microfluidics — a review. *Microchemical Journal*, 127:52–61, 2016. ISSN 0026-265X. doi: https://doi.org/10.1016/j.microc.2016.02.005. URL https://www.sciencedirect.com/science/article/pii/S0026265X16000266.

T. Cherrière. *Élaboration de méthodes et d'outils logiciels pour l'optimisation topologique magnéto-mécanique de machines électriques tournantes*. Theses, Université Paris-Saclay, Nov. 2023. URL https://theses.hal.science/tel-04636530.

T. Cherriere, S. Hlioui, L. Laurent, F. Louf, H. B. Ahmed, and M. Gabsi. Effects of filtering and current-angle adjustment on the multi-material topology optimization of a three-phase stator. *IEEE Transactions on Magnetics*, 60:1–4, 3 2024. ISSN 19410069. doi: 10.1109/TMAG.2023.3317700.

T. Cherrière, L. Laurent, S. Hlioui, F. Louf, P. Duysinx, C. Geuzaine, H. Ben Ahmed, M. Gabsi, and E. Fernández. Multi-material topology optimization using wachspress interpolations for designing a 3-phase electrical machine stator. *Structural and Multidisciplinary Optimization*, 65 (12), Nov. 2022. ISSN 1615-1488. doi: 10.1007/s00158-022-03460-1. URL http://dx.doi.org/10.1007/s00158-022-03460-1.

T. Cherrière, S. Hlioui, L. Laurent, F. Louf, H. Ben Ahmed, and M. Gabsi. Multi-material topology optimization of a flux switching machine. *Science and Technology for Energy Transition*, 78:41, 2023a. ISSN 2804-7699. doi: 10.2516/stet/2023037. URL http://dx.doi.org/10.2516/stet/2023037.

T. Cherrière, T. Vancorsellis, S. Hlioui, L. Laurent, F. Louf, H. B. Ahmed, and M. Gabsi. A multimaterial topology optimization considering the pm nonlinearity. *IEEE Transactions on Magnetics*, 59(5):1–9, 2023b. doi: 10.1109/TMAG.2023.3256003.

T. Cherrière, S. Hlioui, M. Gabsi, L. Laurent, F. Louf, and H. B. Ahmed. Topology optimization of a complete reluctance machine with no initial information on its geometry. In *2024 International Conference on Electrical Machines (ICEM)*, pages 1–7, 2024. doi: 10.1109/ICEM60801.2024.10700155.

H. N. Choi, J. Seong Lee, and I. H. Park. Shape optimization of synrm to obtain minimum torque ripple using continuum sensitivity analysis. In *2020 23rd International Conference on Electrical Machines and Systems (ICEMS)*, pages 1134–1137, 2020. doi: 10.23919/ICEMS50442.2020.9290996.

J. S. Choi and J. Yoo. Structural optimization of ferromagnetic materials based on the magnetic reluctivity for magnetic field problems. *Computer Methods in Applied Mechanics and Engineering*, 197(49):4193–4206, 2008. ISSN 0045-7825. doi: https://doi.org/10.1016/j.cma.2008.04.019. URL https://www.sciencedirect.com/science/article/pii/S0045782508001771.

J. S. Choi, K. Izui, S. Nishiwaki, A. Kawamoto, and T. Nomura. Topology optimization of the stator for minimizing cogging torque of ipm motors. *IEEE Transactions on Magnetics*, 47(10):3024–3027, 2011. doi: 10.1109/TMAG.2011.2158572.

M. Chowdhury, A. Tesfamicael, M. Islam, and I. Husain. Design optimization of a synchronous reluctance machine for high-performance applications. *IEEE Transactions on Industry Applications*, 57(5):4720–4732, 2021. doi: 10.1109/TIA.2021.3091416.

J.-L. Coulomb and G. Meunier. Finite element implementation of virtual work principle for magnetic or electric force and torque computation. *IEEE Transactions on Magnetics*, 20:1894–1896, 1984. URL https://api.semanticscholar.org/CorpusID:123647464.

A. Credo, G. Fabri, M. Villani, and M. Popescu. High speed synchronous reluctance motors for electric vehicles: a focus on rotor mechanical design. In *2019 IEEE International Electric Machines amp; Drives Conference (IEMDC)*, page 165–171. IEEE, May 2019. doi: 10.1109/iemdc.2019.8785083. URL http://dx.doi.org/10.1109/IEMDC.2019.8785083.

A. Credo, G. Fabri, M. Villani, and M. Popescu. Adopting the topology optimization in the design of high-speed synchronous reluctance motors for electric vehicles. *IEEE Transactions on Industry Applications*, 56(5):5429–5438, 2020. doi: 10.1109/TIA.2020.3007366.

M. A. Darmani, A. Cavagnino, S. Vaschetto, F. Marignetti, and C. Gerada. Multiphysics sizing of interior permanent magnet machines based on geometric methodology. *IEEE Open Journal of Industry Applications*, 5:283–299, 2024. doi: 10.1109/OJIA.2024.3427863.

B. Davat, Z. Ren, and M. Lajoie-Mazenc. The movement in field modeling. *IEEE Transactions on Magnetics*, 21(6):2296–2298, 1985. doi: 10.1109/TMAG.1985.1064185.

L. N. de Castro and J. Timmis. *Artificial Immune Systems: A New Computational Intelligence Approach*. Springer-Verlag, 2002. ISBN 978-1-85233-594-6.

J. D. Deaton and R. V. Grandhi. A survey of structural and multidisciplinary continuum topology optimization: post 2000. *Structural and Multidisciplinary Optimization*, 49(1):1–38, July 2013. ISSN 1615-1488. doi: 10.1007/s00158-013-0956-z. URL http://dx.doi.org/10.1007/s00158-013-0956-z.

C. B. Dilgen, S. B. Dilgen, N. Aage, and J. S. Jensen. Topology optimization of acoustic mechanical interaction problems: a comparative review. *Structural and Multidisciplinary Optimization*, 60(2): 779–801, Mar. 2019. ISSN 1615-1488. doi: 10.1007/s00158-019-02236-4. URL http://dx.doi.org/10.1007/s00158-019-02236-4.

J. Du and N. Olhoff. Topological design of freely vibrating continuum structures for maximum values of simple and multiple eigenfrequencies and frequency gaps. *Structural and Multidisciplinary Optimization*, 34(2):91–110, May 2007. ISSN 1615-1488. doi: 10.1007/s00158-007-0101-y. URL http://dx.doi.org/10.1007/s00158-007-0101-y.

D. Dyck and D. Lowther. Automated design of magnetic devices by optimizing material distribution. *IEEE Transactions on Magnetics*, 32(3):1188–1193, 1996. doi: 10.1109/20.497456.

A. R. Díaaz and N. Kikuchi. Solutions to shape and topology eigenvalue optimization problems using a homogenization method. *International Journal for Numerical Methods in Engineering*, 35 (7):1487–1502, Oct. 1992. ISSN 1097-0207. doi: 10.1002/nme.1620350707. URL http://dx.doi.org/10.1002/nme.1620350707.

A. Fawaz, Y. Hua, S. Le Corre, Y. Fan, and L. Luo. Topology optimization of heat exchangers: A review. *Energy*, 252:124053, 2022. ISSN 0360-5442. doi: https://doi.org/10.1016/j.energy.2022.124053. URL https://www.sciencedirect.com/science/article/pii/S0360544222009562.

J. FONTCHASTAGNER and F. MESSINE. Conception par optimisation des actionneurs électromécaniques - aspects méthodologiques. *Conversion de l'énergie électrique*, Feb. 2023. doi: 10.51257/a-v1-d3415. URL http://dx.doi.org/10.51257/a-v1-d3415.

M. Gamba, G. Pellegrino, and F. Cupertino. Optimal number of rotor parameters for the automatic design of synchronous reluctance machines. In *2014 International Conference on Electrical Machines (ICEM)*, pages 1334–1340, 2014. doi: 10.1109/ICELMACH.2014.6960355.

P. Gangl, U. Langer, A. Laurain, H. Meftahi, and K. Sturm. Shape optimization of an electric motor subject to nonlinear magnetostatics. *SIAM Journal on Scientific Computing*, 37(6):B1002–B1025, Jan. 2015. ISSN 1095-7197. doi: 10.1137/15100477x. URL http://dx.doi.org/10.1137/15100477X.

P. Gangl, S. Amstutz, and U. Langer. Topology optimization of electric motor using topological derivative for nonlinear magnetostatics. *IEEE Transactions on Magnetics*, 52(3):1–4, 2016. doi: 10.1109/TMAG.2015.2496172.

J. Gao, M. Xiao, Y. Zhang, and L. Gao. A comprehensive review of isogeometric topology optimization: Methods, applications and prospects. *Chinese Journal of Mechanical Engineering*, 33(1), Nov. 2020. ISSN 2192-8258. doi: 10.1186/s10033-020-00503-w. URL http://dx.doi.org/10.1186/s10033-020-00503-w.

M. Garibaldi, C. Gerada, I. Ashcroft, and R. Hague. Free-form design of electrical machine rotor cores for production using additive manufacturing. *Journal of Mechanical Design*, 141:1, 02 2019. doi: 10.1115/1.4042621.

T. Gauthey, P. Gangl, and M. H. Hassan. Multi-material topology optimization with continuous magnetization direction for motors design. In *2022 International Conference on Electrical Machines (ICEM)*, pages 483–489, 2022. doi: 10.1109/ICEM51905.2022.9910654.

T. Gauthey, M. H. Hassan, F. Messine, and F. Gillon. Topology optimization of the harmonic content for torque ripple minimization. *IEEE Transactions on Magnetics*, 60(3):1–4, 2024. doi: 10.1109/TMAG.2023.3303679.

F. Guo, M. Salameh, M. Krishnamurthy, and I. P. Brown. Multimaterial magneto-structural topology optimization of wound field synchronous machine rotors. *IEEE Transactions on Industry Applications*, 56(4):3656–3667, 2020. doi: 10.1109/TIA.2020.2989682.

F. Guo, N. Tang, and I. P. Brown. Combined dimensional and topology optimization of synchronous machine rotors using a material density interpolation method. *IEEE Transactions on Industry Applications*, 59(6):6591–6600, 2023a. doi: 10.1109/TIA.2023.3292214.

X. Guo, H. Yang, and R. Tu. Multi-objective sequential topology optimization method of interior pm machine based on ngnet. In *2023 IEEE 6th International Electrical and Energy Conference (CIEEC)*, pages 4566–4571, 2023b. doi: 10.1109/CIEEC58067.2023.10167421.

M. Hage-Hassan, M. Zaied, A. Silvestrini, A. Ospina, N.-E. Fenineche, and G. Krebs. Multi-Material BESO Topology Optimization for SynRM based on printed FeSi6.5%. In *COMPUMAG 2023, the 24th International Conference on the Computation of Electromagnetic Fields*, Kyoto (Japan), Japan, May 2023. URL `https://centralesupelec.hal.science/hal-04246986`.

S. Hayashi, Y. Kubota, S. Soma, M. Ohtani, and H. Igarashi. Topology optimization of permanent magnet synchronous motor considering the control system. *IEEE Transactions on Magnetics*, 58 (9):1–5, 2022. doi: 10.1109/TMAG.2022.3172718.

S. Hayashi, Y. Kubota, S. Soma, S. Oya, and H. Igarashi. Topology-parameter hybrid optimization of skewed permanent magnet motor. *IEEE Transactions on Magnetics*, 59(5):1–4, 2023. doi: 10.1109/TMAG.2023.3239620.

Y. Hidaka. Multimaterial topology optimization method based on global search by combinatorial optimization and local search by variable design region method. *IEEE Access*, 10:62450–62458, 2022. doi: 10.1109/ACCESS.2022.3182502.

Y. Hidaka. Multi-objective topology optimization method for hybrid-type motors combining combinatorial optimization and local search. *IEEE Transactions on Magnetics*, 60(3):1–4, 2024. doi: 10.1109/TMAG.2023.3301454.

Y. Hu, Y. Xiao, B. Chen, and Q. Li. Topology optimization of a consequent-pole rotor with v-shaped magnet placement. In *2018 21st International Conference on Electrical Machines and Systems (ICEMS)*, pages 234–239, 2018. doi: 10.23919/ICEMS.2018.8549344.

T. J. Hughes. *The finite element method: linear static and dynamic finite element analysis*. Courier Corporation, 2003.

T. Huguet, J. Šafka, C. Nadal, F. Véle, M. Ackermann, and C. Henaux. Perfomances evaluation of a 3d printed rotor for a synchronous reluctance machine. In *2021 IEEE International Workshop of Electronics, Control, Measurement, Signals and their application to Mechatronics (ECMSM)*, pages 1–8, 2021. doi: 10.1109/ECMSM51310.2021.9468847.

S. Hussain, A. Kallaste, and T. Vaimann. Recent trends in additive manufacturing and topology optimization of reluctance machines. *Energies*, 16(9), 2023. ISSN 1996-1073. doi: 10.3390/en16093840. URL `https://www.mdpi.com/1996-1073/16/9/3840`.

H. Igarashi. Topology optimization of electric motors. In *Compendium on Electromagnetic Analysis*, pages 121–138, 2020. doi: 10.1142/9789813270282_0002. URL https://www.worldscientific.com/doi/abs/10.1142/9789813270282_0002.

C.-H. Im, H.-K. Jung, and Y.-J. Kim. Hybrid genetic algorithm for electromagnetic topology optimization. *Magnetics, IEEE Transactions on*, 39:2163 – 2169, 10 2003. doi: 10.1109/TMAG.2003.817094.

G. U. Jang, S. Cho, J. Moon, K. Jeon, and C.-w. Kim. Topology optimization to reduce electromagnetic force induced vibration for the specific frequency of pmsm motor using electromagnetic-structural coupled analysis. *Energies*, 14(2), 2021. ISSN 1996-1073. doi: 10.3390/en14020431. URL https://www.mdpi.com/1996-1073/14/2/431.

C. JOG. Topology design of structures subjected to periodic loading. *Journal of Sound and Vibration*, 253(3):687–709, 2002. ISSN 0022-460X. doi: https://doi.org/10.1006/jsvi.2001.4075. URL https://www.sciencedirect.com/science/article/pii/S0022460X01940751.

M. Khaleel, H. El-Khozondar, M. Elmnifi, Z. Rajab, E. Yaghoubi, and E. Yaghoubi. Electric vehicles in china, europe, and the united states: Current trend and market comparison. 2:1–20, 01 2024.

N. H. Kim, T. Dong, D. Weinberg, and J. Dalidd. Generalized optimality criteria method for topology optimization. *Applied Sciences*, 11(7), 2021. ISSN 2076-3417. doi: 10.3390/app11073175. URL https://www.mdpi.com/2076-3417/11/7/3175.

Y. S. Kim and I. H. Park. Topology optimization of rotor in synchronous reluctance motor using level set method and shape design sensitivity. *IEEE Transactions on Applied Superconductivity*, 20 (3):1093–1096, 2010. doi: 10.1109/TASC.2010.2040725.

O. Korman, M. Di Nardo, M. Degano, and C. Gerada. On the use of topology optimization for synchronous reluctance machines design. *Energies*, 15(10), 2022a. ISSN 1996-1073. doi: 10.3390/en15103719. URL https://www.mdpi.com/1996-1073/15/10/3719.

O. Korman, M. D. Nardo, M. Degano, and C. Gerada. On the use of topology optimization for synchronous reluctance machines design. *Energies*, 15, 5 2022b. ISSN 19961073. doi: 10.3390/en15103719.

J. K. Kostko. Polyphase reaction synchronous motors. *Journal of the American Institute of Electrical Engineers*, 42(11):1162–1168, 1923. doi: 10.1109/JoAIEE.1923.6591529.

E. Król, M. Maciążek, and T. Wolnik. Review of vibroacoustic analysis methods of electric vehicles motors. *Energies*, 16:2041, 02 2023. doi: 10.3390/en16042041.

E. Kuci, M. Jansen, and O. Coulaud. Level set topology optimization of synchronous reluctance machines using a body-fitted mesh representation. *Structural and Multidisciplinary Optimization*, 64, 08 2021. doi: 10.1007/s00158-021-03049-0.

C. Lee and I. G. Jang. Topology optimization of multiple-barrier synchronous reluctance motors with initial random hollow circles. *Structural and Multidisciplinary Optimization*, 64:2213–2224, 10 2021. ISSN 16151488. doi: 10.1007/s00158-021-02976-2.

C. Lee and I. G. Jang. Multi-material topology optimization for the pmsms under the consideration of the mtpa control. *Structural and Multidisciplinary Optimization*, 65(9), Sept. 2022. ISSN 1615-1488. doi: 10.1007/s00158-022-03367-x. URL http://dx.doi.org/10.1007/s00158-022-03367-x.

C. Lee and I. G. Jang. Topology optimization of the ipmsms considering both the mtpa and fw controls under the voltage and current limitations. *IEEE Transactions on Industrial Electronics*, 70 (8):8244–8253, 2023a. doi: 10.1109/TIE.2023.3234136.

C. Lee and I. G. Jang. Computationally efficient topology optimization for the synrms based on the torque curve interpolation. *Structural and Multidisciplinary Optimization*, 66(7), July 2023b. ISSN 1615-1488. doi: 10.1007/s00158-023-03623-8. URL http://dx.doi.org/10.1007/s00158-023-03623-8.

C. Lee, J. Lee, and I. G. Jang. Topology optimization for the manufacturable and structurally safe synchronous reluctance motors with multiple iron webs and bridges. *IEEE Transactions on Industrial Electronics*, 70(1):678–687, 2023. doi: 10.1109/TIE.2022.3148751.

J. Lee and N. Kikuchi. Structural topology optimization of electrical machinery to maximize stiffness with body force distribution. *IEEE Transactions on Magnetics*, 46(10):3790–3794, 2010. doi: 10.1109/TMAG.2010.2052365.

T.-H. Lee, J.-H. Lee, K.-P. Yi, and D.-K. Lim. Optimal design of a synchronous reluctance motor using a genetic topology algorithm. *Processes*, 9(10), 2021. ISSN 2227-9717. doi: 10.3390/pr9101778. URL https://www.mdpi.com/2227-9717/9/10/1778.

P. Lengvarský and J. Bocko. Theoretical basis of modal analysis. *American Journal of Mechanical Engineering*, 1:173–179, 11 2013. doi: 10.12691/ajme-1-7-4.

Y. Li, B. Ma, J. Zheng, J. Zhu, and G. Lei. Electromagnetic and mechanical topology optimization for synrm rotors considering high dimensional constraints. *IEEE Transactions on Industrial Electronics*, 70(12):12048–12059, 2023a. doi: 10.1109/TIE.2023.3234146.

Y. Li, B. Ma, J. Zheng, J. Zhu, and G. Lei. Electromagnetic and mechanical topology optimization for synrm rotors considering high dimensional constraints. *IEEE Transactions on Industrial Electronics*, 70:12048–12059, 12 2023b. ISSN 15579948. doi: 10.1109/TIE.2023.3234146.

C. Liu, Y. Xu, J. Zou, G. Yu, and L. Zhuo. Permanent magnet shape optimization method for pmsm air gap flux density harmonics reduction. *CES Transactions on Electrical Machines and Systems*, 5 (4):284–290, 2021. doi: 10.30941/CESTEMS.2021.00033.

H. Liu, W. Zhang, and T. Gao. A comparative study of dynamic analysis methods for structural topology optimization under harmonic force excitations. *Structural and Multidisciplinary Optimization*, 51(6):1321–1333, Jan. 2015. ISSN 1615-1488. doi: 10.1007/s00158-014-1218-4. URL http://dx.doi.org/10.1007/s00158-014-1218-4.

B. Lizarribar, B. Prieto, M. Martinez-Iturralde, and G. Artetxe. Novel topology optimization method for weight reduction in electrical machines. *IEEE Access*, 10:67521–67531, 2022. doi: 10.1109/ACCESS.2022.3185741.

F. Lucchini, R. Torchio, V. Cirimele, P. Alotto, and P. Bettini. Topology optimization for electromagnetics: A survey. *IEEE Access*, 10:98593–98611, 2022. doi: 10.1109/ACCESS.2022.3206368.

Z. Luo, L. Tong, J. Luo, P. Wei, and M. Y. Wang. Design of piezoelectric actuators using a multiphase level set method of piecewise constants. *Journal of Computational Physics*, 228 (7):2643–2659, 2009. ISSN 0021-9991. doi: https://doi.org/10.1016/j.jcp.2008.12.019. URL https://www.sciencedirect.com/science/article/pii/S0021999108006633.

B. Ma, J. Zheng, G. Lei, J. Zhu, P. Jin, and Y. Guo. Topology optimization of ferromagnetic components in electrical machines. *IEEE Transactions on Energy Conversion*, 35(2):786–798, 2020. doi: 10.1109/TEC.2019.2960519.

Z.-D. Ma, N. Kikuchi, and H.-C. Cheng. Topological design for vibrating structures. *Computer Methods in Applied Mechanics and Engineering*, 121(1):259–280, 1995. ISSN 0045-7825. doi: https://doi.org/10.1016/0045-7825(94)00714-X. URL https://www.sciencedirect.com/science/article/pii/004578259400714X.

M. R. Mahmoud, M. N. Ibrahim, and P. Sergeant. Topology optimization for enhancing electric machine performance: A review. In *2024 International Conference on Electrical Machines (ICEM)*, pages 1–7, 2024. doi: 10.1109/ICEM60801.2024.10700505.

A. Marrocco. Analyse numérique de problèmes d'électrotechnique. *Annales des sciences mathématiques du Québec*, 1(2):271–296, 1977.

J. C. Maxwell. *A Treatise on Electricity and Magnetism*. Cambridge University Press, June 1892. ISBN 9780511709340. doi: 10.1017/cbo9780511709340. URL http://dx.doi.org/10.1017/CBO9780511709340.

D. Meeker. *Finite Element Method Magnetics, Version 4.2*. FEMM, 2010. URL https://www.femm.info/wiki/HomePage. Available at: https://www.femm.info/wiki/HomePage.

A. Michell. Lviii. the limits of economy of material in frame-structures. *The London, Edinburgh, and Dublin Philosophical Magazine and Journal of Science*, 8(47):589–597, 1904. doi: 10.1080/14786440409463229. URL https://doi.org/10.1080/14786440409463229.

X. Mininger, N. Galopin, F. Bouillault, and M. Gabsi. Analysis of electromagnetic strains on a structure such as switched reluctance machine. *The European Physical Journal Applied Physics*, 39(2):191–196, June 2007. ISSN 1286-0050. doi: 10.1051/epjap:2007109. URL http://dx.doi.org/10.1051/epjap:2007109.

R. Moghaddam. *Synchronous Reluctance Machine (SynRM) Design*. PhD thesis, 01 2007.

B. S. B. Mohamodhosen. *Topology optimisation of electromagnetic devices*. Theses, Ecole Centrale de Lille, Dec. 2017. URL https://theses.hal.science/tel-01818091.

M. Murataliyev, M. Degano, M. Di Nardo, N. Bianchi, and C. Gerada. Synchronous reluctance machines: A comprehensive review and technology comparison. *Proceedings of the IEEE*, 110 (3):382–399, 2022. doi: 10.1109/JPROC.2022.3145662.

M. D. Nardo, G. L. Calzo, M. Galea, and C. Gerada. Design optimization of a high-speed synchronous reluctance machine. *IEEE Transactions on Industry Applications*, 54(1):233–243, 2018. doi: 10.1109/TIA.2017.2758759.

F. Nishanth and B. Wang. Topology optimization of electric machines: A review. In *2022 IEEE Energy Conversion Congress and Exposition (ECCE)*, pages 1–8, 2022. doi: 10.1109/ECCE50734.2022.9948073.

B. Niu, X. He, Y. Shan, and R. Yang. On objective functions of minimizing the vibration response of continuum structures subjected to external harmonic excitation. *Structural and Multidisciplinary Optimization*, 57(6):2291–2307, Dec. 2017. ISSN 1615-1488. doi: 10.1007/s00158-017-1859-1. URL http://dx.doi.org/10.1007/s00158-017-1859-1.

Y. Okamoto, R. Hoshino, S. Wakao, and T. Tsuburaya. Improvement of torque characteristics for a synchronous reluctance motor using mma-based topology optimization method. *IEEE Transactions on Magnetics*, 54, 3 2018. ISSN 00189464. doi: 10.1109/TMAG.2017.2762000.

S. Osher and J. A. Sethian. Fronts propagating with curvature-dependent speed: Algorithms based on hamilton-jacobi formulations. *Journal of Computational Physics*, 79(1):12–49, 1988. ISSN 0021-9991. doi: https://doi.org/10.1016/0021-9991(88)90002-2. URL https://www.sciencedirect.com/science/article/pii/0021999188900022.

Y. Otomo and H. Igarashi. Topology optimization using gabor filter: Application to synchronous reluctance motor. *IEEE Transactions on Magnetics*, 57(6):1–4, 2021. doi: 10.1109/TMAG.2021.3057402.

S. Panda, R. K. Keshri, A. Tessarolo, G. Tiwari, and M. Mezzarobba. Design refinements of synchronous reluctance motor utilising non-magnetic radial ribs for traction applications. *IET Electric Power Applications*, 14(12):2480–2489, Oct. 2020. ISSN 1751-8679. doi: 10.1049/iet-epa.2020.0199. URL http://dx.doi.org/10.1049/iet-epa.2020.0199.

G. Pellegrino, T. M. Jahns, N. Bianchi, W. L. Soong, and F. Cupertino. *The rediscovery of synchronous reluctance and ferrite permanent magnet motors*. SpringerBriefs in Electrical and Computer Engineering. Springer International Publishing, Cham, Switzerland, 1 edition, Apr. 2016.

P. Putek. Mitigation of the cogging torque and loss minimization in a permanent magnet machine using shape and topology optimization. *Engineering Computations*, 33:831–854, 05 2016. doi: 10.1108/EC-01-2015-0007.

Y. Qin, X. Tang, T. Jia, Z. Duan, J. Zhang, Y. Li, and L. Zheng. Noise and vibration suppression in hybrid electric vehicles: State of the art and challenges. *Renewable and Sustainable Energy Reviews*, 124:109782, 2020. ISSN 1364-0321. doi: https://doi.org/10.1016/j.rser.2020.109782. URL https://www.sciencedirect.com/science/article/pii/S1364032120300782.

G. Rozvany. Grillages of maximum strength and maximum stiffness. *International Journal of Mechanical Sciences*, 14(10):651–666, 1972. ISSN 0020-7403. doi: https://doi.org/10.1016/0020-7403(72)90023-9. URL https://www.sciencedirect.com/science/article/pii/0020740372900239.

G. Rozvany and W. Prager. Optimal design of partially discretized grillages. *Journal of the Mechanics and Physics of Solids*, 24(2):125–136, 1976. ISSN 0022-5096. doi: https://doi.org/

10.1016/0022-5096(76)90022-3. URL https://www.sciencedirect.com/science/article/pii/0022509676900223.

N. Sadowski, Y. Lefevre, M. Lajoie-Mazenc, and J. Cros. Finite element torque calculation in electrical machines while considering the movement. *IEEE Transactions on Magnetics*, 28(2):1410–1413, 1992. doi: 10.1109/20.123957.

J.-H. Saiac. Mathématiques et méthodes numériques, tome 2. Course material, E.S.C.P.I. G.M.3, June 2009.

H. Sasaki and H. Igarashi. Topology optimization using basis functions for improvement of rotating machine performances. *IEEE Transactions on Magnetics*, 54(3):1–4, 2018. doi: 10.1109/TMAG.2017.2759784.

S. Sato, T. Sato, and H. Igarashi. Topology optimization of synchronous reluctance motor using normalized gaussian network. *IEEE Transactions on Magnetics*, 51(3):1–4, 2015a. doi: 10.1109/TMAG.2014.2359679.

T. Sato, K. Watanabe, and H. Igarashi. Multimaterial topology optimization of electric machines based on normalized gaussian network. *IEEE Transactions on Magnetics*, 51(3):1–4, 2015b. doi: 10.1109/TMAG.2014.2359972.

H. Sawada, R. Suzuki, Y. Okamoto, and S. Wakao. Optimization of rotor structure for synchronous reluctance motor using coupled topology optimization based on electromagnetic field analysis and structural mechanics. In *2019 19th International Symposium on Electromagnetic Fields in Mechatronics, Electrical and Electronic Engineering (ISEF)*, pages 1–2, 2019. doi: 10.1109/ISEF45929.2019.9097069.

A. Selema, M. N. Ibrahim, and P. Sergeant. Additively manufactured ultralight shaped-profile windings for hf electrical machines and weight-sensitive applications. *IEEE Transactions on Transportation Electrification*, 8(4):4313–4324, 2022a. doi: 10.1109/TTE.2022.3173126.

A. Selema, M. N. Ibrahim, and P. Sergeant. Metal additive manufacturing for electrical machines: Technology review and latest advancements. *Energies*, 15(3):1076, Jan. 2022b. ISSN 1996-1073. doi: 10.3390/en15031076. URL http://dx.doi.org/10.3390/en15031076.

H. Shim and S. Wang. Topology optimization of magneto-mechanical systems considering magnetic force and magnetostriction. In *49th AIAA/ASME/ASCE/AHS/ASC Structures, Structural Dynamics, and Materials Conference amp;lt;bramp;gt; 16th AIAA/ASME/AHS Adaptive Structures*

Conferenceamp;lt;bramp;gt; 10t. American Institute of Aeronautics and Astronautics, Apr. 2008. doi: 10.2514/6.2008-1711. URL http://dx.doi.org/10.2514/6.2008-1711.

H. Shim, H. Moon, S. Wang, and K. Hameyer. Topology optimization for compliance reduction of magnetomechanical systems. *IEEE Transactions on Magnetics*, 44(3):346–351, 2008. doi: 10.1109/TMAG.2007.914670.

O. Sigmund. *Design of material structures using topology optimization*. PhD thesis, Department of Solid Mechanics (now: Department of Mechanical Engineering/Solid Mechanics) Technical University of Denmark, 1994.

O. Sigmund. A 99 line topology optimization code written in matlab. *Structural and Multidisciplinary Optimization*, 21(2):120–127, Apr. 2001. ISSN 1615-1488. doi: 10.1007/s001580050176. URL http://dx.doi.org/10.1007/s001580050176.

O. Sigmund. Morphology-based black and white filters for topology optimization. *Structural and Multidisciplinary Optimization*, 33(4–5):401–424, Jan. 2007. ISSN 1615-1488. doi: 10.1007/s00158-006-0087-x. URL http://dx.doi.org/10.1007/s00158-006-0087-x.

O. Sigmund and K. Maute. Topology optimization approaches: A comparative review. *Structural and Multidisciplinary Optimization*, 48(6):1031–1055, Aug. 2013. ISSN 1615-1488. doi: 10.1007/s00158-013-0978-6. URL http://dx.doi.org/10.1007/s00158-013-0978-6.

O. Sigmund and J. Petersson. Numerical instabilities in topology optimization: A survey on procedures dealing with checkerboards, mesh-dependencies and local minima. *Structural Optimization*, 16:68–75, 08 1998. doi: 10.1007/BF01214002.

Z. Sun, H. Otsuki, T. Sato, and K. Watanabe. Topology optimization of a switched reluctance machine by electromagnetic-structural multiphysics finite element analysis. *IEEE Transactions on Magnetics*, 60(3):1–5, 2024. doi: 10.1109/TMAG.2023.3301903.

K. Svanberg. The method of moving asymptotes—a new method for structural optimization. *International Journal for Numerical Methods in Engineering*, 24(2):359–373, 1987. doi: https://doi.org/10.1002/nme.1620240207. URL https://onlinelibrary.wiley.com/doi/abs/10.1002/nme.1620240207.

K. Svanberg. A class of globally convergent optimization methods based on conservative convex separable approximations. *SIAM Journal on Optimization*, 12(2):555–573, 2002. doi: 10.1137/S1052623499362822. URL https://doi.org/10.1137/S1052623499362822.

K. Svanberg. Mma and gcmma – two methods for nonlinear optimization, 2014. URL https://api.semanticscholar.org/CorpusID:211105912.

K. Svanberg and H. Svärd. Density filters for topology optimization based on the pythagorean means. *Structural and Multidisciplinary Optimization*, 48(5):859–875, June 2013. ISSN 1615-1488. doi: 10.1007/s00158-013-0938-1. URL http://dx.doi.org/10.1007/s00158-013-0938-1.

H. Tiismus, A. Kallaste, T. Vaimann, and A. Rassõlkin. State of the art of additively manufactured electromagnetic materials for topology optimized electrical machines. *Additive Manufacturing*, 55:102778, 03 2022a. doi: 10.1016/j.addma.2022.102778.

H. Tiismus, A. Kallaste, T. Vaimann, and A. Rassõlkin. State of the art of additively manufactured electromagnetic materials for topology optimized electrical machines. *Additive Manufacturing*, 55:102778, 2022b. ISSN 2214-8604. doi: https://doi.org/10.1016/j.addma.2022.102778. URL https://www.sciencedirect.com/science/article/pii/S2214860422001828.

P. Vijayraghavan and R. Krishnan. Noise in electric machines: a review. *IEEE Transactions on Industry Applications*, 35(5):1007–1013, 1999. doi: 10.1109/28.793360.

S. Wang and J. Kang. Topology optimization of nonlinear magnetostatics. *IEEE Transactions on Magnetics*, 38(2):1029–1032, 2002. doi: 10.1109/20.996264.

S. Wang, J. Kang, and J. Noh. Topology optimization of a single-phase induction motor for rotary compressor. *IEEE Transactions on Magnetics*, 40(3):1591–1596, 2004. doi: 10.1109/TMAG.2004.827187.

M. Watahiki and K. Akatsu. Optimization of stator core shape to minimize harmonic current in surface permanent magnet synchronous motor using topology optimization algorithm. In *2021 24th International Conference on Electrical Machines and Systems (ICEMS)*, pages 393–397, 2021. doi: 10.23919/ICEMS52562.2021.9634319.

K. Watanabe, T. Suga, and S. Kitabatake. Topology optimization based on the on/off method for synchronous motor. *IEEE Transactions on Magnetics*, 54(3):1–4, 2018. doi: 10.1109/TMAG.2017.2751653.

Y. Yamashita and Y. Okamoto. Design optimization of synchronous reluctance motor for reducing iron loss and improving torque characteristics using topology optimization based on the level-set method. *IEEE Transactions on Magnetics*, 56(3):1–4, 2020. doi: 10.1109/TMAG.2019.2954468.

X. Yang and Y. Li. Structural topology optimization on dynamic compliance at resonance frequency in thermal environments. *Structural and Multidisciplinary Optimization*, 49(1):81–91, July 2013. ISSN 1615-1488. doi: 10.1007/s00158-013-0961-2. URL http://dx.doi.org/10.1007/s00158-013-0961-2.

X. Yang, Y. Xie, G. Steven, and O. Querin. *Bi-directional evolutionary method for stiffness optimisation*. 1998. doi: 10.2514/6.1998-4900. URL https://arc.aiaa.org/doi/abs/10.2514/6.1998-4900.

Y. Yang, B. Bilgin, M. Kasprzak, S. Nalakath, H. Sadek, M. Preindl, J. Cotton, N. Schofield, and A. Emadi. Thermal management of electric machines. *IET Electrical Systems in Transportation*, 7(2):104–116, 2017. doi: https://doi.org/10.1049/iet-est.2015.0050. URL https://ietresearch.onlinelibrary.wiley.com/doi/abs/10.1049/iet-est.2015.0050.

J. Yoo. Reduction of vibration caused by magnetic force in a switched reluctance motor by topology optimization. *Journal of Applied Mechanics*, 69(3):380–387, May 2002. ISSN 1528-9036. doi: 10.1115/1.1467093. URL http://dx.doi.org/10.1115/1.1467093.

J. Yoo and N. Kikuchi. Topology optimization for reduction of vibration caused by magnetic harmonic excitation. *IEEE Transactions on Magnetics*, 38(6):3643–3649, 2002. doi: 10.1109/TMAG.2002.804806.

S. Zhang, C. Liu, Y. Wang, F. Niu, G. Lei, and J. Zhu. Shape design optimization and comparative analysis of a novel synchronous reluctance machine with grain-oriented silicon steel. *IEEE Transactions on Magnetics*, 60(9):1–5, 2024. doi: 10.1109/TMAG.2024.3408809.

X. Zhang and Z. Kang. Topology optimization of piezoelectric layers in plates with active vibration control. *Journal of Intelligent Material Systems and Structures*, 25:697–712, 03 2013. doi: 10.1177/1045389X13500577.

J. Zhao, Z. Wang, H. Liu, F. Ning, X. Hong, J. Du, and M. Yu. Modal analysis and structure optimization of permanent magnet synchronous motor. *IEEE Access*, 8:151856–151865, 2020. doi: 10.1109/ACCESS.2020.3017679.

H. Zhou, X. Wang, L. Xiong, and X. Zhang. Analysis and research on mechanical stress and multiobjective optimization of synchronous reluctance motor. *CES Transactions on Electrical Machines and Systems*, 8(3):274–283, 2024. doi: 10.30941/CESTEMS.2024.00015.

J. Zou, M. Liu, Y. Xu, G. Yu, and H. Lan. Vibration contribution analysis of radial and tangential electromagnetic force harmonic of permanent magnet synchronous motor. *IEEE Transactions on Applied Superconductivity*, 34(8):1–5, 2024. doi: 10.1109/TASC.2024.3456484.